

The following notice applies to any unclassified (including originally classified and now declassified) technical reports released to "qualified U.S. contractors" under the provisions of DoD Directive 5230.25, Withholding of Unclassified Technical Data From Public Disclosure.

NOTICE TO ACCOMPANY THE DISSEMINATION OF EXPORT-CONTROLLED TECHNICAL DATA

- 1. Export of information contained herein, which includes, in some circumstances, release to foreign nationals within the United States, without first obtaining approval or license from the Department of State for items controlled by the International Traffic in Arms Regulations (ITAR), or the Department of Commerce for items controlled by the Export Administration Regulations (EAR), may constitute a violation of law.**
- 2. Under 22 U.S.C. 2778 the penalty for unlawful export of items or information controlled under the ITAR is up to ten years imprisonment, or a fine of \$1,000,000, or both. Under 50 U.S.C., Appendix 2410, the penalty for unlawful export of items or information controlled under the EAR is a fine of up to \$1,000,000, or five times the value of the exports, whichever is greater; or for an individual, imprisonment of up to 10 years, or a fine of up to \$250,000, or both.**
- 3. In accordance with your certification that establishes you as a "qualified U.S. Contractor", unauthorized dissemination of this information is prohibited and may result in disqualification as a qualified U.S. contractor, and may be considered in determining your eligibility for future contracts with the Department of Defense.**
- 4. The U.S. Government assumes no liability for direct patent infringement, or contributory patent infringement or misuse of technical data.**
- 5. The U.S. Government does not warrant the adequacy, accuracy, currency, or completeness of the technical data.**
- 6. The U.S. Government assumes no liability for loss, damage, or injury resulting from manufacture or use for any purpose of any product, article, system, or material involving reliance upon any or all technical data furnished in response to the request for technical data.**
- 7. If the technical data furnished by the Government will be used for commercial manufacturing or other profit potential, a license for such use may be necessary. Any payments made in support of the request for data do not include or involve any license rights.**
- 8. A copy of this notice shall be provided with any partial or complete reproduction of these data that are provided to qualified U.S. contractors.**

DESTRUCTION NOTICE

For classified documents, follow the procedure in DoD 5220.22-M, National Industrial Security Program, Operating Manual, Chapter 5, Section 7, or DoD 5200.1-R, Information Security Program Regulation, Chapter 6, Section 7. For unclassified, limited documents, destroy by any method that will prevent disclosure of contents or reconstruction of the document.

DIRECTED ENERGY HPM, PP, & PPS EFFORTS: MAGNETIZED TARGET FUSION – FIELD REVERSED CONFIGURATION

Theodore C. Grabowski

**Science Applications International Corporation
2109 Air Park Road SE
Albuquerque, NM 87106**

4 August 2006

Final Report

APPROVED FOR PUBLIC RELEASE; DISTRIBUTION IS UNLIMITED.



**AIR FORCE RESEARCH LABORATORY
Directed Energy Directorate
3550 Aberdeen Ave SE
AIR FORCE MATERIEL COMMAND
KIRTLAND AIR FORCE BASE, NM 87117-5776**

**DTIC COPY
NOTICE AND SIGNATURE PAGE**

Using Government drawings, specifications, or other data included in this document for any purpose other than Government procurement does not in any way obligate the U.S. Government. The fact that the Government formulated or supplied the drawings, specifications, or other data does not license the holder or any other person or corporation; or convey any rights or permission to manufacture, use, or sell any patented invention that may relate to them.

This report was cleared for public release by the Air Force Research Laboratory, Philips Research Site Public Affairs Office and is available to the general public, including foreign nationals. Copies may be obtained from the Defense Technical Information Center (DTIC) (<http://www.dtic.mil>).

AFRL-DE-PS-TR-2006-1086 HAS BEEN REVIEWED AND IS APPROVED FOR PUBLICATION IN ACCORDANCE WITH ASSIGNED DISTRIBUTION STATEMENT.

//Signature//

JAMES A. DEGNAN, DR-IV
Project Manager

//Signature//

JOSEPH F. PUGLIESE, Lt Col, USAF
Chief, DEH Division

This report is published in the interest of scientific and technical information exchange, and its publication does not constitute the Government's approval or disapproval of its ideas or findings.

REPORT DOCUMENTATION PAGE			<i>Form Approved</i> OMB No. 0704-0188		
Public reporting burden for this collection of information is estimated to average 1 hour per response, including the time for reviewing instructions, searching existing data sources, gathering and maintaining the data needed, and completing and reviewing this collection of information. Send comments regarding this burden estimate or any other aspect of this collection of information, including suggestions for reducing this burden to Department of Defense, Washington Headquarters Services, Directorate for Information Operations and Reports (0704-0188), 1215 Jefferson Davis Highway, Suite 1204, Arlington, VA 22202-4302. Respondents should be aware that notwithstanding any other provision of law, no person shall be subject to any penalty for failing to comply with a collection of information if it does not display a currently valid OMB control number. PLEASE DO NOT RETURN YOUR FORM TO THE ABOVE ADDRESS.					
1. REPORT DATE (DD-MM-YYYY) 4 August 2006		2. REPORT TYPE Final Report		3. DATES COVERED (From - To) 03 Jun 03 - 30 Jun 06	
4. TITLE AND SUBTITLE Directed Energy HPM, PP, & PPS Efforts: Magnetized Target Fusion - Field Reversed Configuration			5a. CONTRACT NUMBER F29601-00-D-0055/0036		
			5b. GRANT NUMBER		
			5c. PROGRAM ELEMENT NUMBER 62601F		
6. AUTHOR(S) Theodore C. Grabowski			5d. PROJECT NUMBER D0E4		
			5e. TASK NUMBER HB		
			5f. WORK UNIT NUMBER AB		
7. PERFORMING ORGANIZATION NAME(S) AND ADDRESS(ES) Science Applications International Corporation 2109 Air Park Road SE Albuquerque, NM 87106			8. PERFORMING ORGANIZATION REPORT		
9. SPONSORING / MONITORING AGENCY NAME(S) AND ADDRESS(ES) Air Force Research Laboratory 3550 Aberdeen Ave SE Kirtland AFB, NM 87117-5776			10. SPONSOR/MONITOR'S ACRONYM(S)		
			11. SPONSOR/MONITOR'S REPORT NUMBER(S) AFRL-DE-PS-TR-2006-1086		
12. DISTRIBUTION / AVAILABILITY STATEMENT APPROVED FOR PUBLIC RELEASE; DISTRIBUTION IS UNLIMITED.					
13. SUPPLEMENTARY NOTES					
14. ABSTRACT This effort continued MTF-FRC experimental work at Los Alamos National Laboratory's (LANL's) FRX-L (Field Reversed experiment - Liner) facility and the start up of a parallel experimental effort for forming and translation Field Reversed Configurations (FRCs) at AFRL's Building 322 on Kirtland Air Force Base. This effort also included developing an improved Crowbar switch to reduce modulation of the main discharge used to form the FRCs, as well as considerable design and construction of other FRC formation hardware. In addition, two liner-on-vacuum implosion experiments were also performed on the Shiva Star High Energy Capacitor Bank to verify the scheme that has been proposed to adiabatically compress and heat the FRCs to fusion-relevant densities and temperatures. This scheme used a deformable liner-electrode contact instead of the standard sliding contact in order to allow the placement of an aperture in the electrode that is sufficiently large (8 cm diameter) to enable FRC injection into the liner interior.					
15. SUBJECT TERMS Magnetized Target Fusion (MTF), Field-Reversed Configuration (FRC), Alternative Confinement Concepts, Fusion Energy					
16. SECURITY CLASSIFICATION OF:			17. LIMITATION OF ABSTRACT SAR	18. NUMBER OF PAGES 124	19a. NAME OF RESPONSIBLE PERSON Dr. James Degnan
a. REPORT UNCLASSIFIED	b. ABSTRACT UNCLASSIFIED	c. THIS PAGE UNCLASSIFIED			19b. TELEPHONE NUMBER (include area code)

Table of Contents

List of Figures	v
List of Tables	xii
List of Acronyms	xiii
Executive Summary	xiv
1.0 Design, Fabrication, and Assembly of the FRC Formation and Translation Experiment at AFRL	1
1.1 Overview.....	1
1.2 Main Bank and Crowbar Switch.....	4
1.3 Pre-Ionization Bank	11
1.4 Bias Bank.....	14
1.5 Theta Coil Cable Header.....	15
1.6 Cusp, Guide, and Mirror Banks	19
1.7 Vacuum Vessel and Field Coil Configuration.....	21
1.8 Trigger Generators, Power Supplies, HV Cables, and Other Support Hardware	22
1.9 Control System.....	25
1.10 Diagnostics.....	26
2.0 Deformable Contact Solid Liner Tests	27
2.1 December 2003 Test	27
2.2 January 2005 Test	31
3.0 Support of Experimental Effort (FRX-L) at Los Alamos.....	36
3.1 Lower-Inductance Crowbar Switch for the FRX-L Main Bank	36
3.1.1 First Crowbar Switch – Description of Triggering Problems and Excessive Modulation.....	36
3.1.2 Steps Taken to Alter Circuit Properties External to the Crowbar Switch.....	40
3.1.3 Redesign of the Crowbar Switch to Dramatically Reduce Current Modulation.....	41
3.1.4 Fabrication, Delivery, and Assembly of the New Crowbar Switch.....	43
3.1.5 Evaluation of the Initial Operation of the New FRX-L Crowbar Switch.....	46
3.1.6 Analysis of Triggering Problems With the New Crowbar Switch	49
3.1.7 Slotted Bus Plate Design For Rail Gap Inductive Isolation.....	54
3.2 Implementation of Passive Mirror Concept.....	56
3.3 Design Support for FRC Translation Efforts	58
4.0 Publications and Presentations.....	60
5.0 Summary of Present Work and Future Plans.....	61
Appendix A. Inventory of Hardware Available for the AFRL FRC Formation and Translation Experiment.....	A-1

Appendix B.	Preliminary List of Control and Status Signal Lines Required By the FTX Control System.....	B-1
Appendix C.	Pulsed Power Diagnostics and Triggers Required for FTX.....	C-1
Appendix D.	Slide Summary Describing the Changes Made in the New FRX-L Crowbar Switch Design	D-1
Appendix E.	Analysis for Establishing Better Isolation and/or Better Triggering Between the FRX-L Crowbar Rail Gaps	E-1
Appendix F.	Estimates of Mutual Coupling Between Sections of the Slotted Crowbar Switch Bus Work	F-1
Appendix G.	Two-Stage PFN Concept to Increase Bias Current and Decrease Bias Pulse Duration	G-1
Appendix H.	Initial Analysis of PFN Concept for Driving the FRC Guide/Mirror Field Coils	H-1
Distribution List		I-1

List of Figures

Figure 1.	Proposed layout for the FTX/F-LINCX experimental hardware in the Building 322 high bay.....	Error! Bookmark not defined.
Figure 2.	Global circuit diagram for the FTX capacitor banks and their trigger units and power supplies. Note that the FRX-L field coil configuration and vacuum hardware stand has been shown in this diagram to provide a starting point for the experimental design.	Error! Bookmark not defined.
Figure 3.	Solid Works® rendering of the FTX Main bank (“mini-module”) design. The brown frame shown has the same inner dimensions as the Shiva Unistrut framework, so it seems that there will be sufficient space for the Main bank under the Shiva arms.....	5
Figure 4.	Quick Field calculation of the current density distribution in the hot bus plates of the FTX Main bank. The potential is +35 kV on the upper capacitor terminals and –35 kV on the lower capacitor terminals.	5
Figure 5.	A second Quick Field calculation of the current density distribution in the hot bus plates of the FTX Main bank, however this time one-inch slots have been placed near several capacitor terminals to redistribute the current flow. The potentials on capacitor terminals are the same as in Fig. 4.....	6
Figure 6.	(a) Front and (b) back views of the final FTX Main bank design. The back view also shows the new Crowbar switch in place on the bank.....	7
Figure 7.	(a) The Unistrut framework of the Main bank during assembly; (b) aluminum spacer with copper crush rings on both sides; (c) placing the upper half of the bank onto the lower half; (d) aligning the two halves of the bank with a 4 x 4 beam and cargo strap.	8
Figure 8.	Photo of the trigger board setup on the Main bank. The trigger board has been reduced to several smaller segments mounted onto a fiberglass frame that will move with the Main bank.	8
Figure 9.	(a) The Mylar packs from the Main bank stretched out uniformly on the ground plate below the Crowbar switch; (b) Crowbar and Main-bank Rogowski coils shown in place around the load-side Crowbar supports and the bottom-bus plate, respectively; (c) The Crowbar rail gaps suspended and rotated 180° so that the small Mylar pack can be affixed to its side; (d) the Crowbar switch Mylar is wrapped around the bank Mylar packs as the Crowbar switch is lowered into place.	9
Figure 10.	(a) Front view of the Main bank with fiberglass cable trays above to bring the Main bank and Crowbar switch trigger cables over from the trigger units. (b) Back view of the Main bank showing the Crowbar switch and the RG 17/14 transmission line cables to run to the Theta-coil-cable header.	10
Figure 11.	Photo showing the fiber optic cables in the aluminum bus plate over one of the Crowbar rail-gap switches. Simplex fiber optic feed-throughs in the plate hold	

	the fibers in place – ten per switch. Socket head bolts are used to plug the empty holes.	11
Figure 12.	Solid Works® rendering of the FTX PI bank that was prepared to guide assembly and identify hardware that was still needed. The design is essentially the same as the original two-capacitor (1.35 μ F each) FRX-L PI bank, except that a single 2.1 μ F capacitor was used instead, so FRX-L drawings were used to fabricate the remaining bank components.	12
Figure 13.	(a) The initial test-fit of hardware following its fabrication; (b) close-up view of the Mylar sheets attached to each side of the rail-gap switch, which serve as a flashguard; (c) the trigger board for the PI rail gap; (d) view of the nearly-completed bank in place just north of the Main bank.	13
Figure 14.	Design sketch of the Bias bank layout. Provision is made for having up to two 2.5 mF bank modules in the circuit. The bank module(s) is (are) connected to one or two ignitrons and the pair of inductors through a current limiting resistor (tan block). This resistor serves to prevent the Coulomb limit of the ignitrons from being exceeded.	14
Figure 15.	Photo of two of the “Slow Bank” modules that have been set in place between Shiva B and C Arms for use in the FTX experiment. The module in the foreground is intended for use in the Bias bank circuit, while the one in the background (and others still in storage) will be used for the other slow banks (Cusp, Guide, or Mirror).	15
Figure 16.	(a) Photo of the two parts of one of the Bias bank inductors: the outer return conductor (foreground) and the inner inductor winding itself (background). (b) The support stand for the inductors is shown along with the single ignitron that will be used initially to switch the Bias bank.	16
Figure 17.	Solid Works® rendering of the Theta coil cable header design. (a) The cable header is attached to the theta coil via a short parallel plate transmission line. The red cables in the header represent the PI bank cables, the blue cables are for the Bias bank, and the green cables are Main bank cables. (b) The top and side plates have been hidden to show the connection of the cable center conductors to the “hot” side of the header.	16
Figure 18.	Photos of the ground (a) and hot (b) sides of the cable header during test fitting. (c) The cable header with the Theta coil attached is shown next as it nears completion. (d) Once the Main bank transmission line cables have been inserted into the header, the clear Lexan cover is placed on top. (e) A capacitive voltage divider is set up nearby to measure the voltage at the Theta coil. Two Rogowski coils will measure the current. (f) Photo of the finished Theta coil load and cable header setup.	20
Figure 19.	Most recent conceptual layout of the field coils, vacuum vessel, and solid liner to enable translation of the FRC from the Theta coil to the solid liner.	21
Figure 20.	Photos of the ancillary components being set up between Shiva B- and C-Arms for the FTX (and F-LINCX) experiments: (a) the trigger (foreground) and power supply (background) units for the Main bank, and (b) the PI bank and Crowbar switch trigger units. (c) Lexan covers have been placed around the	

	isolation transformers powering each trigger system to protect personnel from exposed terminals on the transformers.	22
Figure 21.	(a) Three Jennings switches have been mounted on a wooden platform above the Main bank dump tank to lift the charging supply connections (positive and negative high voltage and ground) to the Main bank. (b) A Ross relay is being used on the PI bank (and on the other banks and trigger units) to lift the frame ground before a shot.....	24
Figure 22.	Photo of one of the charge and dump resistor stands, with the Jennings charge and dump switches mounted to it (upper right), on the FRX-L experiment. Bank voltage monitors are also mounted on these stands.....	24
Figure 23	A view looking down on the triggering systems and Main bank power supply between the B and C arms of the Shiva bank. The arrangement of the new three-raceway cable tray setup can be clearly seen in the upper portion of the photo.	25
Figure 24.	Cross-sectional diagram of the Shiva load region for the tall (30 cm), deformable-contact liner shot. The region both in and around the liner will be under vacuum, as will be the case when an FRC is to be compressed within the liner.	28
Figure 25.	Radiographic images of the middle (a) and bottom (b) portions of the MTF deformable-contact liner (DCL). The taper near the electrode surface (from $\phi = 11$ cm to $\phi = 10.2$ cm) is very obvious for the first 1 cm, but another more gradual taper continues from there for another 5 cm (reducing to $\phi = 10.0$ cm).....	29
Figure 26.	Radiographic images of the middle (a) and bottom (b) portions of the MTF DCL 20 μ s after current conduction began. The images show a nearly uniform radial compression in the central region of the liner with no indication of tearing near the electrodes.	29
Figure 27.	Radiographic images of the middle (a) and bottom (b) portions of the MTF DCL 22 μ s after current conduction began. The liner seems to be pinching slightly in the lower part of (a), but there is still no indication of tearing near the electrodes.	30
Figure 28.	Photographic image (negative) obtained from the gated MCP camera. The MCP was triggered at 20.85 μ s and had a 300 ns exposure window.	30
Figure 29.	Current waveforms measured by the Shiva arm Rogowski coils, the clockwise (CW) Rogowski coil, the counter-clockwise (CCW) Rogowski coil, and each of the three B-dot probes inserted through the liner return conductor. The waveforms have been scaled by the factors shown to the right of the graph.....	31
Figure 30.	AutoCAD drawing of the hardware configuration used in the second deformable contact liner shot. The black dashed lines indicate the center axis of the radiography pulser, the field of view of the pulser (dictated by the port in the steel I-beam in front of it), and the plane of the radiographic film pack.	32
Figure 31.	Current waveforms obtained with the Faraday rotation diagnostic, the clockwise (CW) and counter-clockwise (CCW) load Rogowski coils, and the six Shiva	

	arm Rogowski coils. Each Rogowski coil signal has been multiplied by a correction factor of 1.1.....	33
Figure 32.	Current waveforms obtained from the three B-dot probes inserted into the return conductor. The probes were spaced 120° apart azimuthally.....	33
Figure 33.	Static radiographic image of the deformable contact liner taken before the shot.....	34
Figure 34.	Radiographic image of the liner taken 20.96 μs after current delivery began.	34
Figure 35.	Radiographic images of the liner taken 21.88 μs after current delivery began.	34
Figure 36.	Plot of voltage across the Crowbar switch vs. time. Waveforms from shots with varying Main bank-to-Crowbar triggering delays (and one without the Main bank – #2340) are overlaid to show how the Crowbar triggering becomes worse as delay time is decreased.....	37
Figure 37.	Output signals from one of the flux loops around the vacuum vessel at the theta coil for the same shots as in Fig. 36. As delay decreases – and switch closure occurs later in time – the modulation in the flux increases and the average value drops.....	38
Figure 38.	Several load current waveforms recorded during AFRL Crowbar test shots. The quarter cycle time for the current was slightly longer than for FRX-L, being ~2.9 μs.	39
Figure 39.	Graph showing typical waveforms (unintegrated) obtained from Rogowski coils placed around trigger cables going to the west side and the two inner Crowbar rail-gap switches and to the west side Main bank rail-gap switch. The Main bank monitor signal was delayed by 1.845 μs to allow it to be displayed with the other signals.	39
Figure 40.	A graph of the same waveforms shown in Fig. 39 after they have been integrated. The Main bank monitor signal was again delayed (by 1.845 μs) to allow it to be displayed with the other signals.....	40
Figure 41.	Conceptual drawing of a Crowbar switch configuration allowing the center conductors of the RG 17/14 cables to be connected to bus plates running over the tops of the Crowbar rail gaps. Arrows indicate the current paths during the initial discharge and following the triggering of the Crowbar switch.	41
Figure 42.	Solid Works® rendering of the new crowbar switch design.	42
Figure 43.	End-on view of the Crowbar switch model shown in Fig. 42. Red circles highlight additional features suggested by FRX-L personnel at the design review: (I) an array of fiber optic feed-throughs above each rail gap; (II) an extension to Main bank bus plates; (III) notches in the bracket supporting rail gaps for Rogowski coils.....	43
Figure 44.	Photo of the new Crowbar rail gaps and several of the new Crowbar hardware items during a trial assembly at AFRL.	44
Figure 45.	FRX-L Crowbar switch installation: (a) view of the Crowbar rail gaps and ground bus work being mounted on the back of the Main bank; (b) the nylon anti-tracking tubes and Lexan side cover have now been placed on the cable header portion of the switch; (c) the Lexan end covers and the hot bus bar of the cable header have now been attached; (d) a view looking down on the FRX-L	

	Crowbar switch after the rail gap covers and gas feeds have been installed and the top bus plate over the switch has been bolted into place.	45
Figure 46.	Closer view of the crowbar current diagnostics: (a) four Rogowski coils (pushed up against the L-bracket when the Nylon anti-tracking tubes were installed) monitor the current flow in each rail-gap switch; (b) connections to the Rogowski coils are made at the west Lexan end cover.....	46
Figure 47.	Waveforms from a B-dot probe inserted in the top of Theta coil segment B. The red waveform was recorded during a shot with the old Crowbar switch and black during a shot with the new switch. The drop in flux density following the initial peak is only 27% with the new Crowbar switch, compared to 46% with the old. This drop is somewhat dependent on the extent of the trigger delay following the Theta coil current maximum.	47
Figure 48.	Current waveforms recorded with the Rogowski coils around each of the crowbar switch rail gaps. During typical shots it was observed that the current passing through the outer two rail gaps was higher than that passing through the inner two. Currents were often, but not always, balanced between the gaps in each pair, as shown here.	48
Figure 49.	Current waveforms recorded with the Crowbar Rogowski coils following the re-gapping of the inner two rail-gap switches. During typical shots it is now observed that the current is highest in gap 1 and steadily decreases toward gap 4.....	50
Figure 50.	(a) Solid Works® rendering of the Crowbar switch assembly with 1.27-cm-wide slots cut in the hot bus plates between the rail-gap switches. (b) Close-up view near one of the rail-gap switches to show the slot more clearly.	55
Figure 51.	Photos of (a) the bank side and (b) the Theta coil side of the new Crowbar switch slotted bus work during its test fitting. As is shown in (b), two single rail-gap switches were set out and spaced appropriately to allow the bolt-hole spacing and the sizes of parts to be checked.....	56
Figure 52.	(a) Four-segment Theta coil with passive mirror rings attached on the outside segments. (b) Cutaway view showing the outside segments of both sides of the Theta coil with their mirror rings.....	57
Figure 53.	Close-up view of one end of the Theta coil showing the step down in the inside radius of the mirror ring. The ring also has a lip that extends inside the bore of the Theta coil segment to aid with centering the ring.....	58
Figure E1.	Propagation of the voltage wave from a rail-gap switch after it closes.	E-2
Figure E2.	Propagation of the collapsing voltage wave between crowbar rail gaps. The view is from the Main bank looking toward the switch, and the angle bracket support has been made transparent so that the contacts on the rail gaps can be seen.	E-3
Figure E3.	Cross-sectional view of crowbar geometry. Regions set at ground and at high voltage in the Quick Field electrostatic simulation are noted, as well.....	E-4

Figure E4.	Illustration of how the collapsing voltage wave would have to propagate further to an adjacent rail gap if a slot were inserted into the bus plates and angle bracket.....	E-5
Figure E5.	Sketch of trigger circuit with second trigger cable added to double the trigger pulse amplitude.....	E-7
Figure F1.	Layout of the Quick Field simulation for the transmission line feed on back of Main bank going to the Crowbar switch and cable header. 0.12” of Mylar separate the upper plates from the lower plates. Between each upper-lower plate pair, there is the proposed 0.5”-wide slot in the bus plates.....	F-1
Figure F2.	Close-up of right side of the two conducting plates – current density contours are now shown for 0° phase with the scaling as indicated to the right. Field line plot and vector plot scales are the same as above.....	F-2
Figure F3.	Layout of the Quick Field simulation for the bus plate and angle bracket that are bolted to each side of the Crowbar switch. 7.725” (the width of the rail-gap switches) separate the top angle bracket segments in the sketch from the bottom plate segments. Between each bracket-plate pair, there is the proposed 0.5”-wide slot. (A 0.5” wide slot is actually already present in the angle bracket because of the Rogowski coils.).....	F-3
Figure F4.	Close-up of right side of the two conducting plates – current density contours are now shown for 0° phase with the scaling as indicated to the right. Field line plot and vector plot scales are the same as above.....	F-4
Figure G1.	Lumped-element circuit model of the FRX-L experiment that has been entered into MicroCap.....	G-1
Figure G2.	Current and voltage waveforms calculated by MicroCap using the FRX-L circuit model shown in Fig. G1.....	G-2
Figure G3.	Current and voltage waveforms calculated by MicroCap for case when the Bias bank is not triggered.....	G-3
Figure G4.	MicroCap circuit model of Dr. Intrator’s Bias bank/PFN concept.....	G-3
Figure G5.	Current and voltage waveforms calculated by MicroCap using the circuit model shown in Fig. G4.....	G-4
Figure G6.	The lumped-element FRX-L circuit model is shown again but with the Bias PFN circuit in place of the original Bias circuit.....	G-5
Figure G7.	Current and voltage waveforms calculated by MicroCap using the circuit model shown above in Fig. G6.....	G-5
Figure G8.	Plot of the voltage at the node between the load resistor and the ignitron and the voltages at the hot terminals of the stage 2 and stage 1 Bias bank capacitors. The initial charge voltage on the Bias bank capacitors was -8 kV.....	G-6
Figure G9.	A similar plot to that shown in Fig. G8, except that the initial charge voltage on the Bias bank capacitors was only -1 kV.....	G-7
Figure G10.	A plot of the same node voltages shown in Figs. G8 and G9 for the case when the Bias bank ignitron is not triggered.....	G-8

Figure G11. Overlay of the current waveforms calculated by MicroCap using the circuit diagrams shown in Figs. G1 and G6.....	G-9
Figure G12. Expanded view of the time period between 0 and 100 μ s from Fig. G11.	G-9
Figure G13. Overlay of the voltage waveforms calculated by MicroCap using the circuit diagrams shown in Figs. G1 and G6. The initial charge voltage on the Bias bank capacitors was -8 kV.	G-10
Figure G14. A second overlay of Bias bank voltage waveforms for the case when the initial charge voltage on the Bias bank capacitors was -1 kV.....	G-10
Figure G15. Overlay of the current waveforms calculated by MicroCap for the two FRX-L Bias bank configurations and the FTX (AFRL) Bias bank.....	G-11
Figure H1. Circuit model of a PFN configured to drive the FRX-L translation (Guide and Mirror) magnets.	H-1
Figure H2. Current and voltage waveforms calculated by MicroCap for the circuit shown in Fig. H1.	H-2
Figure H3. An alternative PFN circuit concept in which the translation (Guide and Mirror) magnets are now placed in parallel close to the load.....	H-2
Figure H4. Current and voltage waveforms calculated by MicroCap for the circuit shown in Fig. H3.	H-3
Figure H5. A PFN circuit similar to that in Fig. H3 but with a decreased stage inductance. ..	H-3
Figure H6. Current and voltage waveforms calculated by MicroCap for the circuit shown in Fig. H5.	H-4
Figure H7. A PFN circuit similar to those shown in Figs. H3 and H5 but with the stage inductance decreased still further.....	H-4
Figure H8. Current and voltage waveforms calculated by MicroCap for the circuit shown in Fig. H7.	H-5
Figure H9. Conceptual field coil designs and arrangement along the translation region and solid liner that will allow enable FRC translation from the Theta coil region into the liner.	H-6

List of Tables

Table 1.	Inductances of various elements in the FTX PI bank circuit. The target for the total inductance was ~209 nH to keep the ringing frequency of the bank close to that of the FRX-L PI bank.	12
Table 2.	Delay times between Main-bank triggering/current start and crowbar triggering/current start for several shots following the crowbar-switch re-gapping.....	52
Table C.1.	Pulsed Power Diagnostics for the FTX banks and Theta coil.	C-1
Table C.2.	FTX triggers and possible delay generator channels.	C-1

List of Acronyms

AFRL	Air Force Research Laboratory
FRC	Field Reversed Configuration
FRX-L	Field Reversed eXperiment – Liner
F-LINCX	Formation – LINer Compression eXperiment
FTX	Formation – Translation eXperiment
LANL	Los Alamos National Laboratories
MTF	Magnetized Target Fusion
PI	Pre-Ionization
SAIC	Science Applications International Corporation

EXECUTIVE SUMMARY

This report provides a summary of the involvement of Science Applications International Corporation (SAIC) and its subcontractors, FabTek, Inc. and NumerEx, in the Air Force Research Laboratory's (AFRL's) Task Order 36 under the Directed Energy HPM, PP, and PPS R&D contract. The work on Task Order 36 has been aimed at studying Magnetized Target Fusion (MTF) concepts with particular emphasis on a concept involving plasmas that are confined in a Field Reversed Configuration (FRC). Specific areas of work for SAIC and its subcontractors under this Task Order have included both supporting the continuing experimental work at Los Alamos National Laboratory's (LANL's) FRX-L (Field Reversed eXperiment – Liner) facility, the objectives of which have been to study the formation processes of the FRC as well as to characterize parameter regimes that will lead to reproducible formation of FRCs at MTF relevant plasma temperatures and densities, and starting a parallel experimental effort at AFRL's Building 322 on Kirtland Air Force Base, which will use this FRC knowledge base compiled at the FRX-L facility to form and translate an FRC into a cylindrical flux conserving shell (solid liner) that will then be imploded by the Shiva Star High Energy Capacitor Bank. Because the electrodes on each end of the liner must be open to allow the FRC to enter the liner before implosion, two liner-on-vacuum implosion experiments were performed to verify the uniformity of such an imploding liner over the open electrodes. During the period of this Task Order, SAIC personnel, along with AFRL personnel, have traveled to two conferences to report on the progress and findings of the work that is being performed, as is encouraged by the sponsor of this research, the Department of Energy's Office of Fusion Energy Studies (DOE OFES).

Sections 2 through 4, which follow, describe in detail SAIC's, FabTek's, and NumerEx's efforts in the principal areas of work mentioned above. Beginning in the next section, the planning, design, fabrication, and assembly of the primary hardware components of the AFRL experimental setup are discussed. A general layout of the experiment is also described, as is the concept for interfacing the FRC formation and translation portion of the experiment with the cylindrical solid liner that will be positioned underneath the center of the Shiva bank. The diagnostic results of the two liner-on-vacuum experiments that were performed are summarized in Section 3, and Section 4 outlines the areas of support that SAIC and FabTek personnel have been able to provide at the FRX-L facility. A brief mention is then made in Section 5 of the conference presentations and publications that have been prepared and written by SAIC personnel for the work on this project. Finally, in Section 6 a short summary recapping the major milestones of our efforts under this Task Order is given. This is followed by a short discussion of both the work that remains to be done at AFRL before FRC formation and translation experiments can begin (without solid liner implosion) and a long-term outlook towards the end objective of demonstrating this MTF concept in the integrated formation, translation, and liner implosion experiments.

1.0 DESIGN, FABRICATION, AND ASSEMBLY OF THE FRC FORMATION AND TRANSLATION EXPERIMENT AT AFRL

1.1 OVERVIEW

One of the primary objectives of Task Order 36 was to begin and advance as far as possible the assembly of the experimental apparatus at AFRL that would be needed to form and translate the FRC plasmas into a solid liner. Before starting any of the assembly work, it was determined that we should aim for duplicating electrically the FRX-L experiment and when possible attempt to duplicate the general configuration and the specific hardware components of the FRX-L experiment, as well (i.e., efforts to redesign or make other improvements in the experiment were to be kept to a minimum). These decisions were made with the intent of setting up the AFRL experimental in such a way that it should produce FRC plasmas very similar to those obtained with FRX-L. In practice, due size constraints around the Shiva bank, some design changes had to be made, as will be discussed below.

Also before starting any of the assembly on the experiment, efforts were made up front to inventory all of the hardware that was available in either Building 322 or in nearby storage facilities that could be used for this task. Major components that make up the FRX-L experiment – and that the AFRL experimental setup would also need – were written down, and this list, showing the components grouped according to the specific bank or system in which they are found, is presented in the table in Appendix A. Items that were found in the hardware inventory conducted at AFRL are noted in the second column of the table, and items that would have to be obtained through purchasing or some other means are noted in the third column. As can be seen, a good number of the items needed for the experiment, particularly the capacitor banks, were already available and in-house.

A tentative layout in the Building 322 high bay for the hardware of the FRC formation and translation apparatus (which will be referred to in this report as FTX, for “Formation-Translation eXperiment”, though an official name for the experiment has not yet been chosen) was also developed at this time and is shown below in Fig. 1. To reduce interference with other experimental setups and shots on the Shiva Star High Energy Capacitor Bank, the FTX is initially being assembled and tested in the northeast corner of the high bay. Capacitor banks for which transmission line inductance is critical (such as the Pre-Ionization, or PI, bank and the Main bank) have been kept close to the Theta coil and vacuum vessel assembly. These banks will then be moved with the Theta coil and vacuum vessel underneath the B-arm of the Shiva bank to the Shiva load region when making preparations for the FRC compression-heating (liner implosion) shots. (The combined FTX and Shiva experimental setup is being referred to in this report as F-LINCX, for “Formation-LINer Compression eXperiment”, though, again, an official name for the experiment has not yet been chosen.) The remaining “slow” banks, such as the Bias, Cusp, Guide, and Mirror banks, are being placed in a more central location between the Shiva B and C arms. Power supplies and trigger units are being placed at this location, as well.

A detailed circuit diagram showing the interconnections between each of the capacitor banks and the various coils around the vacuum vessel assembly is presented in Fig. 2. Note that the Main, PI, and Bias banks all have a common connection to the Theta coil, and this connecting point is at the Theta coil cable header. Note also that as a starting point for the field coil arrangement,

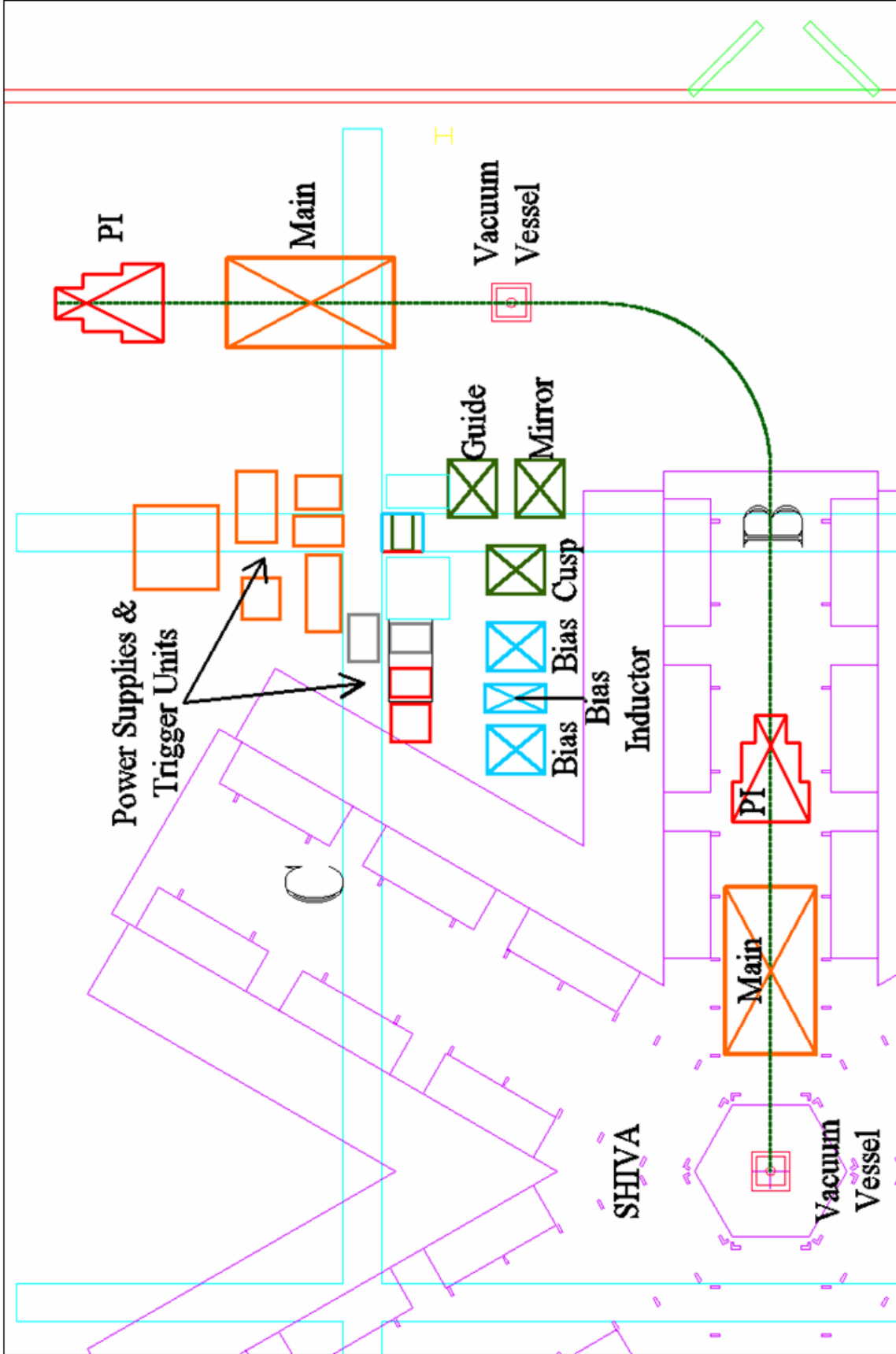


Figure 1. Proposed layout for the FTX/F-LINEX experimental hardware in the Building 322 high bay.

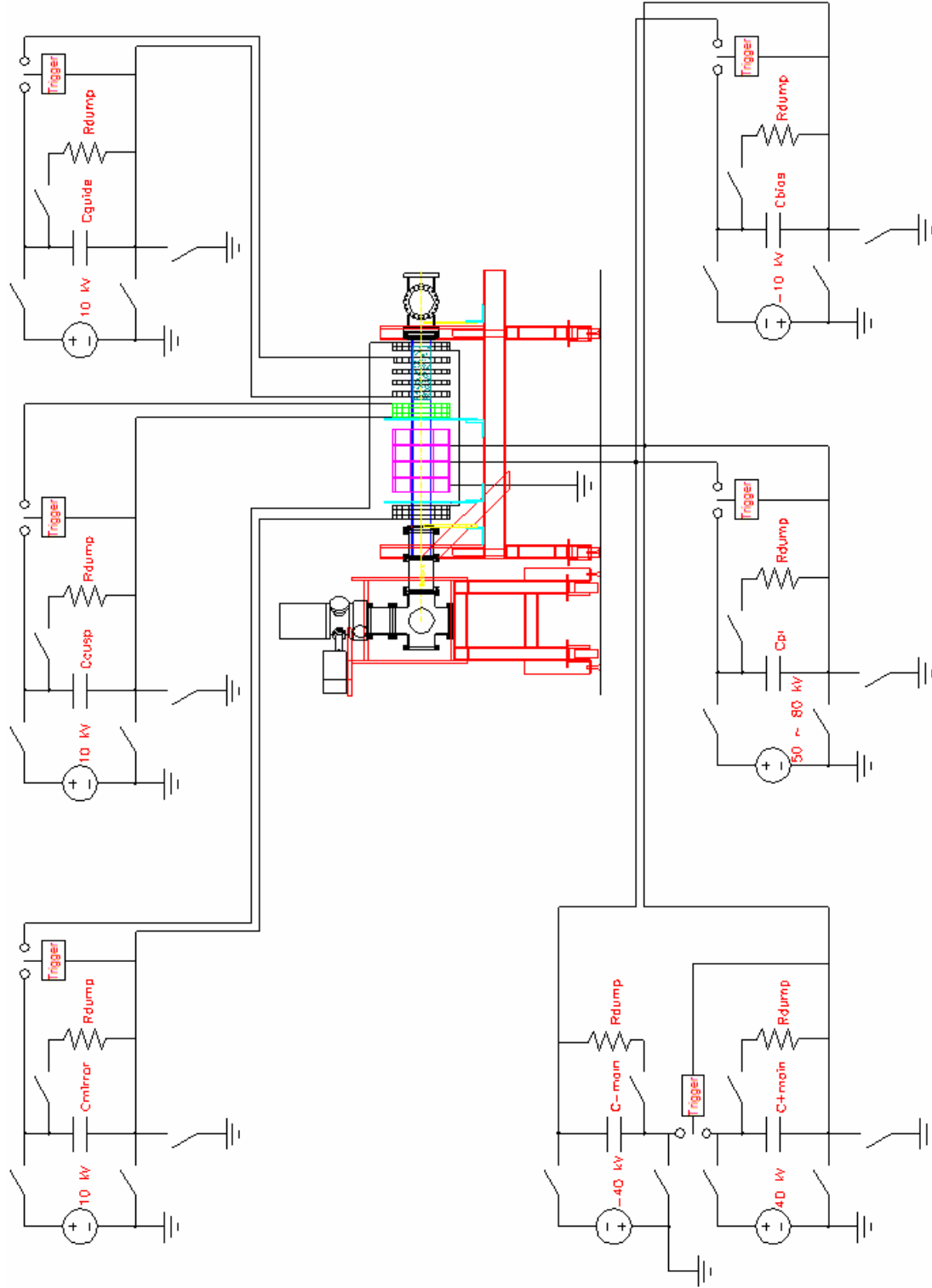


Figure 2. Global circuit diagram for the FTX capacitor banks and their trigger units and power supplies. Note that the FRX-L field coil configuration and vacuum hardware stand has been shown in this diagram to provide a starting point for the experimental design.

we have simply shown the horizontal configuration of the FRX-L field coils and vacuum hardware. In addition to helping define the number of capacitor banks that will be needed and their connections to the field coils, this diagram has also been useful as a guide for showing how the connections between the banks and their respective trigger units and charging supplies should be made. Because of the placement of diagnostics around the theta coils, the theta coil assembly has been chosen to be the single-point ground for the experiment, as is the case with FRX-L. To prevent ground loops, all ground connections to the individual banks will be lifted using Ross relays or Jennings switches just after the charging sequence is completed for each test shot. Trigger units will also be floated together with their respective banks to attempt to alleviate any possible triggering problems. This will be accomplished through the use of Ross relays again to lift the grounds on the trigger units and isolation transformers to float the AC power connections.

The next subsections discuss the design efforts and present status of each of the capacitors banks indicated in Fig. 2. Descriptions of the Theta coil cable header, the vacuum vessel with the various field coils arranged around it, the support systems (power supplies and trigger units) for the banks, the operations control system, and the diagnostics on the experiment are also provided in several of the other subsections below.

1.2 MAIN BANK AND CROWBAR SWITCH

The starting point for determining the configuration of the FTX Main bank was, of course, the FRX-L Main bank, and the FRX-L Main bank is essentially a standard Shiva bank module. The hardware listed in the table in Appendix A as being necessary to build up the Main bank – in particular the capacitors – was available from any of the three Formation bank modules located at the ends of Shiva A-, C-, and E-Arms, which are no longer being used. Some modifications were needed to the basic architecture of the bank, however, to allow it to fit under the Shiva B-arm (Fig. 1) when we are performing FRC compression-heating experiments. To reduce the overall height of the bank it was noted that we could rotate each capacitor by 90 degrees: the capacitors are 11” x 14” and instead of making the vertical dimension 14”, as is typically the case, the 11” side could be made vertical. Hot and ground bus plates, as well as the bank framework, then had to be remade, but it was still possible to use the quad rail-gap closing switch from one of the Formation bank modules after a wider flash-guard was bonded to it. Figure 3 shows an early Solid Works® rendering of this “mini-module” positioned underneath the Unistrut framework of a Shiva bank arm. Sufficient space exists to give the top and bottom rolls of Mylar approximately 6 inches of separation from the framework and the ground plane.

There has been some concern about the possibility of non-uniform current flow through the closing switch since the terminals of the capacitors closest to the closing switch are being moved even closer to it. The higher fields in the proximity of the capacitor terminals would lead to this non-uniformity, and the non-uniformity would manifest itself as reduced multi-channeling in the individual rail-gap switches. The reduced multi-channeling would then in turn result in higher erosion of the rail-gap electrodes.

To estimate whether or not the closer positioning of the capacitors was going to be a problem, the hot bus plates for the Main bank design were modeled in Quick Field. For simplicity, the rail-gap switches were considered to be uniformly conducting sheets in the model. Figure 4 shows a 2D plot of the current density distribution that Quick Field calculated for this arrangement. As can be seen, the regions nearest the edges of the rail gaps seem to be prone to

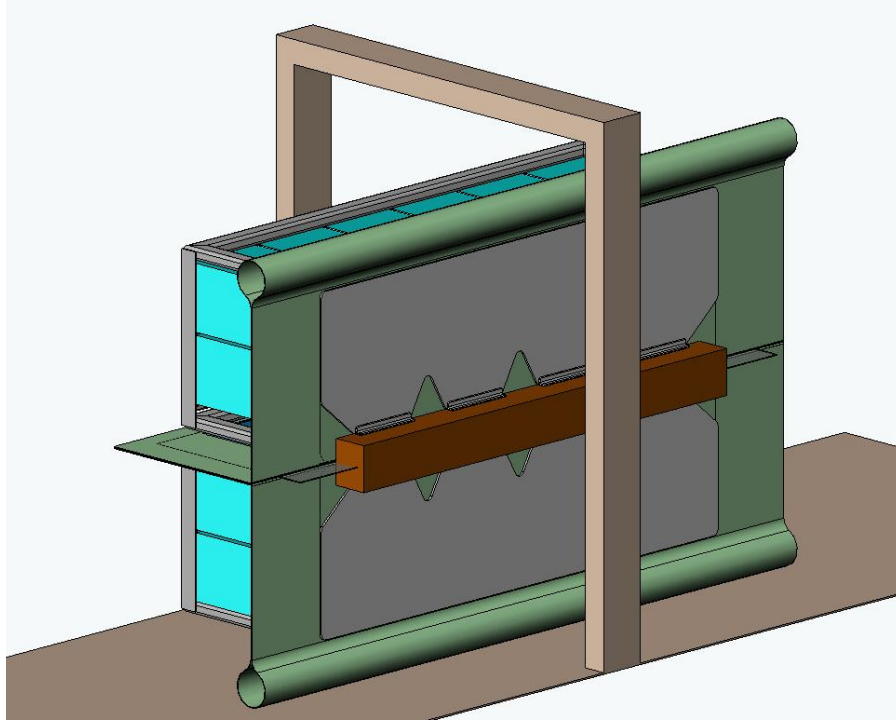


Figure 3. Solid Works® rendering of the FTX Main bank (“mini-module”) design. The brown frame shown has the same inner dimensions as the Shiva Unistrut framework, so it seems that there will be sufficient space for the Main bank under the Shiva arms.

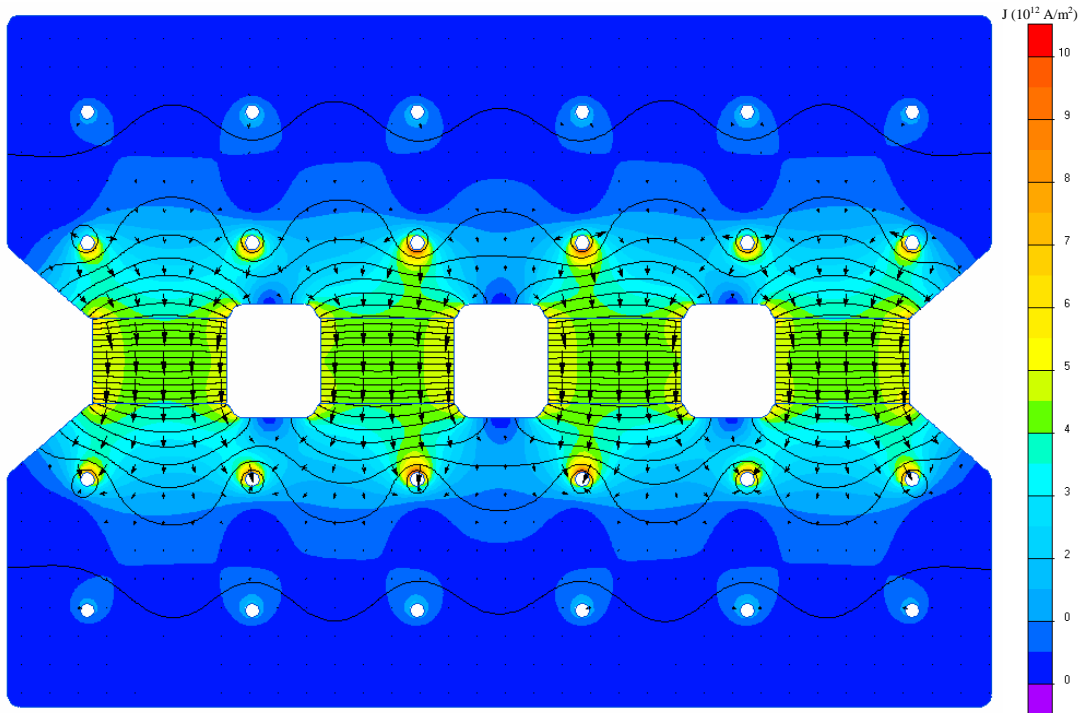


Figure 4. Quick Field calculation of the current density distribution in the hot bus plates of the FTX Main bank. The potential is +35 kV on the upper capacitor terminals and -35 kV on the lower capacitor terminals.

having a slightly higher current flow than the regions in the middle of each switch. As a means of redistributing the current flow, slots were then placed in the hot bus plates in the model between the capacitor terminals and the rail-gap switches. The plot in Fig. 5 indicates how several one-inch-wide slots in the upper and lower plates can help to increase the uniformity of the current distribution through each of the rail gaps.

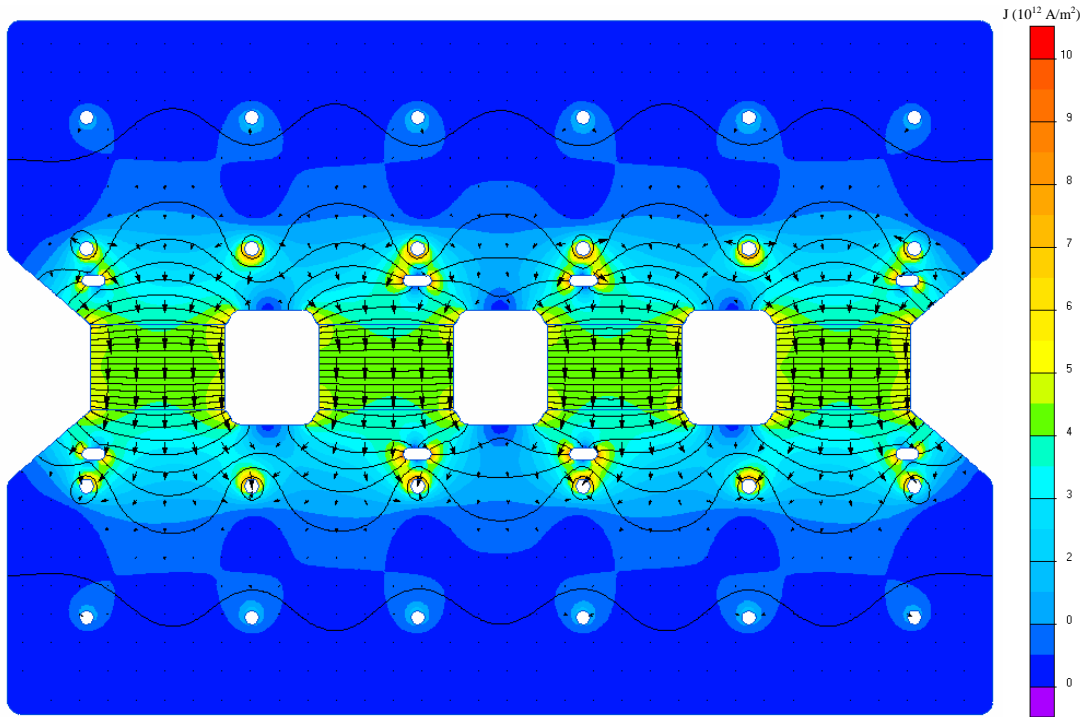


Figure 5. A second Quick Field calculation of the current density distribution in the hot bus plates of the FTX Main bank, however this time one-inch slots have been placed near several capacitor terminals to redistribute the current flow. The potentials on capacitor terminals are the same as in Fig. 4.

Once the appropriate sizes and positions of the slots were determined from the Quick Field modeling, work on preparing detailed drawings of all of the new hardware for the FTX Main bank began. In addition to the hot bus plate slots, the geometry of the bus work on the back of the bank was also modified relative to that of the Formation bank modules so that it would be more like the bus work on the FRX-L Main bank and would therefore readily mate up to the new Crowbar switch hardware (Fig. 6). (The lower-inductance Crowbar switch design will be described later in Section 4.)

After the drawings were completed, a final design review was held with AFRL and SAIC personnel attending to determine if any details in the design had been overlooked or needed to be changed. Following the review and only a few minor corrections to the drawings, all drawings were sent out to local machine shops for bids and parts fabrication. Drawings for a set of Crowbar switch hardware for our Main bank were also sent out at the same time, so that the Crowbar could be fabricated and assembled in parallel with the Main bank. By August of 2005 the parts for both had started arriving in house from the machine shops, and assembly was quickly started.

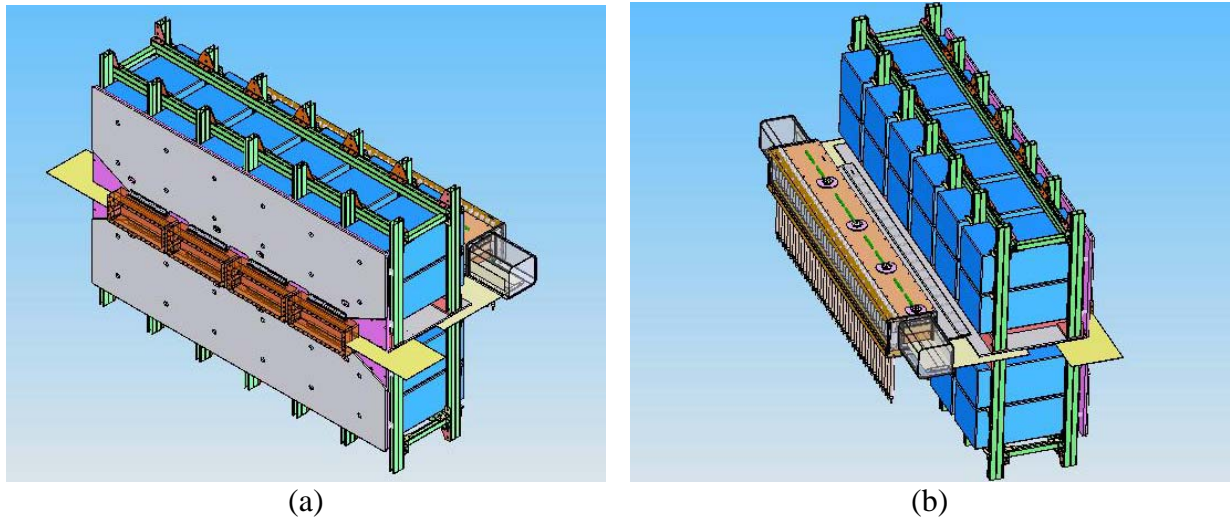


Figure 6. (a) Front and (b) back views of the final FTX Main bank design. The back view also shows the new Crowbar switch in place on the bank.

Figure 7 shows several photographs of the Main bank during the assembly process. Unistrut pieces were mounted first to two welded portions of the bank framework (Fig. 7a), after which the two sets of “ground” bus plates were then bolted onto the two framework assemblies. Next, the capacitors were inserted into the pockets in the frames and bolted to the ground plates. Aluminum spacers with copper crush rings on each end were inserted into polyurethane “doughnuts” (Fig. 7b), and these were then placed in the headers of each of the capacitors. The spacer is used to electrically connect each capacitor to the hot bus plates on the bank, and the polyurethane doughnut is squeezed tightly into the volume around the aluminum spacer in the header to remove any air pockets and serve as a high voltage insulator. Mylar packs consisting of 12 sheets of 5-mil Mylar and one sheet of brown craft paper, with holes cut for each of the aluminum spacers, were then placed over the ground bus plates on both frames. (The brown craft paper has been found to be effective in helping to grade the voltage away from the hot bus plates and thereby suppress surface flashover on the Mylar.) Once the Mylar packs were in place, the hot bus plates were attached to the vertical faces of the bank sections using 1-in.-diameter bolts that ran through the aluminum spacers and threaded into the capacitor headers.

At this point the two sections of the bank were ready to be joined together. The closing-switch assembly was first bolted onto the hot bus plate of the lower bank half and supported with several wooden beams. Next, the top half of the bank was hoisted by crane over to the lower half and rested “lightly” on top of it (Fig. 7c). When the alignment of the two halves was observed to be good, the weight of the upper half was taken off the crane and allowed to rest fully on the lower half (Fig. 7d). The rail-gap switches were then bolted to the upper hot bus plate, completing the assembly of the basic bank structure.

Once the key parts of the bank were assembled, personnel began to focus on assembling both the trigger board for the closing switch on the front of the bank and the hardware for the Crowbar switch on the back. Regarding the closing switch trigger board, due to the tight spaces that the Main bank must fit into under the Shiva bank, it was necessary to look at ways of reducing its size. The end result (shown in the photo in Fig. 8) was that the single acrylic board typically placed ~12 ½ in. away from the bank was changed to two narrow, parallel acrylic strips above



(a)



(b)



(c)



(d)

Figure 7. (a) The Unistrut framework of the Main bank during assembly; (b) aluminum spacer with copper crush rings on both sides; (c) placing the upper half of the bank onto the lower half; (d) aligning the two halves of the bank with a 4 x 4 beam and cargo strap.



Figure 8. Photo of the trigger board setup on the Main bank. The trigger board has been reduced to several smaller segments mounted onto a fiberglass frame that will move with the Main bank.

and below the rail-gap switches, and both are now placed about 6 ¾ in. from the bank. Both of the narrow boards, along with a third acrylic plate for the biasing resistors, are mounted to a fiberglass frame that is in turn mounted to the bank so that it all can be moved with the bank.

Assembly of the Crowbar switch on the back of the Main bank followed nearly the same procedure as for the FRX-L Crowbar switch, as had been anticipated. Figure 9 shows several photos of the switch as it was being assembled. The Mylar packs from the two halves of the Main bank were laid out uniformly onto the ground plate below where the Crowbar switch sits, where they were then cleaned one more time (Fig. 9a). After cleaning, the Mylar was



Figure 9. (a) The Mylar packs from the Main bank stretched out uniformly on the ground plate below the Crowbar switch; (b) Crowbar and Main-bank Rogowski coils shown in place around the load-side Crowbar supports and the bottom-bus plate, respectively; (c) The Crowbar rail gaps suspended and rotated 180° so that the small Mylar pack can be affixed to its side; (d) the Crowbar switch Mylar is wrapped around the bank Mylar packs as the Crowbar switch is lowered into place.

temporarily taped back against the bank while Rogowski coils were placed through the slots in the load-side support bracket for the rail gaps and around the ground plate (Fig. 9b). Next, when the Rogowski coils were in place, the Mylar was laid back down, and the set of Crowbar switch rail gaps was lifted with the crane and positioned over the back of the bank. Before lowering them into place, a second short pack of 12 sheets of 5-mil Mylar was sandwiched between the bank-side support bracket and the rail gap assembly (Fig. 9c), and a bead of silicone RTV was run between the Mylar and the switch bodies to form a seal that will prevent arcing across the bottom surfaces of the switches. (Note that in this photo the Crowbar rail gaps have been rotated 180° so that personnel can readily attach the bracket and run the bead of RTV.) After the RTV dried, the Crowbar rail gaps were finally lowered slowly into place on the back of the bank, with the new Mylar pack that was attached to the switch being tucked under the Main bank Mylar as it was lowered (Fig. 9d). This scheme has so far proven effective for suppressing any breakdown around the Crowbar switch rail gaps on FRX-L. As can be seen in Fig. 9c Unistrut supports have been attached to the bank framework to provide a means of supporting the weight of the Crowbar switch.

With assembly of the Crowbar switch completed, trigger and charge cables were then run to the bank and Crowbar switch, along with the various gas lines required by the rail-gap switches (SF_6/Ar), the peaking gaps on the Crowbar switch trigger board (compressed air), and the Crowbar cable header (SF_6). A cable tray system was set up above the bank to help with running the numerous cables over to it, while gas lines were run through the building cable trays in the floor. Figure 10 shows two final photos of the setup with all of these cables and gas lines in place.

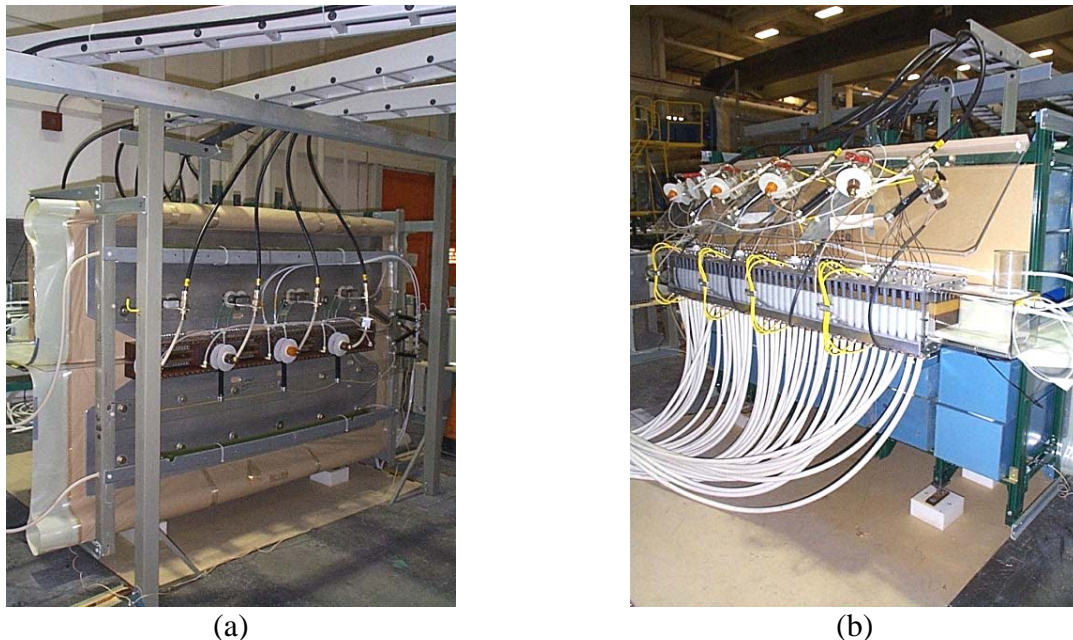


Figure 10. (a) Front view of the Main bank with fiberglass cable trays above to bring the Main bank and Crowbar switch trigger cables over from the trigger units. (b) Back view of the Main bank showing the Crowbar switch and the RG 17/14 transmission line cables to run to the Theta-coil-cable header.

At this time there is one final task that remains to be completed to ready the Main bank and Crowbar switch for testing. Due to the solid aluminum plate covering the top of the Crowbar switch, it is not possible to take open shutter photos of the switch during shots to verify multi-channeling. As a result, an array of fiber optic cables, ten per rail-gap switch for the FTX Crowbar, has been set up instead to observe the arc channels in the switches (Fig. 11). As is indicated by the photo, the ends of these fibers have been inserted into feed-through ports in the plate, and then the fibers have been run through one of the upper cable trays back to the Main bank power supply, which actually provides a convenient location to set up an open-shutter camera to image the ends of these fibers. The set up of this camera is expected to take place within the next couple of weeks.



Figure 11. Photo showing the fiber optic cables in the aluminum bus plate over one of the Crowbar rail-gap switches. Simplex fiber optic feed-throughs in the plate hold the fibers in place – ten per switch. Socket head bolts are used to plug the empty holes.

1.3 PRE-IONIZATION BANK

Given the general layout of the FTX hardware that is shown in Fig. 1, the RG 17/14 transmission line cables from the Pre-Ionization bank needed to be somewhat longer than those on the FRX-L PI bank. To then maintain the same oscillation frequency (~ 240 kHz) during the FTX PI bank discharge either a reduction in inductance somewhere else in the circuit or a smaller bank capacitance was required (based upon the relation $\omega^2 = (2\pi f)^2 = 1/LC$). Initial analyses of the overall PI bank circuit suggested that reducing the bank capacitance and working with a higher bank charge voltage was the more feasible approach.

Presently two 100 kV, 1.35 μF capacitors are being used on the FRX-L PI bank, giving a total bank capacitance of 2.7 μF . At AFRL, in addition to having many of the same 100 kV, 1.35 μF capacitors on hand, several 100 kV, 2.1 μF capacitors were available for use, as well. By using only one of the 2.1 μF capacitors, the inductance “limit” for the PI bank could be increased from 163 nH to 209 nH. This inductance is broken down among the various elements in the PI bank circuit in Table 1. The inductance values for the 2.1 μF capacitor and the rail-gap switch inductance are those specified by the manufacturer, while the inductances for the bank cable header, bus plates, and the theta coils were calculated based upon both geometry and FRX-L experimental results. The RG 17/14 cables have an inductance of 42 nH/ft; with a minimum

Table 1. Inductances of various elements in the FTX PI bank circuit. The target for the total inductance was ~209 nH to keep the ringing frequency of the bank close to that of the FRX-L PI bank.

PI Circuit Element	Stated/Calculated Inductance (nH)
Capacitor	30
Rail-Gap Switch	20
Bus Plates	5
Bank Cable Header	10
RG 17/14 Cables	78
Theta Coil Cable Header	35
Theta Coils	31
Total	209

estimated length of 22 feet between the PI bank and the Theta coil cable header, 12 parallel cables can be used to lower the transmission line inductance to ~78 nH. This then leaves 35 nH for the Theta coil cable header. As will be discussed shortly in Section 2.5 on the Theta coil cable header design, it was possible to tailor the design and PI cable positions in the header to achieve an inductance very close to this (36 nH).

Once the general circuit of the bank had been decided upon, the design concept sketch shown in Fig. 12 was prepared to aid with identifying hardware that needed to be fabricated and, later, with the actual assembly of the bank. In keeping with the goal of duplicating the FRX-L

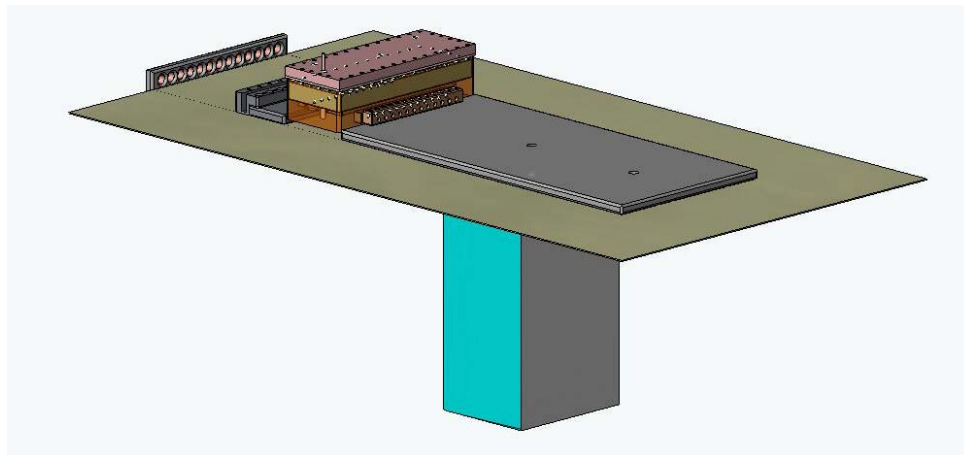


Figure 12. Solid Works® rendering of the FTX PI bank that was prepared to guide assembly and identify hardware that was still needed. The design is essentially the same as the original two-capacitor (1.35 μ F each) FRX-L PI bank, except that a single 2.1 μ F capacitor was used instead, so FRX-L drawings were used to fabricate the remaining bank components.

experiment as much as possible, several key components used to construct the FTX PI bank – in particular, the hot and ground capacitor plates and the rail-gap switch – are actually from the original FRX-L PI bank. This hardware was being kept in storage at the FRX-L facility and has been readily loaned to us by FRX-L personnel. Drawings of the remaining FRX-L PI bank hardware, which had been provided by FRX-L personnel some time earlier, were then used to fabricate the remaining parts needed for the FTX bank.

The photos in Fig. 13 show the PI bank during the early stages of assembly and in its present, nearly-completed state. Once the newly fabricated hardware had arrived in house, all of the bank hardware, including the pack of insulating Mylar sheets, was put together for a trial fitting (Fig. 13a). After the trial fitting, everything was disassembled once again and the capacitor header, with an aluminum spacer on the hot terminal, was potted with Dow Corning 3110 RTV rubber. The RTV rubber serves the same purpose (electrical insulation) as the blue polyurethane doughnuts in the headers of the Main bank capacitors (Fig. 7b) but the potted RTV material was used here because there were no pre-made insulators already on hand for these capacitors. This procedure is actually the same as that followed in fabricating the FRX-L PI bank, as well.

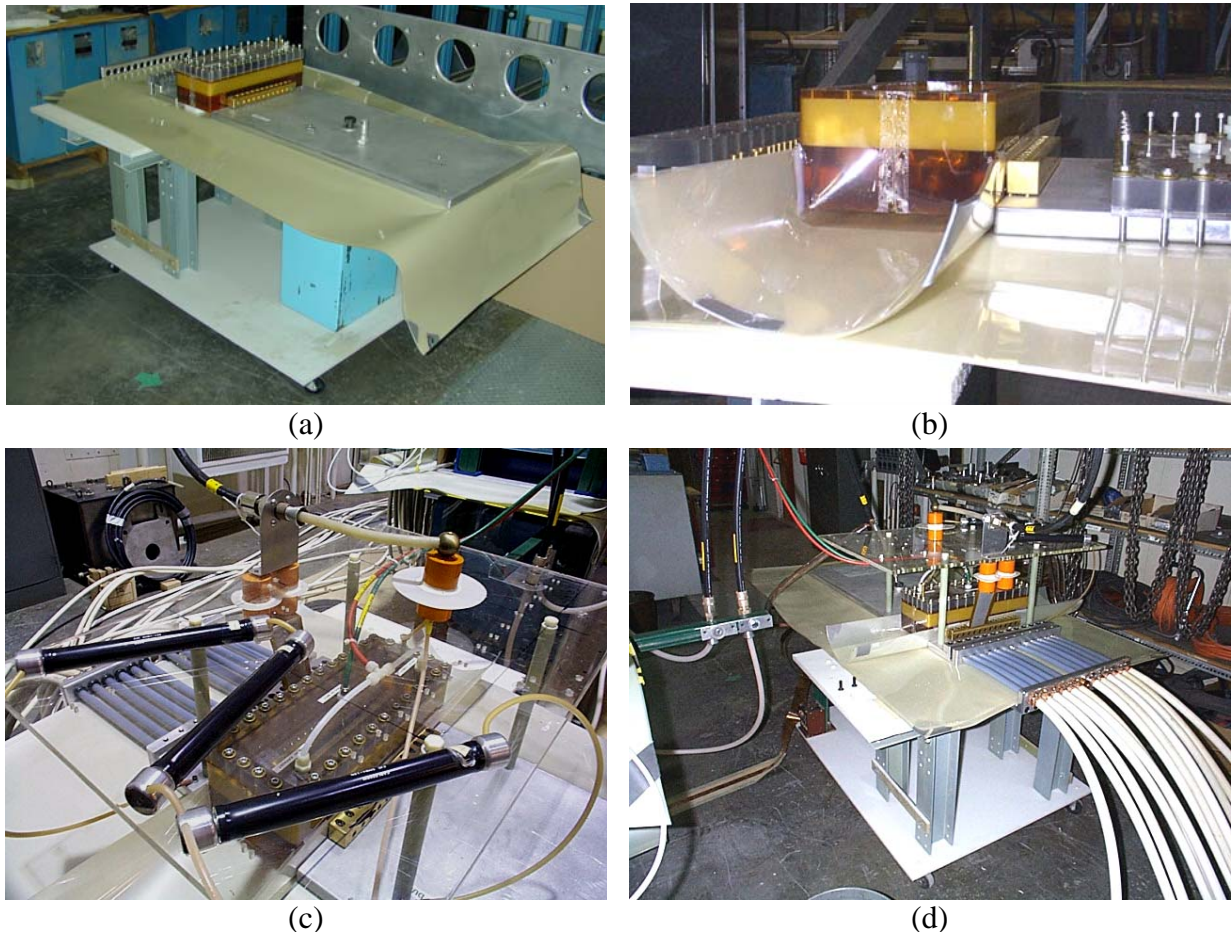


Figure 13. (a) The initial test-fit of hardware following its fabrication; (b) close-up view of the Mylar sheets attached to each side of the rail-gap switch, which serve as a flashguard; (c) the trigger board for the PI rail gap; (d) view of the nearly-completed bank in place just north of the Main bank.

Once the Dow Corning RTV rubber had cured, all of the bank hardware was again carefully assembled, but before torquing the upper bus plate down onto the capacitor terminal, several additional Mylar sheets were bonded to each side of the rail-gap switch with a silicone RTV, as was done with the Crowbar rail-gap switches, to prevent tracking around or under the switch body when the bank is charged (Fig. 13b). Next, the rail electrodes were removed from the switch so that the bolt holes could be slotted to allow for a smaller gap spacing in the switch, which is needed for the relatively low voltages that the PI bank will be charged to. Lastly, a trigger board was fabricated for the few trigger components needed for the single rail-gap switch, and the 22-ft RG 17/14 transmission line cables were terminated and installed in the bank cable header (Fig. 13c). A box structure around the cable header is still required at this time so that the header can be insulated with SF₆. Drawings for the pieces for such a box have already been prepared, and fabrication is expected to begin within the coming week. Figure 13d shows a photo of the PI bank in its nearly completed state.

1.4 BIAS BANK

As with the FTX PI bank circuit just described, the Bias bank circuit is being fabricated primarily using hardware that was already in house with some additional new parts being machined as needed. Using the FRX-L Bias bank current waveforms and circuit parameters as a guide, SAIC personnel have developed the hardware layout for the FTX Bias bank shown in Fig. 14. For the principle component, the capacitor bank itself, a number of 2.5 mF capacitor bank modules from an earlier experimental setup (the “Slow Bank”) have been in storage at AFRL for some time and can be used here. SAIC personnel have moved two of these former Slow Bank modules into the FTX work area in the high bay (Fig. 15), and the first is being prepared for use as the Bias bank.

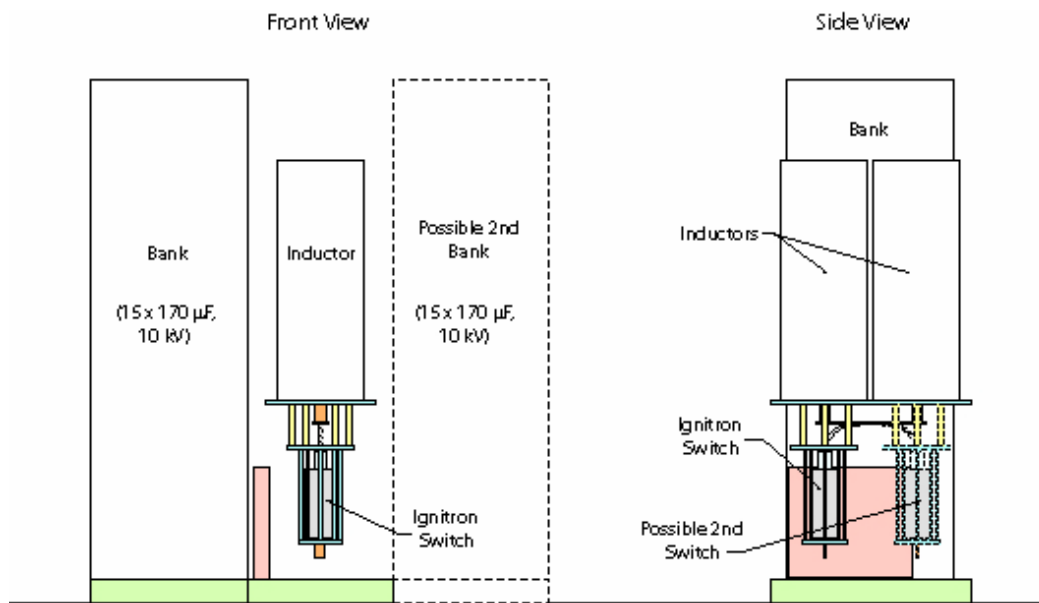


Figure 14. Design sketch of the Bias bank layout. Provision is made for having up to two 2.5 mF bank modules in the circuit. The bank module(s) is (are) connected to one or two ignitrons and the pair of inductors through a current limiting resistor (tan block). This resistor serves to prevent the Coulomb limit of the ignitrons from being exceeded.



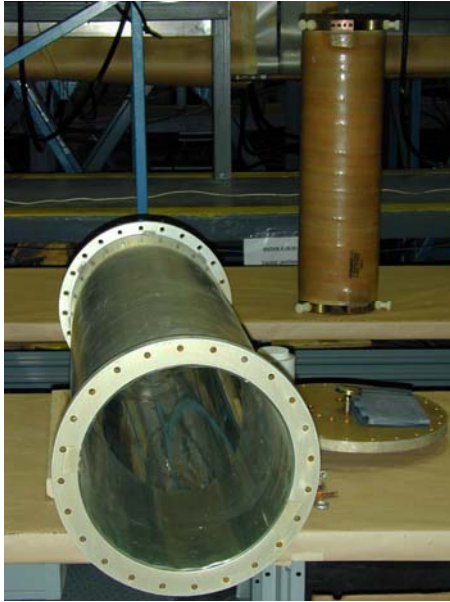
Figure 15. Photo of two of the “Slow Bank” modules that have been set in place between Shiva B and C Arms for use in the FTX experiment. The module in the foreground is intended for use in the Bias bank circuit, while the one in the background (and others still in storage) will be used for the other slow banks (Cusp, Guide, or Mirror).

Going through the diagram in Fig. 14, the bank is connected to an ignitron switch and then to two inductors through a $6.8\text{ m}\Omega$ current limiting resistor. The two inductors ($\sim 4.4\text{ }\mu\text{H}$ each) were borrowed from the FRX-L facility several months ago (Fig. 16a) and are identical to the ones presently being used in the FRX-L Bias circuit. As can also be seen from the Fig. 14 drawing, the ignitron switch is mounted below the inductors (Fig. 16b), and the transmission line cables going to the Theta coil cable header will then exit from the top of the inductors. Provision is also made in this layout for the addition of a second bank module and ignitron if it is determined that a larger Bias current is eventually needed for FRC formation experiments.

Presently, most of the hardware pieces needed for Bias bank have already been fabricated and are in house. The only two components that remain to be fabricated are the $6.8\text{ m}\Omega$ current limiting resistor and the base plate on which everything will be mounted. Work on drawings for these items and their fabrication should be completed within the coming month.

1.5 THETA COIL CABLE HEADER

The previous three subsections have discussed the principle capacitor banks required for FRC plasma formation. All three of these banks drive the same field coil, which is referred to as the “Theta coil” since the FRC is really a form of a reversed-field theta pinch. Deviating at this point from our guidelines of trying to keep everything on the FTX experiment very similar to FRX-L, a considerable amount of time was spent redesigning the cable header required to connect the transmission line cables from the PI, Bias, and Main banks to the Theta coil. Like the FRX-L Main bank with its Shiva-module-style configuration, the cable header design currently in use at FRX-L is too large to fit underneath the Shiva bank, so a more compact design had to be considered. Figure 17 shows an illustration of such a design.

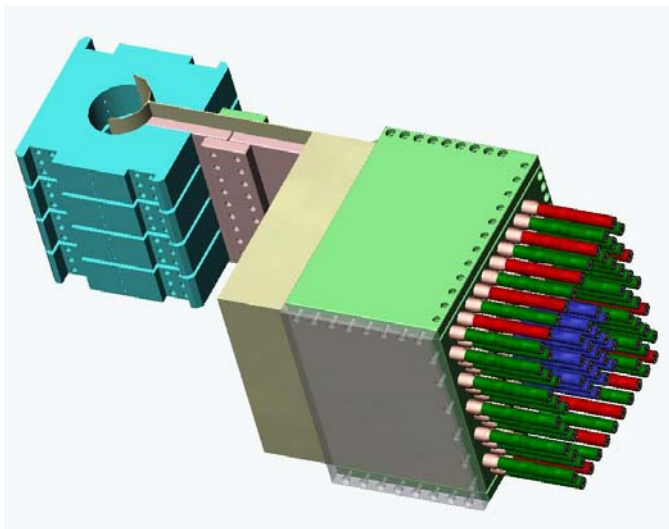


(a)

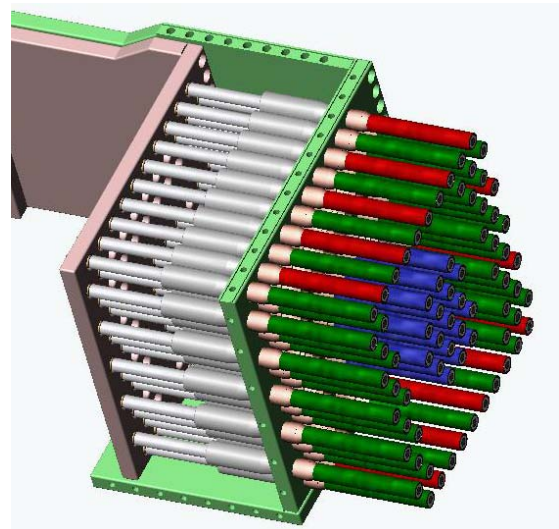


(b)

Figure 16. (a) Photo of the two parts of one of the Bias bank inductors: the outer return conductor (foreground) and the inner inductor winding itself (background). (b) The support stand for the inductors is shown along with the single ignitron that will be used initially to switch the Bias bank.



(a)



(b)

Figure 17. Solid Works® rendering of the Theta coil cable header design. (a) The cable header is attached to the theta coil via a short parallel plate transmission line. The red cables in the header represent the PI bank cables, the blue cables are for the Bias bank, and the green cables are Main bank cables. (b) The top and side plates have been hidden to show the connection of the cable center conductors to the “hot” side of the header.

With this header design, the transmission line cables are connected to the hot and ground bus plates in a matrix fashion, and the bus plates are in turn connected to two short parallel plates, to

which the theta coil segments are bolted at the other end. Side plates that are electrically connected to both the grounded bus plate and the bottom parallel plate have been added to the header in an attempt to lower its inductance. (When the header is set up in its correct orientation, which will align the bore of the Theta coil with the vertical axis, these side plates will be more correctly labeled “top” and “bottom” plates.) A clear Lexan plate has also been placed on the top of the header so that the volume around the cables inside can be sealed off and filled with SF₆ for added electrical insulation. The transparency of the Lexan plate will also allow personnel to visually inspect the cables inside without any disassembly. All ground-potential plates are kept isolated from the hot bus plate and the top parallel plate by the Mylar sheets that are shown in light yellow in Fig. 17a.

The key parameter of interest for this cable header design is its inductance. While not terribly critical for the Main bank and not even noticeable to the Bias bank, the header inductance is an important parameter for the PI-bank circuit, as it is the high-frequency ringing of the bank discharge (~240 kHz) that facilitates the gas breakdown in the vacuum vessel. As was mentioned in the discussion in subsection 2.3, the net Theta coil cable header inductance for the PI circuit had to be limited to ~35 nH. If the inductance was higher than this, either another Theta coil cable header design would have to be developed or the proposed PI bank circuit would have to be reconsidered.

To calculate the net inductance that this particular Theta coil cable header design would add to the PI bank circuit a method that is outlined in Grover’s *Inductance Calculations* (F. W. Grover, “*Inductance Calculations: Working Formulas and Tables*,” Dover Publications Inc., 1973) was used. This method centers around the relation shown on page 31 for the mutual inductance between two current elements:

$$M = 0.002\ell \left[\log_e \left(\frac{\ell}{d} + \sqrt{1 + \frac{\ell^2}{d^2}} \right) - \sqrt{1 + \frac{d^2}{\ell^2}} + \frac{d}{\ell} \right]. \quad (1)$$

Here ℓ is the length of the current elements and d is their distance apart in cm. For solid cylindrical or annular conductors, d is simply the distance between the center axes of the conductors. However, when the conductors have other than circular cross sections (such as the case for the return conductors in our cable header), the geometric mean distance between the conductors must be calculated and used for d in Eqn. (1). The geometric mean distance between two rectangular conductors, with cross-sectional areas of A_1 and A_2 , is given by

$$\text{G.M.D.} = \frac{1}{A_1 A_2} \int_{y_{2a}}^{y_{2b}} \int_{x_{2a}}^{x_{2b}} \int_{y_{1a}}^{y_{1b}} \int_{x_{1a}}^{x_{1b}} \ln \left[\sqrt{(x-v)^2 + (y-w)^2} \right] dv dw dx dy. \quad (2)$$

Geometric mean distances between conductors of other cross sections can be evaluated by changing the limits of integration to reflect the different area profiles. The geometric mean distance of an area from itself can be calculated by letting $x_{1a} = x_{2a}$, $x_{1b} = x_{2b}$, and so on. When this calculation is done and substituted for d in Equation (1), the self-inductance of a conductor is obtained. The total inductance of a pair of conductors may then be calculated using the expression

$$L_{\text{Tot}} = L_1 + L_2 \pm 2M, \quad (3)$$

where L_1 , L_2 , and M are all calculated from Equation (1) using the appropriate geometric mean distances.

Evaluating the inductance of the Theta-coil-cable-header design requires a few additional steps because there are actually 12 PI cables carrying current to the Theta coils and three sections of aluminum plate carrying current back. To calculate the geometric mean distance of Conductor 1 from an ensemble of three conductors, of which Conductor 1 is a part, the expression

$$\text{GMD}_{-1T} = \text{Exp} \left[\frac{A_1 \ln(\text{GMD}_{-11}) + A_2 \ln(\text{GMD}_{-12}) + A_3 \ln(\text{GMD}_{-31})}{A_1 + A_2 + A_3} \right] \quad (4)$$

is used, where GMD_{-1T} , GMD_{-11} , GMD_{-12} , and GMD_{-31} are the geometric mean distances of Conductor 1 from the ensemble, from itself, from Conductor 2, and from Conductor 3, respectively, and A_1 , A_2 , and A_3 are the cross-sectional areas of the three conductors. Similar expressions can be written for GMD_{-2T} and GMD_{-3T} . The geometric mean distance of the ensemble from itself can then be found by taking a logarithmic average of GMD_{-1T} , GMD_{-2T} , and GMD_{-3T} :

$$\text{GMD}_{-T} = \text{Exp} \left[\frac{A_1 \ln(\text{GMD}_{-1T}) + A_2 \ln(\text{GMD}_{-2T}) + A_3 \ln(\text{GMD}_{-3T})}{A_1 + A_2 + A_3} \right] \quad (5)$$

Following this somewhat tedious process, with the aid of MathCAD to perform the calculations, the self-geometric mean distance of the ensemble of return-conductor plates from itself and the self-geometric mean distance of the ensemble of cables from themselves were found, and each was plugged into Equation 1 to find the self-inductances of the respective ensemble. A self-geometric mean distance of the entire ensemble of cables and return conductor plates from itself was calculated to find the net mutual inductance of the system.

The final inductances that were obtained were dependent upon the locations selected for the PI cables in the header, as might be expected. When the cables were placed closest to the return conductor and somewhat apart from each other, the net inductance appeared to be minimized. For the PI cable arrangement shown above in Figure 17, where the PI cables are the red cables, a final inductance of ~ 36 nH was obtained, only 1 nH higher than the target value. Once the PI bank is finally assembled, other stray inductances will likely come into play, as well, but if the values of these inductances are not overly large the resulting decrease in frequency should be minimal. The final FTX PI frequency should then actually end up being quite close to that of the FRX-L PI bank (which has been measured to be closer to 238 kHz).

Once the inductance of this header design was determined to be sufficiently low for the PI bank, SAIC mechanical engineers began working on the detailed drawings needed to fabricate each of the header parts. After the drawings were completed, a design review was held with AFRL and SAIC personnel attending, and with the exception of noting a few very minor changes that should be made first (e.g., increasing the radii on some of the corners), it was decided to proceed with the fabrication of the header parts. Fabrication was then completed by the beginning of February 2006, and as soon as the parts were shipped to our facility personnel started test fitting

each of the components to verify tolerances. Unfortunately, a number of fabrication errors were discovered during this process. While the errors slowed the final assembly of cable header somewhat, it was possible to correct (or have the fabricating shop correct) each of the errors without too much difficulty. Figure 18 shows several photos of the cable header during the test fitting (Figs. 18a - 18b) and the final assembly process (Fig. 18c). Details of the completed setup and the pulsed power diagnostics put into place around the Theta coil are seen in the photos in Figs. 18d – 18f.

It should be noted that the radius at the end of the new transmission line plate to which the Theta coil segments are bolted is slightly larger (by 0.5 cm) than the radius of the Theta coil segments. Our Theta coil segments were fabricated several years ago at the same time that a second set of FRX-L Theta coil segments was fabricated, but since that time the FRX-L Theta coil radius has been bored out an additional 0.5 cm to provide more room for excluded flux loops. In the near future we anticipate making a similar modification to our Theta coil segments or, more likely, shifting to a set of thinner Theta coil segments having an overall conical bore that FRX-L personnel have started designing for their translation setup. (The thinner segments and the greater number of them allow the resulting Theta coil to maintain a length that is similar to the present coil while at the same time open up greater diagnostic access to the formation region within their bore.)

1.6 CUSP, GUIDE, AND MIRROR BANKS

The present FRX-L Cusp coil circuit utilizes a 1-mF bank, with a single ignitron switch, to drive six of the Cusp coil windings in varying series and parallel combinations. FRX-L personnel are exploring the possibility, however, of operating without the Cusp coils, as the Cusp field extends well into the Theta coil region, and the Bias bank discharge must overcome it to establish the background Bias field before FRC formation.

As was mentioned above in Subsection 2.4 when discussing the FTX Bias bank, a second “Slow Bank” module has already been moved into place for use as a Cusp bank should it be necessary to continue providing a Cusp field for reliable and reproducible FRC formation. SAIC personnel will finish the assembly of the Bias and PI banks and then evaluate whether or not to proceed with setting up a Cusp bank and an appropriate number of transmission line cables to drive the Cusp coils. If it is decided to go ahead and proceed with this effort, there are likely enough spare Cusp coils at the FRX-L facility that it should be possible to borrow six for use on FTX, and the time required to bring the Cusp circuit on line should be rather short.

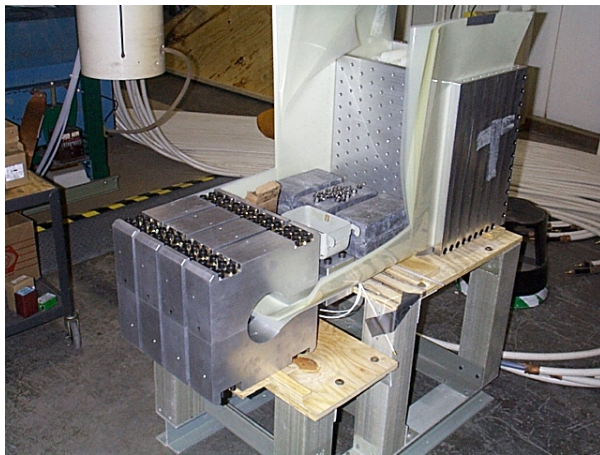
Regarding the Guide and Mirror fields and their bank circuits, FRX-L project manager Dr. Tom Intrator has recently enlisted the help of two other LANL personnel, Mr. William Reass and Mr. Robin Gribble, to develop designs for both the field coils needed to generate these fields and the pulsed power systems necessary to drive the coils. Like the design work being done on the new Theta coil segments, this effort is being carried out in preparation for moving forward with the FRX-L FRC translation setup. SAIC personnel intend to be involved and provide assistance wherever possible in this design effort, since we will be attempting to duplicate both the coils and the pulsed power drivers for the FTX experiment.



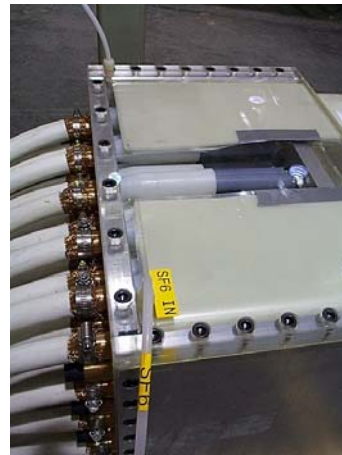
(a)



(b)



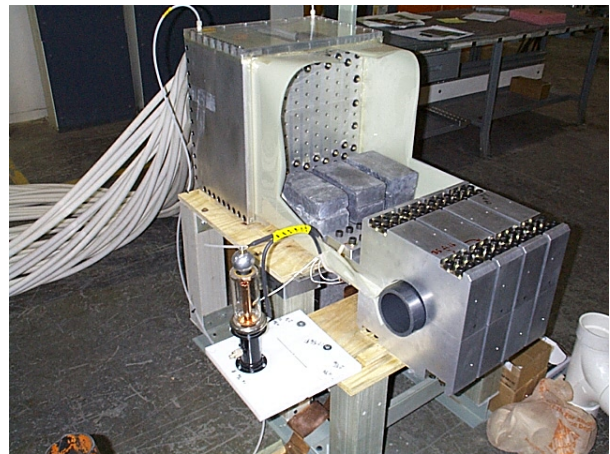
(c)



(d)



(e)



(f)

Figure 18. Photos of the ground (a) and hot (b) sides of the cable header during test fitting. (c) The cable header with the Theta coil attached is shown next as it nears completion. (d) Once the Main bank transmission line cables have been inserted into the header, the clear Lexan cover is placed on top. (e) A capacitive voltage divider is set up nearby to measure the voltage at the Theta coil. Two Rogowski coils will measure the current. (f) Photo of the finished Theta coil load and cable header setup.

1.7 VACUUM VESSEL AND FIELD COIL CONFIGURATION

As has been discussed in the previous two sub-sections, FRX-L personnel are currently in the process of calculating the field coil geometries and liner electrode configuration that will be required for the FRX-L FRC translation setup. Since the intent is to duplicate the FRX-L setup, for both the FTX experiments that will be conducted around the perimeter of the Shiva bank and certainly for the F-LINCX experiments conducted under the center of Shiva, SAIC personnel are attempting to work very closely with them in this design effort. Aside from the obvious need in our case to change the orientation of the entire setup from a horizontal topology to one that is vertical, special consideration must also be given to the arrangement of field coils around the liner region so that some radiography access to the liner is maintained and so that the externally applied Guide and Mirror fields do not adversely affect the magnetic insulation in the current feeds to the liner.

Figure 19 shows a drawing of the most recent arrangement of the field coils and liner electrode configuration that is being considered. SAIC personnel are using this as a guide to go ahead and begin design work on a support stand for not only the field coils but also the vacuum hardware such as the quartz tube and any stainless steel vacuum sections having diagnostic and vacuum pump ports. The stand will be required to have wheels because initially the entire vacuum and

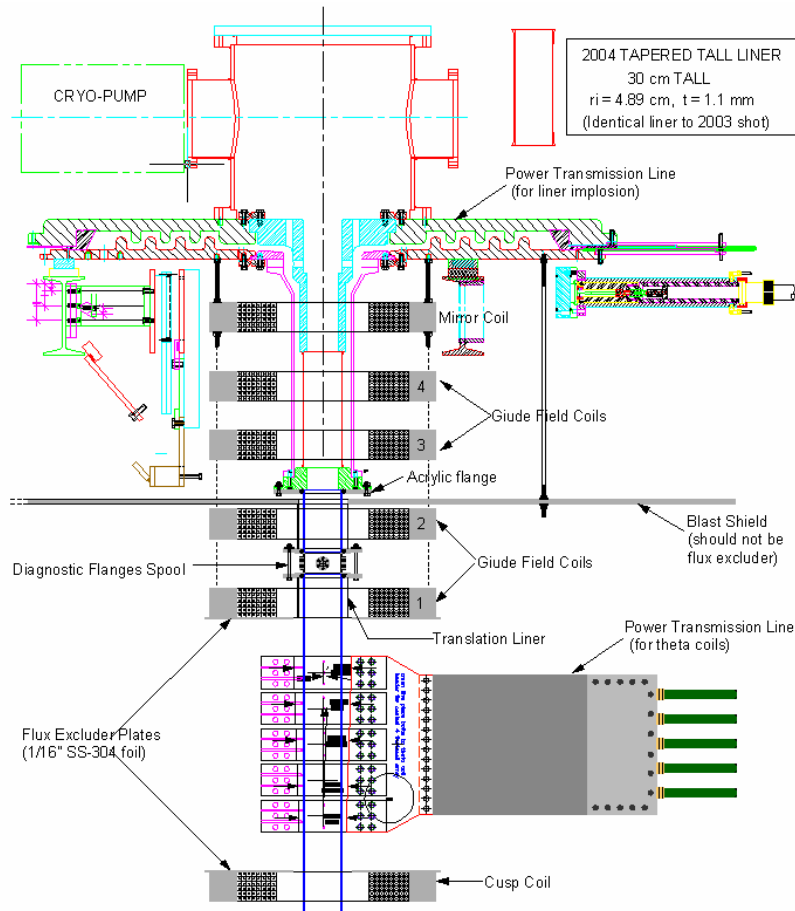


Figure 19. Most recent conceptual layout of the field coils, vacuum vessel, and solid liner to enable translation of the FRC from the Theta coil to the solid liner.

field coil assembly, complete with a “fake” liner and return conductor, will be set up just to the east of the Shiva bank for the initial formation and translation (FTX) tests, but at the appropriate time it must then be moved down the Shiva bank B-Arm to the Shiva center section when the compression-heating experiments (F-LINCX) are to be performed. With work on the Main, PI, and Bias banks either completed or well underway, the vacuum vessel is the last major item to be designed, fabricated, and assembled before beginning FRC plasma formation experiments.

1.8 TRIGGER GENERATORS, POWER SUPPLIES, HV CABLES, AND OTHER SUPPORT HARDWARE

Work on setting up the various sub-systems for the FTX experiment, as laid out in the floor plan shown in Fig. 1, began very early in this Task Order even before work on any of the banks began. Such sub-systems included the Main bank trigger unit and the Main bank power supply (Fig. 20a), both of which were previously used with the Formation bank and were known to be in

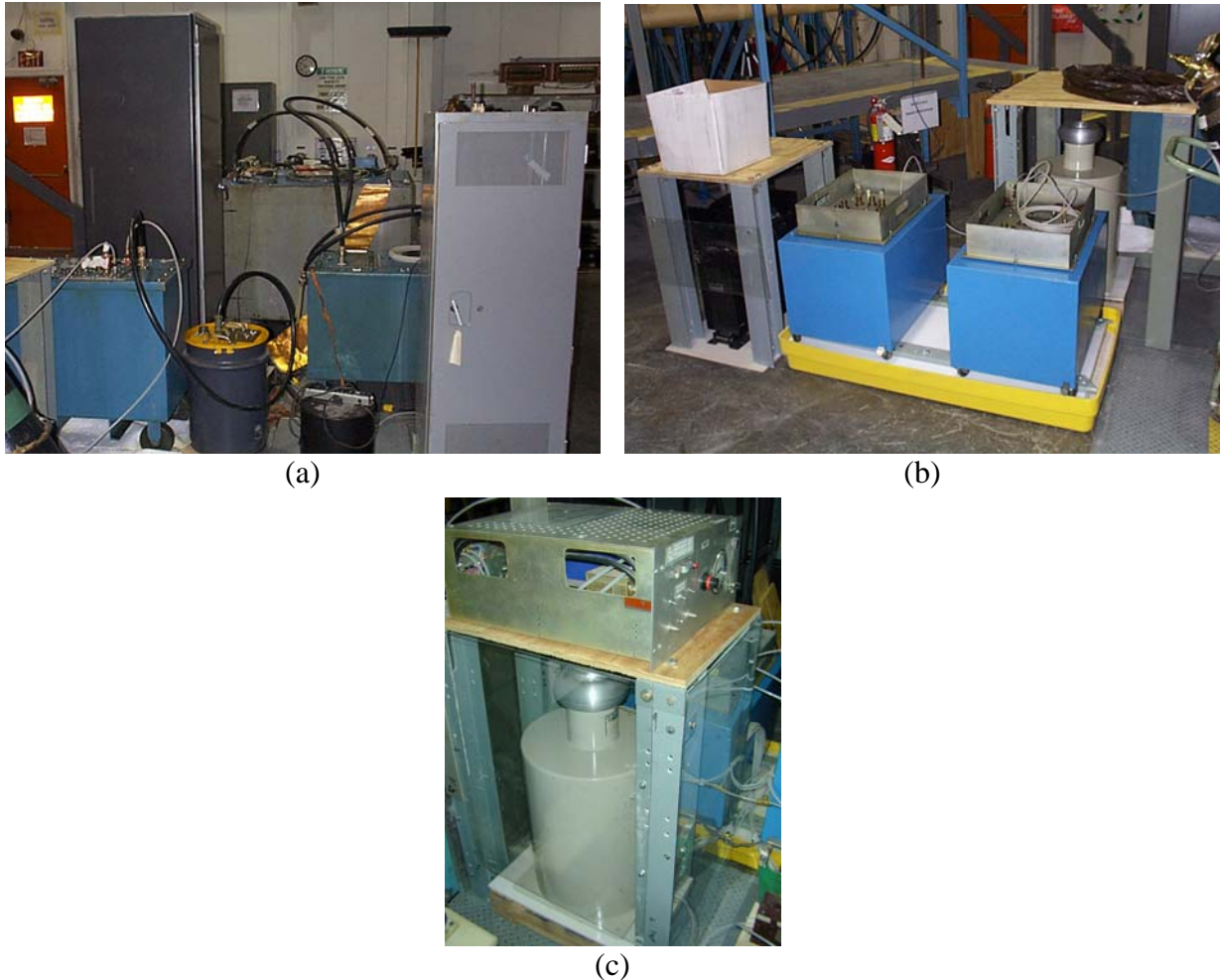


Figure 20. Photos of the ancillary components being set up between Shiva B- and C-Arms for the FTX (and F-LINCX) experiments: (a) the trigger (foreground) and power supply (background) units for the Main bank, and (b) the PI bank and Crowbar switch trigger units. (c) Lexan covers have been placed around the isolation transformers powering each trigger system to protect personnel from exposed terminals on the transformers.

good working order. Likewise, trigger systems for the PI bank and the Crowbar switch were also moved into place (Fig. 20b). Many of the components for these two systems, however, had been in storage, and it was not until recently that they were powered up and that high-voltage checks were performed to verify their status. The Crowbar trigger system has been found to be in good working order, however minor repairs are needed on the components set up for the PI trigger system; these repairs will be made in the near future. Remote trigger tests from the Shiva control room can be performed on the Main and Crowbar trigger systems as soon as fiber optic receivers are set up by each of the trigger systems and fiber optic cables are run to them.

Isolation transformers have been set up to power each of the rail gap trigger systems, since, as is indicated in Fig. 2 back in Sub-section 2.1, each of these trigger systems will be floated with their respective banks during a shot. The transformers have been placed underneath stands supporting other components of the trigger systems, and Lexan covers have been placed around the sides of the stands (Fig. 20c), since the terminals on the transformers are often exposed.

For all of the slow banks (i.e., Bias, Cusp, Guide, and Mirror) ignitrons will be used for switching. There were no trigger units for ignitrons found in our inventory, so the necessary components to construct five such units (including one spare) have been purchased. Assembly of these trigger units will get under way as the work on the Bias bank approaches completion.

As was just mentioned, the Formation bank power supply has been moved to the area between Shiva B- and C-Arms and will be used to charge the Main bank during experiments. To charge the Cusp, Guide, and Mirror banks, a 12 kV, 5 A Peter-Dahl power supply that has been provided to us by FRX-L personnel will be used. Charge switches on each of the banks will open when the respective charge voltage on each bank has been reached. Either a 50 kV, 8 kJ/s or a 40 kV, 2 kJ/s Maxwell CCDS power supply, both from our facility, will be used to charge the Bias bank, and a 50 kV, 80 mA Spellman power supply, also on loan from the FRX-L facility, will be used to charge the PI bank. These additional power supplies are in the process of being set up close to the Formation (Main) bank power supply.

To connect the power supplies to their respective banks and to then safely discharge these banks into dump resistors after a shot, FRX-L personnel have provided us with numerous Jennings switches. Figure 21a shows a photo of three of the Jennings switches recently set up to lift the Main bank charging connections, one each for the positive and negative charge lines to the bank and one for the charging return or ground. All bank charging connections will be set up in this manner to disconnect both the high voltage and charge returns (power supply grounds), as is indicated in Fig. 2. In addition, as Fig. 2 also points out, Ross relays are being used to lift the ground connections on the bank frames and on each of the triggering systems before each shot. The photo in Fig. 21b shows this setup for the PI bank. When all bank grounds are lifted, this will leave a single ground point at the Theta coil, and there should therefore be no ground loops created when the banks are fired. The Theta coil was chosen for the single-point ground location for the benefit of the diagnostics that will be placed around the coil.

Charging and dump resistors for the Main bank are already in place and are located on the trigger board support frame and within the Main bank power supply, respectively. For the remaining banks a charge and dump resistor setup similar to that in use on FRX-L and shown in Fig. 22 will be employed. As can be seen from the photo, the Jennings switches for these banks are mounted



(a)



(b)

Figure 21. (a) Three Jennings switches have been mounted on a wooden platform above the Main bank dump tank to lift the charging supply connections (positive and negative high voltage and ground) to the Main bank. (b) A Ross relay is being used on the PI bank (and on the other banks and trigger units) to lift the frame ground before a shot.



Figure 22. Photo of one of the charge and dump resistor stands, with the Jennings charge and dump switches mounted to it (upper right), on the FRX-L experiment. Bank voltage monitors are also mounted on these stands.

directly onto the resistor stands, and the resistors themselves are simply acrylic tubes filled with a copper sulfate solution to give a resistance of a few kilo-Ohms. Drawings for the hardware needed to build these resistor stands are being prepared now.

Charge and trigger cables for the banks and their switches are being laid out as the assembly of the respective bank or switch reaches completion. To handle the growing number of cables that are being run from the power supplies and trigger units over to the Main and PI banks, and also

to maintain separation between the sets cables belonging to the various banks and triggering systems, a fiberglass cable tray system having three separate raceways leading to the PI bank, the Main bank, and the Crowbar switch was erected (Fig. 23). The new cable tray arrangement is also supported independently of the Main bank, thereby allowing the Main bank to be disassembled or moved without disturbing the cable trays and the cables in them.

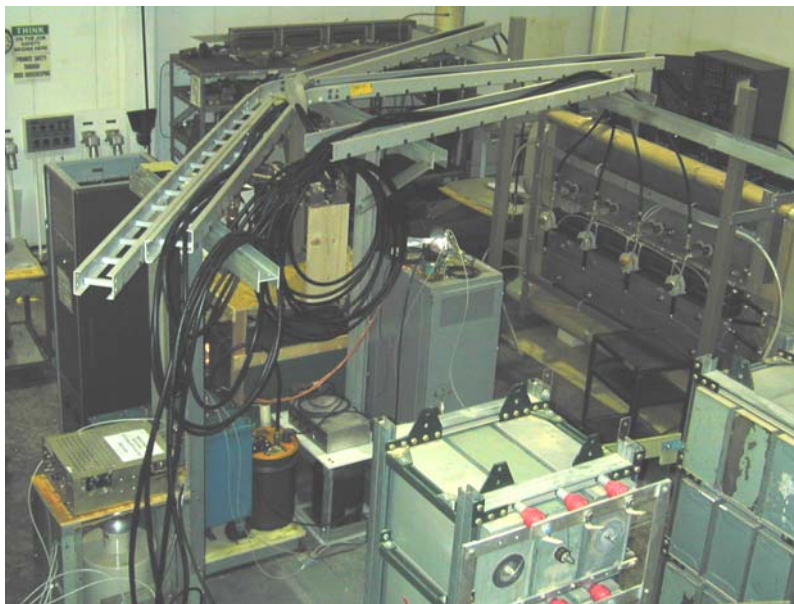


Figure 23 A view looking down on the triggering systems and Main bank power supply between the B and C arms of the Shiva bank. The arrangement of the new three-raceway cable tray setup can be clearly seen in the upper portion of the photo.

Gas control panels for all of the trigger units and for each set of rail-gap switches have been set up in close proximity to the test area in an equipment rack located underneath Shiva C-Arm. Gas lines were run to each of the trigger units first, as these units were set up. Later, as the Main bank, Crowbar switch, and PI bank were assembled, the gas lines were run to the rail-gap switches and to the peaking gaps on the Crowbar switch trigger board. An SF₆ line has also been run to the Main and PI bank cable headers and to the Theta coil cable header, so that their volumes can be filled with SF₆ for added voltage hold-off, as has already been discussed.

1.9 CONTROL SYSTEM

Mr. Phil Sanchez and Mr. Robert Aragonéz, who were formerly with subcontractor FabTek, Inc. but have recently become employees of LANL, have begun working with SAIC personnel on the design and assembly of the FTX control system. Mr. Sanchez and Mr. Aragonéz also worked with SAIC personnel under the previous MTF Task Order (Task Order 3) to set up and test the FRX-L control system, with Mr. Sanchez and his coworker overseeing the hardware portion of the control system and SAIC personnel writing and testing the LabVIEW®-based software.

Because the two experiments are so similar, the FTX control system can be nearly identical to the FRX-L control system, not only in architecture but also with respect to individual components and software, as well. One change that is likely to be made, however, is that a

Compact Field Point controller rather than a PXI-based controller is likely to be used for the core component of the system. This change is based upon Mr. Sanchez's recommendation, since the Compact Field Point components are less expensive and more ruggedized (i.e., less susceptible to being affected by EMI) than the PXI.

Based upon the number of input and output channels established for the FRX-L control system and the assignments of each of these channels, SAIC personnel have prepared a similar list of required channels for the FTX experiment. This list is presented in Appendix B for reference. Mr. Sanchez and Mr. Aragonex have taken this list and used it to identify and order an appropriate number of digital and analog modules needed for the Compact Field Point controller and the appropriate number and type of control transducers (air-actuated switches, fiber optic transmitters and receivers, etc.) needed to interface between the controller and the experimental setup. As soon as this hardware begins arriving, they will begin laying out the centralized portion of it in a Hoffman box and start wiring the components together. We anticipate being ready to start testing the control system by the end of the summer.

1.10 DIAGNOSTICS

As with the control system, because both FRX-L and FTX are so similar, the array of diagnostics, and especially the array of pulsed power diagnostics, is expected to be very similar between the two experiments. SAIC personnel have identified the various voltage and current monitors needed at each of the pulsed power banks in FTX, and these are listed in Table 1 in Appendix C. The diagnostics that will be needed up front to begin tests with the Main bank and Crowbar switch are indicated in red. These particular diagnostics, with the exception of the Faraday rotation setup at the Theta coil, have in fact already been fabricated, calibrated, and installed at their appropriate locations. Two diagnostic cable patch panels to connect to each of these diagnostics are currently being set up by the east wall of the high bay (18 channels) and among the trigger units (6 channels) between Shiva B- and C-Arms. The cable bundles from these patch panels are being run back to the Shiva center section where they will tie in with several patch panels there to send data all the way back to the Shiva screen room. Additional cables, or possibly analog optical fiber links, will likely be run when FRC plasma formation experiments begin, as numerous plasma and magnetic field diagnostics will also be fielded around the Theta coil at that time.

A fiber optic patch panel, similar to the data cable arrangement, is also in the process of being set up among the FTX trigger units to bring trigger signals from the Shiva screen room to the experiment. A listing of all anticipated triggers for the pulsed power banks, with those needed for the imminent tests with the Main bank and Crowbar switch indicated in red, is provided in Table 2 in Appendix C. Table 2 also notes some additional triggers that may possibly be needed for some of the plasma diagnostics. The fiber optic patch panel and the fiber bundle that is being run will be able to accommodate up to 24 triggers, which should be more than adequate for the experiment.

2.0 DEFORMABLE CONTACT SOLID LINER TESTS

The previous section of this report has focused on the status and progress of the experimental setup (FTX) that will form and translate an FRC plasma into a solid liner that will in turn be imploded by the Shiva Star High Energy Capacitor Bank. The dimensions of liners of interest to be used for imploding FRCs are approximately a 30 cm length and a 10 cm diameter. Liners of similar dimensions have been imploded in previous tests on Shiva Star, but such tests have allowed the use of solid electrodes that the liner would glide across as it imploded. To allow the FRC to enter the liner before implosion, however, the liner electrode facing the FRC formation region must be open, and to facilitate diagnostic access (for fast photography or spectroscopy) into the liner during the implosion the other end should have an opening, as well.

As was noted back in Section 1, there were some uncertainties regarding how uniformly a liner would implode once it moved radially inward over an opening in the electrode. Furthermore, since electrical contact obviously has to be maintained, the ends of the liner must stretch from the electrode into the opening as the bulk of the liner proceeds on its radially inward path. As a result, there was additional concern that regions at one or both ends of the liner might tear away from the electrodes during implosion and therefore not compress the FRC uniformly or to the extent that is required for fusion. An alternative liner implosion concept, a “ Θ -driven” concept (versus the “z-driven” concept that has traditionally been used), exists that would eliminate the potential for these problems, but it is not as efficient and would require a radically different configuration for the FRC formation and translation structure.

Because of the uncertainties associated with the implosion of a deformable-contact liner, it was deemed rather important to perform two liner-on-vacuum implosion experiments very early on in the work on this Task Order, before the configuration of the FRC formation and translation structure had become well defined. Both tests were very successful in that no tearing was observed and that the implosions appeared to be very uniform both axially and azimuthally. The next two sub-sections provide a summary of the results from these two tests.

2.1 DECEMBER 2003 TEST

The first deformable-contact liner implosion test was performed December 9, 2003. A drawing of the liner and electrode assembly for this test shot is shown in Fig. 24. Though the resolution of the drawing is not sufficient to clearly illustrate this, the liner has a greater thickness at its ends where it makes contact with the electrodes. This is the mechanism that allows the ends of the liner to deform and maintain electrical contact with the electrodes while the bulk of the liner continues to move radially inward. That is, as compression begins, the thicker portions move inward more slowly than the thinner regions, and this has the effect of causing the liner contacts at each end to stretch. Using 2D MHD simulations of the liner, Prof. Norm Roderick at the University of New Mexico was able to help select the necessary thickness and taper of the thickness along the length of the liner.

For this first implosion test, four radiography sources, driven by two 300-kV Marx banks, were set up for viewing the axial uniformity of the implosion and, hence, served as the key diagnostic for the test. Two of the sources were focused at the mid-section of the liner and two at the lower liner/electrode region, and each mid-section source was paired with the lower-electrode source below it so that a view covering approximately two thirds of the liner was obtained at each of the

times when the radiography Marx banks were triggered. Appropriate timing for triggering the radiography pulsers was determined with the aid of calculations made with a circuit solver finite thickness liner implosion code. This code was written and run by Dr. James Degnan of AFRL/DEHP.

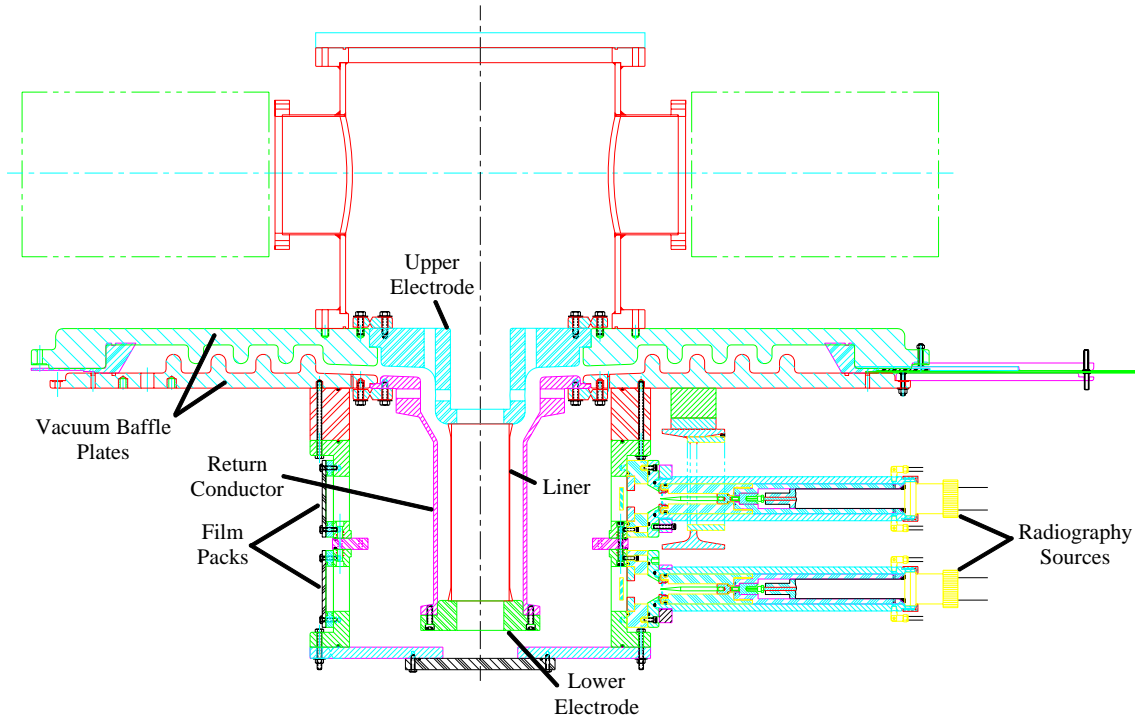


Figure 24. Cross-sectional diagram of the Shiva load region for the tall (30 cm), deformable-contact liner shot. The region both in and around the liner will be under vacuum, as will be the case when an FRC is to be compressed within the liner.

In addition to radiography, two micro-channel plate cameras were set up as an on-axis, fast photography diagnostic for observing the azimuthal uniformity of the implosion. Other diagnostics included six arm and four center-section Rogowski coils for current measurement on the Shiva bank, three V-dot probes for voltage measurement near the liner, the Faraday rotation diagnostic to provide a third liner current measurement, several B-dot probes to monitor liner current azimuthal uniformity, a PIN diode array with varying filters for X-ray photon measurement, and several scintillator photomultipliers, also for X-ray measurement.

Figure 25 shows two radiographic images of the liner before the shot. The image of the lower liner/electrode region in Fig. 25b provides a clearer view of the degree of taper in wall thickness. Figures 26 and 27 show radiographic images of the same regions in Fig. 25 taken during the shot at 20 μ s and 22 μ s after the start of current conduction, respectively. (It should be noted that the scales in Figs. 26 and 27 are not the same as in Fig. 25.) In Fig. 26 the images indicate that the middle of the liner compressed nearly uniformly, and there was no indication of any tearing or other abnormalities near the electrodes as the liner stretched inward. The images in Fig. 27 also show no signs of tearing near the electrodes, though a slight pinch seems to have formed at the base of the central region (Fig. 27a). The early stages of it can perhaps be seen in Fig. 26a.

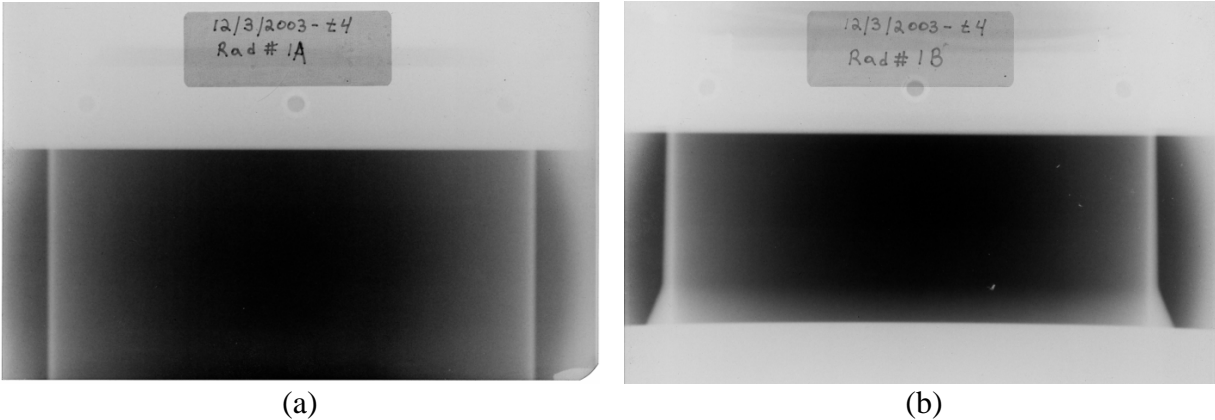


Figure 25. Radiographic images of the middle (a) and bottom (b) portions of the MTF deformable-contact liner (DCL). The taper near the electrode surface (from $\phi = 11$ cm to $\phi = 10.2$ cm) is very obvious for the first 1 cm, but another more gradual taper continues from there for another 5 cm (reducing to $\phi = 10.0$ cm).

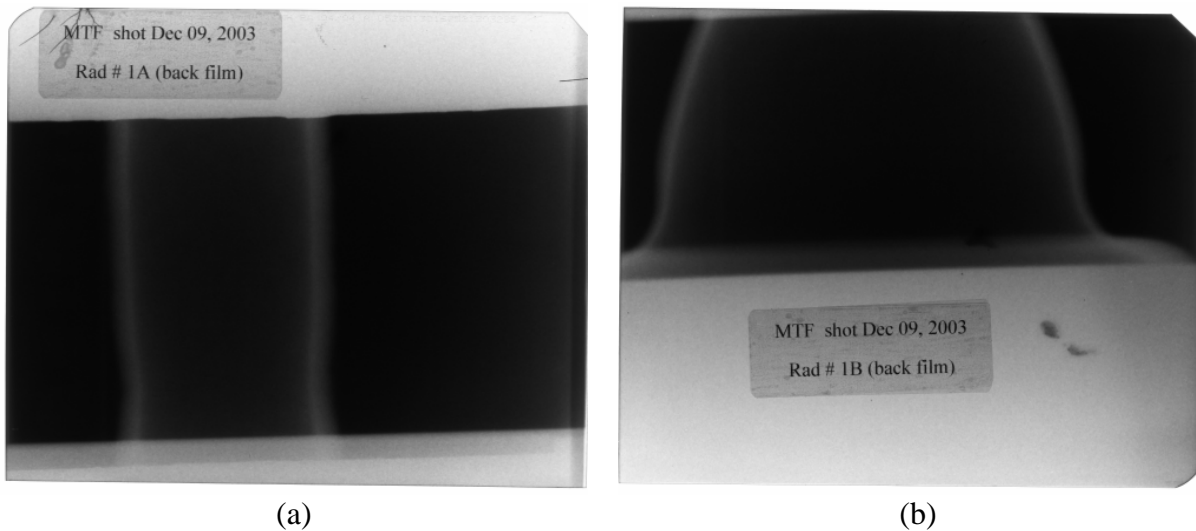
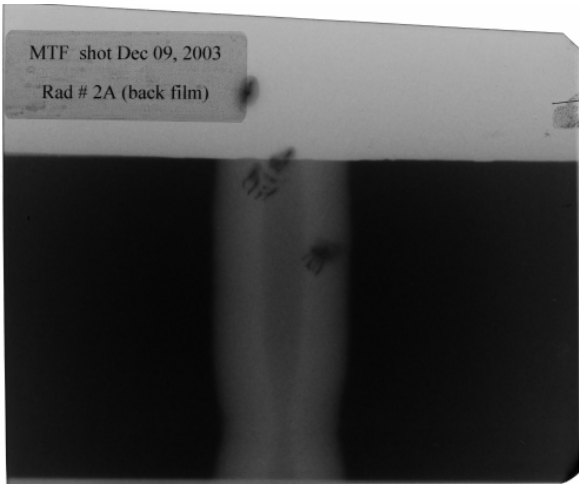


Figure 26. Radiographic images of the middle (a) and bottom (b) portions of the MTF DCL 20 μ s after current conduction began. The images show a nearly uniform radial compression in the central region of the liner with no indication of tearing near the electrodes.

Due to the field of view of the images recorded, it was not known if a similar pinch formed on the upper end of the central region. For the second implosion test shot, which will be discussed shortly, steps were taken to increase the field of view and obtain images of nearly the full axial length of the liner during the implosion. In any case, the pinch should likely not have an adverse effect on the FRC compression and may even aid in keeping it trapped in the liner.

Axial fast photography of the liner during the shot also revealed the implosion to be uniform azimuthally. A xenon flash lamp was placed on top of the Shiva bank and triggered just before Shiva itself was triggered. An aluminized Mylar mirror directed the light from the flash lamp down the axis of the liner, and a second mirror below the liner (this one made of glass) then directed the light to a gated MCP camera located 5 ~ 6 feet (1.5 ~ 1.8 m) away. Figure 28 shows



(a)



(b)

Figure 27. Radiographic images of the middle (a) and bottom (b) portions of the MTF DCL 22 μ s after current conduction began. The liner seems to be pinching slightly in the lower part of (a), but there is still no indication of tearing near the electrodes.

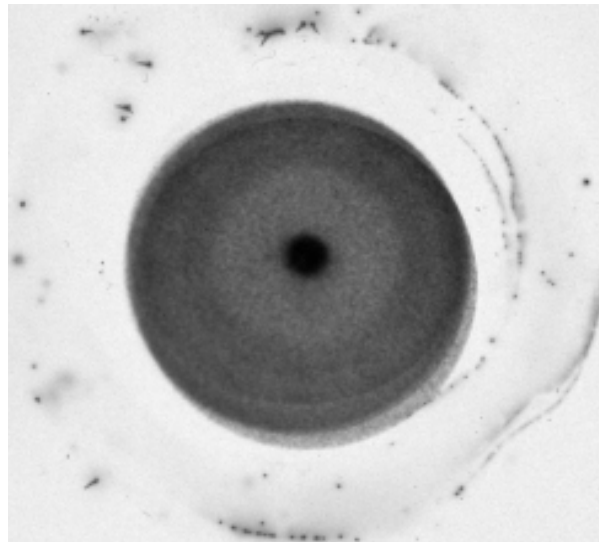


Figure 28. Photographic image (negative) obtained from the gated MCP camera. The MCP was triggered at 20.85 μ s and had a 300 ns exposure window.

an image recorded with the MCP camera $\sim 21 \mu$ s after current conduction started with a 300 ns window of exposure. The image is a negative, so the black spot in the center indicates the inner diameter of the liner, which is open and still transmitting light. As can be seen, the spot is very uniform.

As might be expected from the images above, signals from three B-dot probes spaced 120° apart in the return conductor around the liner also showed that there were no non-uniformities in the current delivered to the liner. These signals, along with the current waveforms measured with the Shiva arm and load Rogowski coils are presented in the plot in Fig. 29. The Rogowski current waveforms have been rescaled by a factor of 1.1 before being plotted in this graph, as

previous Shiva shots on which the Faraday rotation diagnostic was fielded have shown that the sum of the arm currents and the CW/CCW Load currents are low in amplitude by this amount. (The Faraday diagnostic has been chosen to be the “standard” because it has been found to be the most accurate diagnostic for determining the actual amplitude of the current.) The B-dot probe waveforms were also rescaled (arbitrarily) by 1/1.13 to 1/1.16 (i.e., 0.885 to 0.865) to make them overlay with the Rogowski signals. This minor variation in amplitude in the B-dot probe signals is not unexpected, since placement of the probes in the experimental setup at the exact orientation and depth to which they were placed when calibrated in the calibration stand is somewhat difficult.

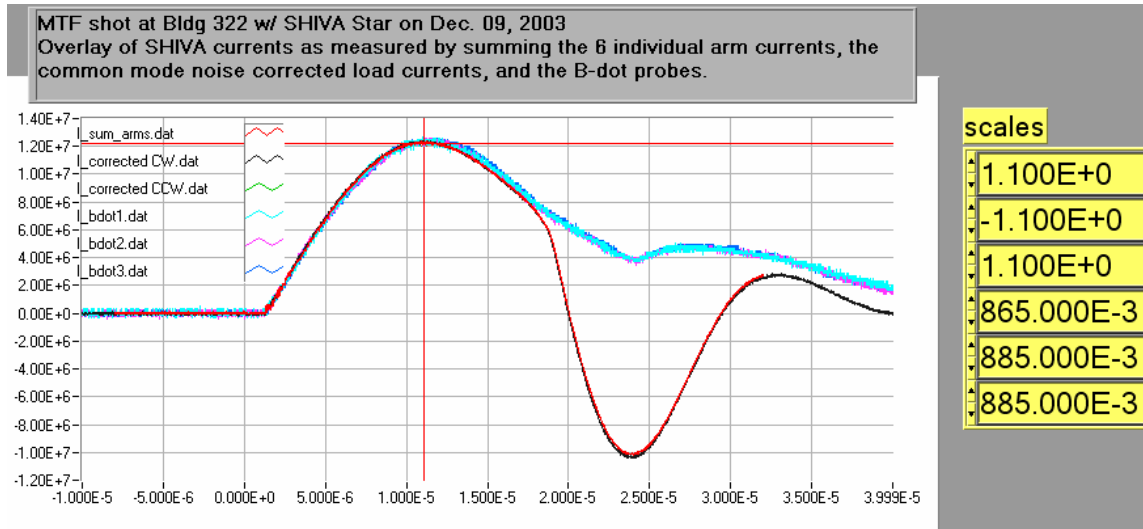


Figure 29. Current waveforms measured by the Shiva arm Rogowski coils, the clockwise (CW) Rogowski coil, the counter-clockwise (CCW) Rogowski coil, and each of the three B-dot probes inserted through the liner return conductor. The waveforms have been scaled by the factors shown to the right of the graph.

In any case, after adjusting the scaling the Rogowski coils all indicate that a peak current of ~12.2 MA was obtained, and all six waveforms plotted in the graph follow each other very closely up until $t = 17 \sim 18 \mu\text{s}$. At this point, the Rogowski coils, which are further away from the liner, indicate a more rapid drop and reversal in current, while the B-dot probes indicate continued current flow of the same polarity through the liner. Note that current flow is actually observed to start at $t = 1.3 \mu\text{s}$, so that the corresponding times for the photos in Figs. 26 – 28 are then 21.3 μs , 23.3 μs , and 22.15 μs , respectively.

2.2 JANUARY 2005 TEST

The second deformable-contact liner implosion test was performed January 5, 2005. A key change in the setup compared to the previous shot was the provision enabling radiographic images to be taken that spanned nearly the entire length of the liner during the shot. To accommodate the increased field of view, the radiography sources were moved back from the liner, and the aluminum hexagonal vacuum chamber surrounding the liner and return conductor was replaced with a 1” thick acrylic tube with an aluminum end plate. There were essentially no

changes made to the liner, its upper and lower electrodes, or the return conductor, however. Figure 30 shows a cross-sectional diagram of this new hardware arrangement.

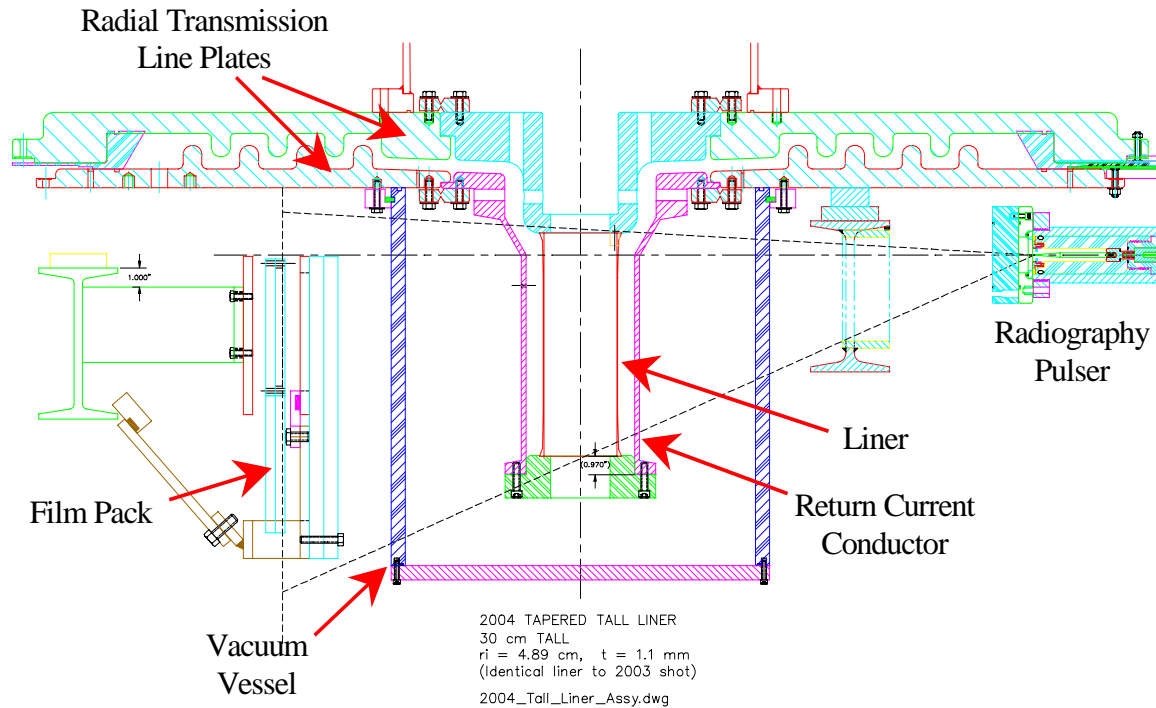


Figure 30. AutoCAD drawing of the hardware configuration used in the second deformable contact liner shot. The black dashed lines indicate the center axis of the radiography pulser, the field of view of the pulser (dictated by the port in the steel I-beam in front of it), and the plane of the radiographic film pack.

The load current waveforms obtained during the shot from the Faraday rotation diagnostic and the clockwise (CW) and counter-clockwise (CCW) Rogowski coils are shown in Fig. 31. The sum of the currents measured by the six Shiva arm Rogowski coils is also shown in the plot. As is the case for the data presented in Fig. 29, each of the three Rogowski waveforms has been multiplied by a correction factor of 1.1 to match their amplitudes with that of the waveform obtained from the Faraday diagnostic. As can be seen, there is excellent agreement among the current waveforms from all four diagnostics.

Current waveforms measured with three B-dot probes, placed 120° apart around the return conductor (Fig. 30), are shown in Fig. 32. The amplitudes of the waveforms are within 8% of those measured by the other current diagnostics (Fig. 31), but more importantly there is again very good agreement between the shapes of each of the probe signals, which indicates uniform current delivery to the liner. Only at $t = \sim 22 \mu\text{s}$, at which point the liner has perhaps reached the center axis and begun to expand again, do the current waveforms begin to differ from one another.

Radiographic images of the liner were taken at similar times as the images recorded during the first test shot (Figs. 25 – 27) and are shown below in Figs. 33 – 35. Figure 33 shows a static

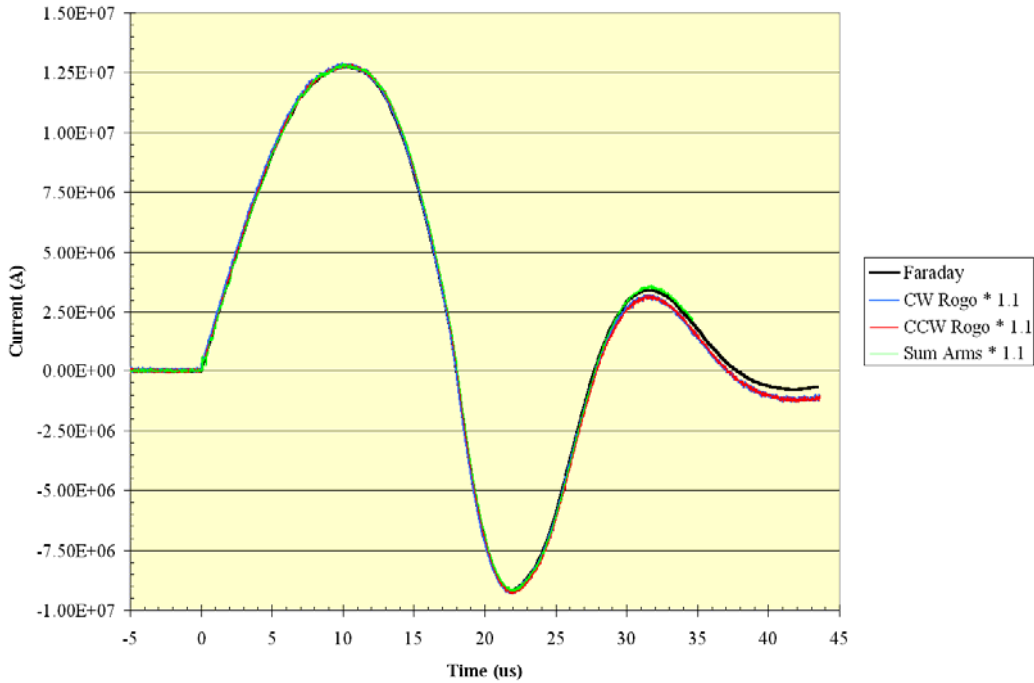


Figure 31. Current waveforms obtained with the Faraday rotation diagnostic, the clockwise (CW) and counter-clockwise (CCW) load Rogowski coils, and the six Shiva arm Rogowski coils. Each Rogowski coil signal has been multiplied by a correction factor of 1.1.

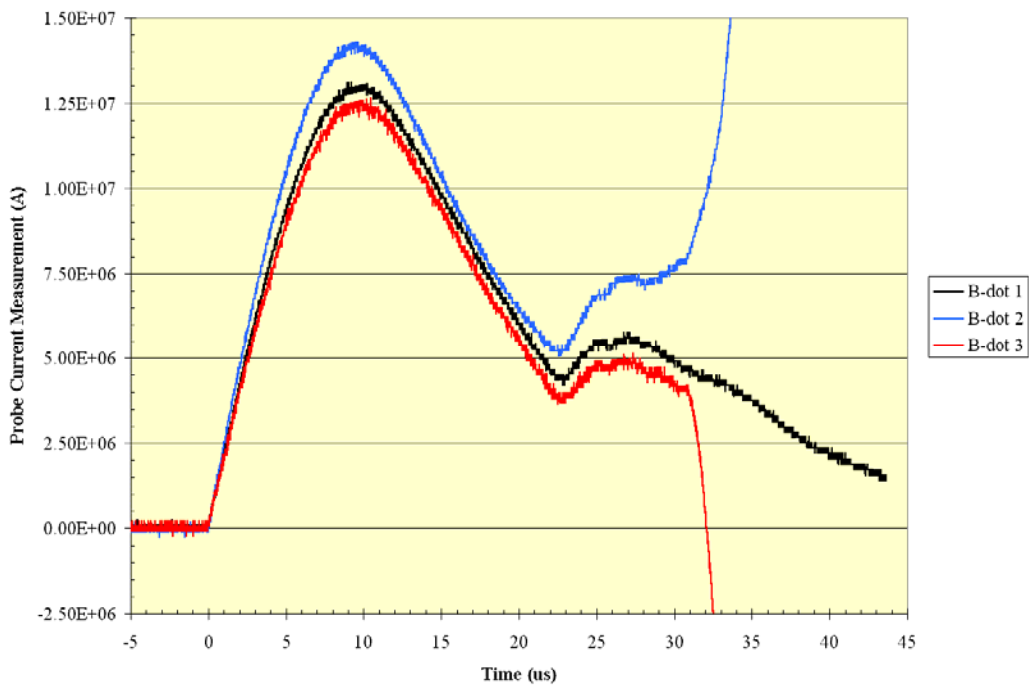


Figure 32. Current waveforms obtained from the three B-dot probes inserted into the return conductor. The probes were spaced 120° apart azimuthally.



Figure 33. Static radiographic image of the deformable contact liner taken before the shot.



Figure 34. Radiographic image of the liner taken 20.96 μ s after current delivery began.



Figure 35. Radiographic images of the liner taken 21.88 μ s after current delivery began.

view of the liner taken before the shot, Fig. 34 shows an image of the liner during the shot at $t = 20.96 \mu\text{s}$ after current has started flowing, and Fig. 35 shows the liner at $t = 21.88 \mu\text{s}$. The actual radiographic films that were recorded are one piece, but due to the size limitation of our scanner only half of the film could be scanned at one time. A piece of tape was placed on each film (projecting from the right side of each image) as a marker to indicate where to overlap the top and bottom images.

The radiographs show a very uniform radial implosion of the liner with even a slight pinch developing at each end of the uniform region (c.f., the pinch observed in Figs. 26a and 27a). As mentioned above, such a pinch may provide further aid in confining the FRC within the liner as it is being compressed. After carefully analyzing and comparing the mean liner diameters observed in the radiographs in Figs. 33 and 34, it can be seen that the liner is compressed by a factor of approximately 4.6 by $20.96 \mu\text{s}$. From the radiograph in Fig. 35 a factor of 7.2 in compression is observed by $21.88 \mu\text{s}$, and now both ends of the liner appear to be totally closed off while a narrow opening remains in the middle. The increased radiographic field of view in this second experiment has verified that there are no instabilities developing at late times during the implosion, and data from both liner shots have revealed an extremely uniform radial compression of the liner. These data confirm that a “z-driven” liner can in fact be used for FRC compression.

3.0 SUPPORT OF EXPERIMENTAL EFFORT (FRX-L) AT LOS ALAMOS

Picking up where Task Order 3 left off, under Task Order 36 SAIC personnel and subcontractor FabTek, Inc. have continued to provide support on a regular basis to personnel at the FRX-L facility. Traditionally our support efforts have been focused primarily on the FRX-L Main bank Crowbar switch, including such tasks as providing assistance with troubleshooting (of the triggering system), maintenance (rail-gap switch cleaning), and repairs. Soon after the start of work on Task Order 36, however, the Crowbar switch work was expanded to include a complete redesign of the configuration of the switch. The redesign effort was aimed at reducing the amount of modulation induced by the Crowbar switch on the Theta coil current waveform to the minimal amount possible. SAIC's efforts in this area also included preparing the detailed hardware drawings necessary to have the parts fabricated, and then following through with the fabrication and installation of the new switch on the FRX-L Main bank.

More recently, SAIC personnel have been able to provide assistance in a number of other areas related to the daily operation of the experiment, from troubleshooting other systems (e.g., identifying a bad capacitor in one of the banks and helping to replace it) to helping with the set-up of various diagnostics (e.g., an array of fiber optic light monitors) to even operating the FRX-L system, as needed. Related to design and upgrade efforts, SAIC was able to help with the implementation of a passive mirror scheme on the ends of the Theta coil earlier this year. Within the past couple of months, SAIC personnel have performed analyses on two proposed capacitor bank designs that will possibly be set up to drive various field coils as experiments in FRC translation begin.

In the subsection below, SAIC's work related to the FRX-L Crowbar switch will be discussed in much greater detail. In following subsections, additional information regarding the other design efforts that SAIC personnel have been supporting is provided.

3.1 LOWER-INDUCTANCE CROWBAR SWITCH FOR THE FRX-L MAIN BANK

3.1.1 First Crowbar Switch – Description of Triggering Problems and Excessive Modulation

Since its installation on FRX-L as part of the work performed for Task Order 3, the Main bank Crowbar switch has had considerable difficulties with triggering. Specifically, this problem has manifested itself as the inability to initiate current conduction in all four Crowbar rail-gap switches at the desired time except within a narrow time window around the zero crossing of the voltage across the switch. Even within this time window, the jitter displayed by the individual rail gaps was fairly substantial (100's ns). Furthermore, while the time window did lie in a region where one would typically desire to trigger a Crowbar switch, at the Theta coil current maximum, the time window also coincided with a regime in which the switch operated more inductively, as was evidenced during characterization tests performed at AFRL. Consequently, the Crowbar switch induced a considerable amount of amplitude modulation on the Theta coil current waveform during each shot. Before pursuing an alternative lower-inductance Crowbar switch design, a number of attempts were made to identify and remedy the triggering problems so that the existing switch could be operated in a lower-inductance regime.

The graph in Fig. 36 better illustrates the triggering problems encountered. Waveforms from the voltage monitor across the Crowbar switch, taken from several shots with varying delays between the Main bank and Crowbar switch triggers, are overlaid. The Theta coil current peak occurs approximately $2.6 \mu\text{s}$ following the start of the Main bank current, where the voltage waveform crosses the axis. In each case, there is an abrupt rise in voltage when the Main bank is triggered; then as voltage drops there appears a spike in each waveform corresponding to the time at which the Crowbar is triggered. For the $2.6 \mu\text{s}$ case, there is some small voltage oscillation remaining across the Crowbar switch after it is triggered. This voltage is the drop due to the inductance (and finite resistance) in the switch. For the $2.2 \mu\text{s}$ case, the trigger is clearly seen to have occurred earlier, but the voltage in the negative cycle swings much larger until at $\sim 12.8 \mu\text{s}$ there is a sudden drop (though following the drop the voltage still remains larger than for the $2.6 \mu\text{s}$ case). This drop indicates when the Crowbar switch actually starts conducting, $\sim 3.1 \mu\text{s}$ after the trigger pulse. The situation becomes worse for the $1.8 \mu\text{s}$ case, and still worse when the PI bank is not operated. Open shutter photos have confirmed that switch operation was poorer as the delay time was decreased. With a delay of $2.6 \mu\text{s}$, all 4 rail-gap switches were seen to fire; with a delay of $2.2 \mu\text{s}$, only three rail gaps fired and the fourth remained dark; and during the $1.8 \mu\text{s}$ shots only one or two of the rail gaps fired.

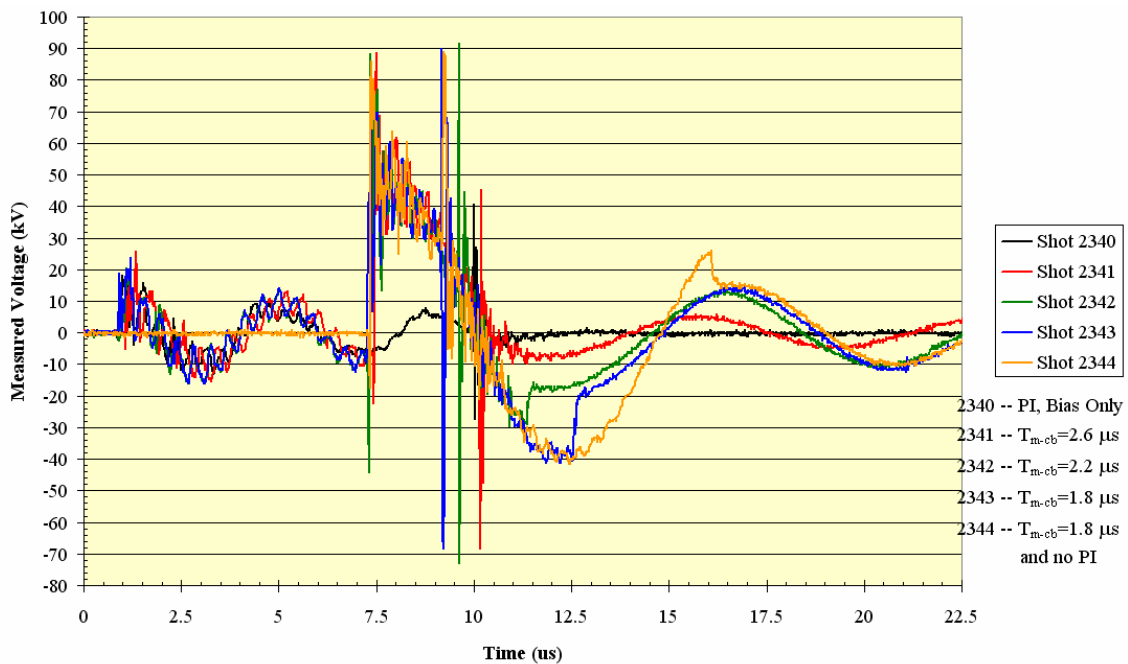


Figure 36. Plot of voltage across the Crowbar switch vs. time. Waveforms from shots with varying Main bank-to-Crowbar triggering delays (and one without the Main bank – #2340) are overlaid to show how the Crowbar triggering becomes worse as delay time is decreased.

The extent of the modulation on not only the Theta coil current but also on the magnetic field forming and compressing the FRCs was evident from the flux loop waveforms, several of which are shown in Fig. 37. As the trigger delay is decreased, the modulation was found to increase, and because switch closure tended to occur later and later after the current maximum, the mean current and flux was also reduced.

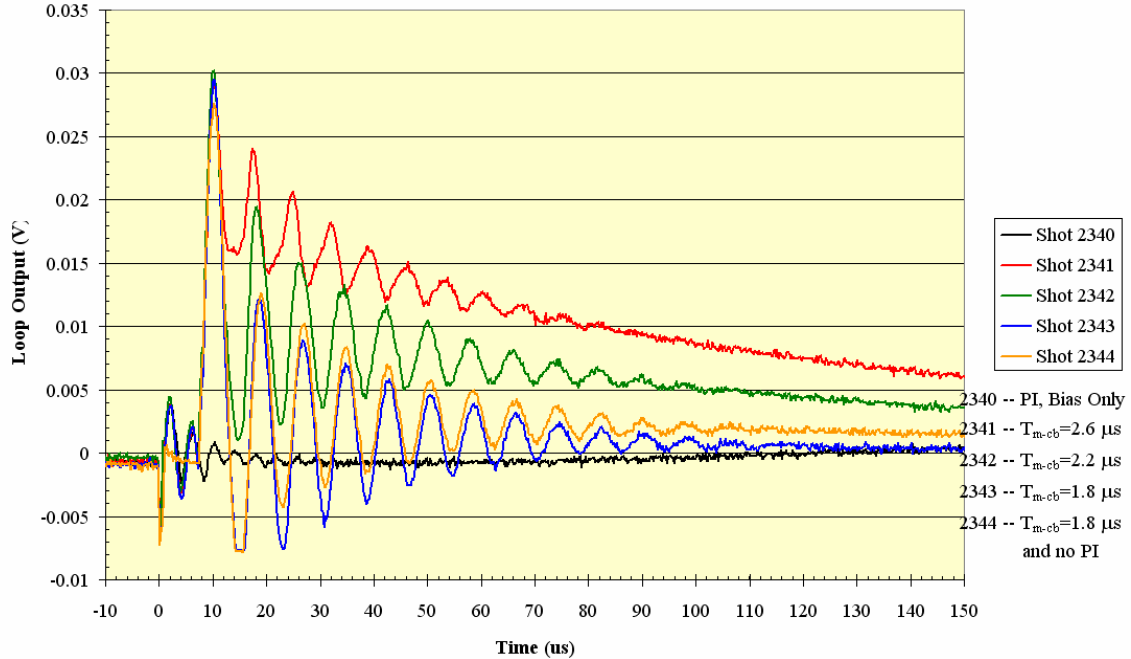


Figure 37. Output signals from one of the flux loops around the vacuum vessel at the theta coil for the same shots as in Fig. 36. As delay decreases – and switch closure occurs later in time – the modulation in the flux increases and the average value drops.

It should be noted that during the characterization tests of the Crowbar switch conducted at AFRL, such triggering problems were not observed. Rather, the switch seemed to trigger quite readily at whatever delay time was dialed into the delay generator, and opposite to what has been observed at FRX-L the load current modulation increased as the delay approached the time of the Theta coil current maximum/voltage minimum (Fig. 38). (It is this behavior that led to the hypothesis that with less voltage across the Crowbar rail gaps when they are triggered, there is poorer multi-channeling, which in turn leads to higher switch inductance and more modulation in the current waveform following the Crowbar trigger.) Furthermore, open-shutter photos always indicated that all four Crowbar rail-gap switches fired.

Therefore, in an effort to better understand the source of the Crowbar switch triggering problem on FRX-L several trigger diagnostics were set up and monitored. The diagnostics consisted primarily of Rogowski coils placed around both the Main bank and Crowbar switch trigger cables at the trigger boards to monitor the amplitude and rate of rise of the trigger pulses. Other diagnostics such as fiber optic monitors to sense when the peaking gaps on the Crowbar trigger board fired and a voltage monitor to measure the change in potential between the trigger cable ground braid and the Main bank ground were also fielded and monitored over several shots. Data from three of the Crowbar trigger monitors and one of the Main bank trigger monitors is shown in Fig. 39. Part of the noisy appearance of the signals is likely due to reflections of the trigger pulse at the rail gap trigger electrode, as it first encounters an open circuit followed by a rapidly falling impedance. The waveforms shown here are unintegrated; that is, they show the dI/dt of the trigger pulse. It is immediately obvious that the dI/dt for the Main bank trigger pulse is significantly larger than that for each of the Crowbar trigger pulses. The shape also is somewhat different. Integrating the signals to obtain the current in each trigger pulse also shows a difference in amplitude between the Main bank and Crowbar switches, though it is not quite as

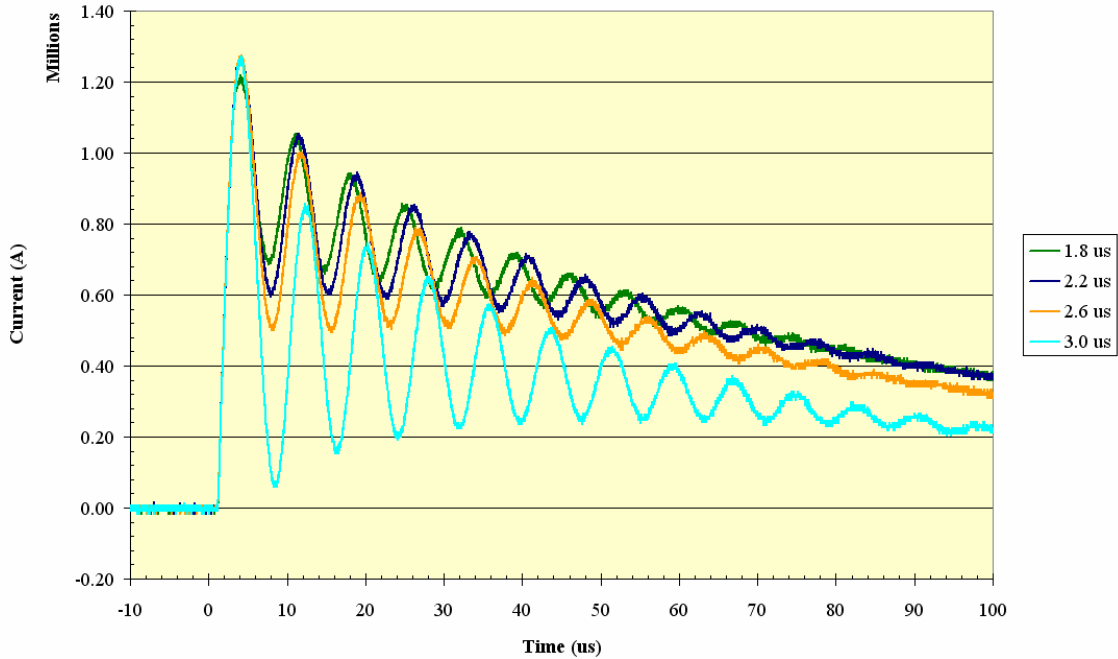


Figure 38. Several load current waveforms recorded during AFRL Crowbar test shots. The quarter cycle time for the current was slightly longer than for FRX-L, being $\sim 2.9 \mu\text{s}$.

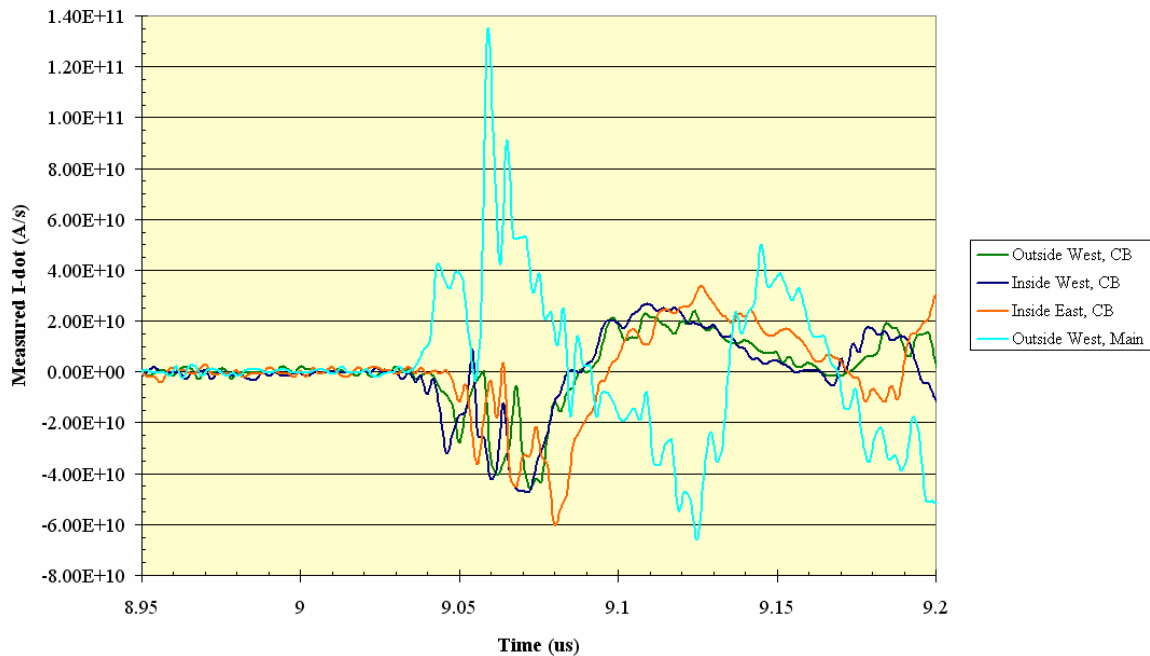


Figure 39. Graph showing typical waveforms (unintegrated) obtained from Rogowski coils placed around trigger cables going to the west side and the two inner Crowbar rail-gap switches and to the west side Main bank rail-gap switch. The Main bank monitor signal was delayed by $1.845 \mu\text{s}$ to allow it to be displayed with the other signals.

pronounced (Fig. 40). For the shot illustrated in these graphs, the Main bank was charged and fired, though the trigger dI/dt and current waveforms appeared nearly identical in trigger-only tests.

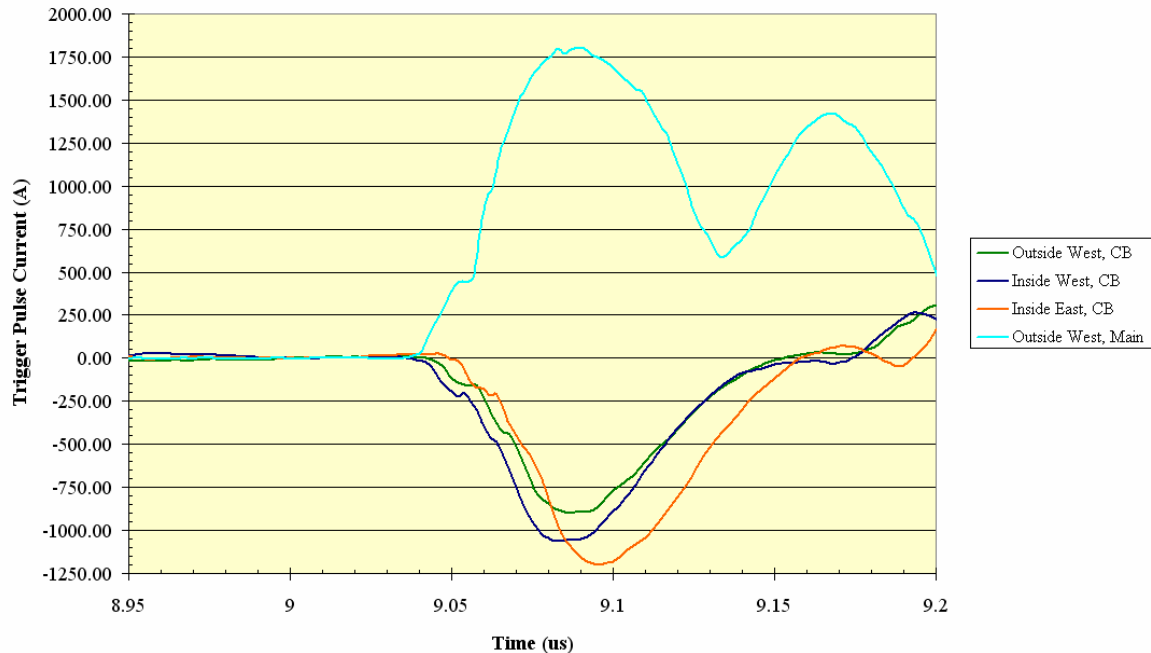


Figure 40. A graph of the same waveforms shown in Fig. 39 after they have been integrated. The Main bank monitor signal was again delayed (by 1.845 μs) to allow it to be displayed with the other signals.

At first glance the data in these two graphs appear to point to the Crowbar trigger system as being the source of the problem because of the considerably lower amplitude of the Crowbar trigger signals when compared to the Main bank trigger signals. However, all of the components beyond the master trigger generator to the Crowbar rail gaps (trigger cables, trigger board components, etc.) were also a part of the initial Crowbar test setup at AFRL, and thorough checks of these components showed nothing abnormal with them. Inside the Crowbar master trigger generator, which of course generates and launches the trigger pulses down the trigger cables, there is only a power supply and a spark gap switch to short out that end of the trigger cables. A quick measurement of the DC charge voltages applied by both the Main bank and Crowbar switch master trigger generators revealed that they were within 1 kV of each other. It is possible that the peaking switches on the Crowbar trigger board are responsible for the lower dI/dt in the Crowbar triggers, as the Main bank trigger setup does not include any such switches. Their main purpose is to increase the dV/dt of the trigger pulse delivered to the Crowbar rail gaps, but the addition of another series resistive and inductive element may work to reduce the dI/dt . If this is the case, though, it must also have been true for the AFRL test setup, as well, since again the same peaking switches are being used on FRX-L. Thus, while these data provide some additional and interesting information, they still have not provided a clear indication of where the source of the triggering problems really lies.

3.1.2 Steps Taken to Alter Circuit Properties External to the Crowbar Switch

In addition to studying the Crowbar triggering problems and examining how the Crowbar switch might be triggered at earlier times where it could operate less inductively, FRX-L and SAIC personnel also explored a means of altering inductances elsewhere in the Main bank circuit with the intent of decreasing the influence of the Crowbar switch inductance. Specifically, this

approach involved moving the flux excluder plates further away from the ends of the Theta coil (from 2 cm to 4 cm on each side). By increasing the spacing between the two, the effective inductance of the theta coil would increase, and thus the Crowbar inductance would become a lower percentage of the total circuit inductance. SAIC's Dr. Jerry Parker performed several computational analyses of the Theta coil and excluder plate geometry and determined that the net inductance increase for the Theta coil would be from ~24 nH to ~31 nH with this change.

Subsequent shots did indeed show some improvement in the way of a reduction in modulation on the crowbarred Theta coil current waveform, however the reduction was still not sufficient for acceptable FRC plasma formation. The modulation seemed at best to be ~50 %. With minor modifications to the Crowbar switch bus hardware, such as those that had been proposed in the Task Order 3 final report, further improvement in the performance of the switch could be expected, however FRX-L's Dr. Tom Intrator estimated that an acceptable upper limit for the amplitude of the modulation was only 25 ~ 30%. Otherwise, the FRC would likely expand axially beyond either end of the Theta coil at the first current minimum and the resulting particle loss would be quite high, which in turn would adversely affect the FRC lifetime. Since our estimates for the reduction in inductance that would be obtained with the proposed modifications to the present switch did not appear to meet these requirements, SAIC personnel began studying alternative Crowbar switch designs that could keep the level of the modulation below this limit.

3.1.3 Redesign of the Crowbar Switch to Dramatically Reduce Current Modulation

Several different Crowbar switch configurations were considered, but eventually it became apparent that the one illustrated in Fig. 41 would be the best choice. Because the current path for

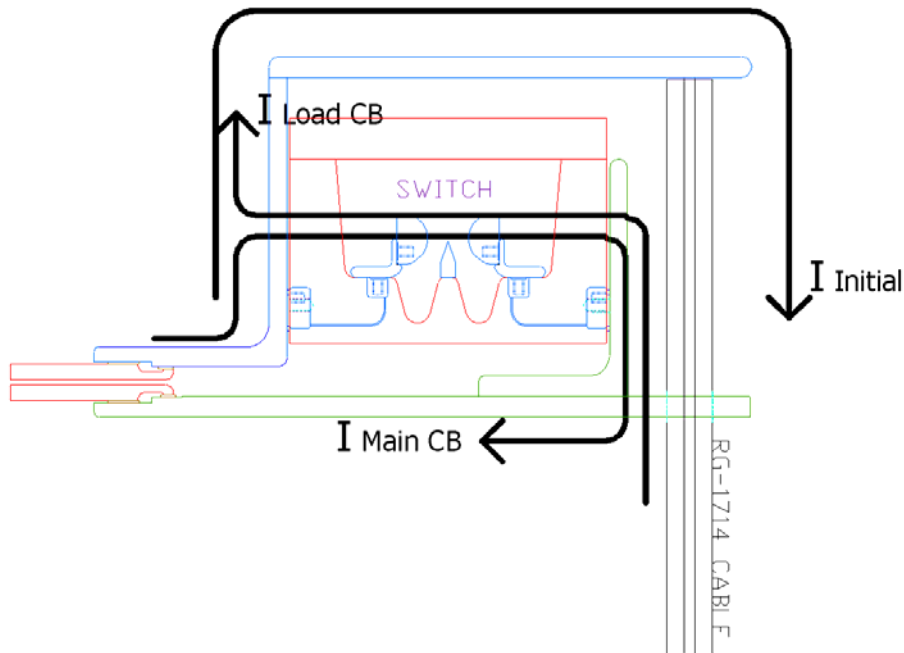


Figure 41. Conceptual drawing of a Crowbar switch configuration allowing the center conductors of the RG 17/14 cables to be connected to bus plates running over the tops of the Crowbar rail gaps. Arrows indicate the current paths during the initial discharge and following the triggering of the Crowbar switch.

the RG 17/14 cores (dielectrics and center conductors) runs over the tops of the rail-gap switches instead of below, as was the case with the first Crowbar switch configuration, the two loops formed by the crowbarred Main bank and Theta coil circuits do not enclose any volume that is common between the two. With no shared volume (i.e., no coupling), the modulation of the crowbarred Theta coil current waveform is significantly reduced. Circuit simulations, using inductances calculated for the new geometry, predicted a modulation of 28 ~ 29%, within the acceptable range determined by Dr. Intrator. To achieve a further reduction in inductance adding a fifth rail gap switch in parallel with the other four was considered, but it was later decided to limit the design to four rail gaps, since the FRX-L Crowbar trigger system was already set up for a four-rail-gap Crowbar switch.

Following the preparation of a Solid Works® model of the switch showing many of the hardware details (Fig. 42), a formal review for this new design was held at the FRX-L facility on March 3, 2004. The purpose of the review was to make certain that nothing was being overlooked in the design and to allow FRX-L personnel an opportunity to insert any last-minute additions into the design that experience with the first crowbar switch had shown would be useful or important to have. The additional features that were proposed were minor and are located where the red circles are shown in Fig. 43.

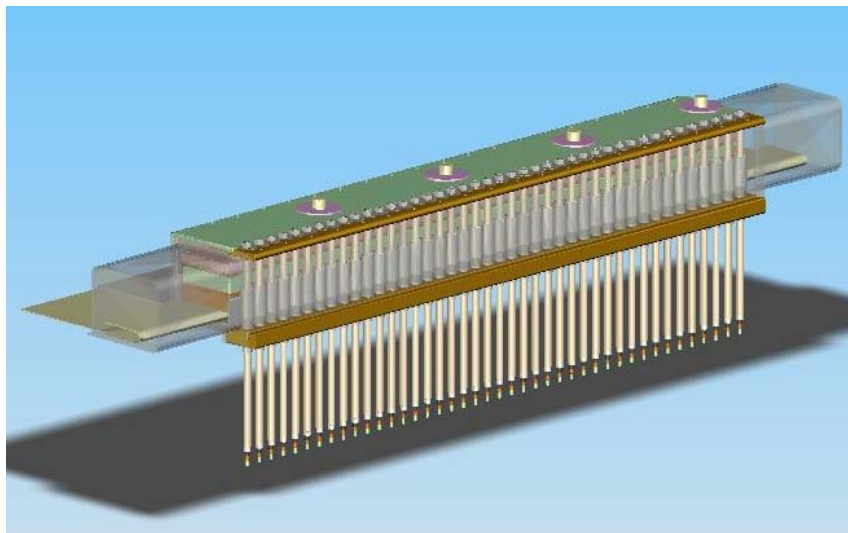


Figure 42. Solid Works® rendering of the new crowbar switch design.

The first addition to the design that was suggested (I) involved inserting an array of seventy-two fiber optic cables in the conductor going over the rail-gap switches (eighteen per switch). Since this conductor passes over the switch, it effectively blocks all view of the switch and prevents any open-shutter photos from being taken during shots (which have been used to verify that the rail gaps conducted current and that multi-channeling was good). An array of optical fibers could perform this same monitoring function in place of the open shutter photos, however, since several fibers, spaced uniformly along the length of each rail-gap switch, could transmit light from the rail gaps to either a film pack or an array of fiber optic receivers, thereby providing the same information as an open shutter photo. Either the recorded image or the signals from the fibers would then show whether each rail gap had fired and, if so, whether the light (current channels) was uniform along the length of the gap or concentrated in just a few locations.

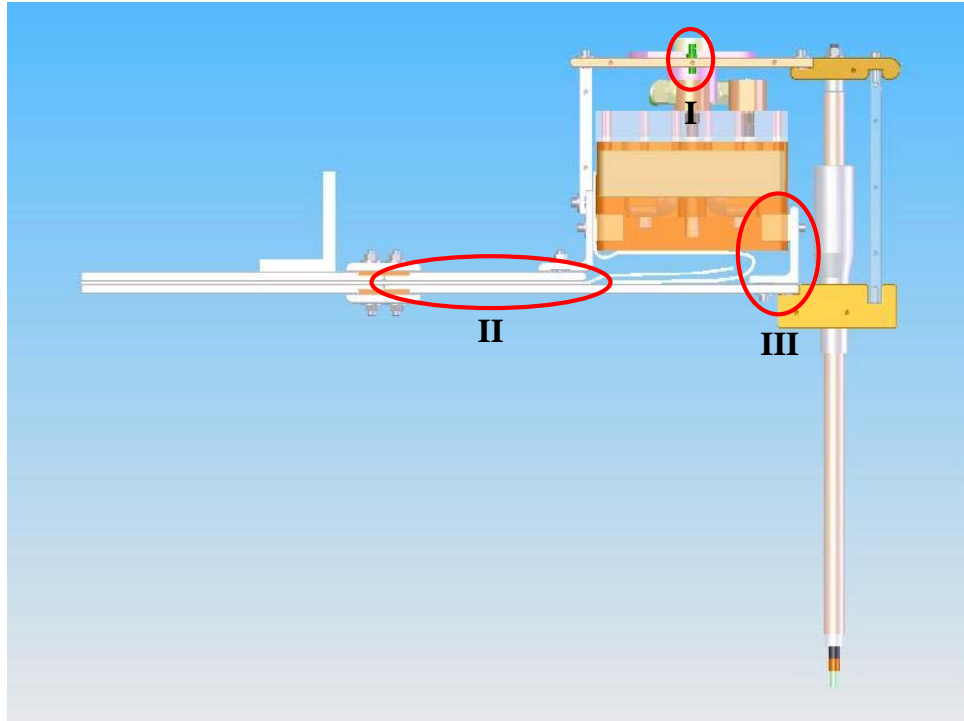


Figure 43. End-on view of the Crowbar switch model shown in Fig. 42. Red circles highlight additional features suggested by FRX-L personnel at the design review: (I) an array of fiber optic feed-throughs above each rail gap; (II) an extension to Main bank bus plates; (III) notches in the bracket supporting rail gaps for Rogowski coils.

The second addition (II) was derived following a more careful examination of the spacing between the Crowbar switch hardware and the backs of the capacitors in the upper half of the Main bank. While posing no problem with electrical breakdown since both the capacitors and the Crowbar switch bus work are all at the same potential, it was apparent that the spacing would be extremely confined and would complicate assembly and maintenance. Therefore, the extension to the bus plates shown between the Main bank bus plates and the proposed Crowbar bus work was added.

Addition number III provided an additional means of diagnostic access in the new Crowbar switch that was not present in the original. Though not clearly seen from the view in Fig. 43, it was suggested that slots be added to the support bracket on the “ground” side of the rail gaps, so that individual Rogowski coils might be looped around the bracket segments under each rail-gap switch to monitor the currents passing through them. In conjunction with the fiber optic array, this feature would provide a second verification that each Crowbar rail gap was indeed operating during each shot, and it would also show how uniformly the current was distributed among the four rail gaps.

3.1.4 Fabrication, Delivery, and Assembly of the New Crowbar Switch

Following the design review, each of the three hardware additions/modifications discussed above were incorporated into the final detailed parts drawings for both the FRX-L Crowbar switch and the FTX Crowbar switch (described earlier in Section 2). Fabrication of the hardware for the

FRX-L Crowbar switch then began once the drawings were completed and after the next funding increment had arrived from the OFES.

Once fabrication was completed and the parts had arrived in house at AFRL, SAIC personnel inspected and test fitted each component to ensure that they had the proper dimensions and tolerances (Fig. 44). A few minor problems were discovered initially, such as the fact that the spacing between rail-gap switches was slightly different than anticipated or that certain bolt holes were not drilled correctly or not drilled at all. However, these problems were quickly corrected, either by the vendor or by our in-house machine shop.



Figure 44. Photo of the new Crowbar rail gaps and several of the new Crowbar hardware items during a trial assembly at AFRL.

With regard to the best approach to testing the new switch, initially it was felt that it would be more expedient to test it at AFRL, since by doing so the FRX-L experimental campaign would not have to be interrupted and the system taken off line to install the switch. In that case SAIC personnel would install the crowbar switch onto the FTX Main bank once the design work for it had been completed and the hardware fabricated and assembled. Characterization tests with the new Main bank could then be performed at the same time as the tests with the Crowbar switch, using a dummy load in which to discharge the bank. The proposed series of tests would, therefore, have been very similar to those that were done with the first crowbar switch in FY01. This decision was later reversed, however, because it was noted that while FRCs could possibly be formed on FRX-L with the densities and temperatures within the desired range, the FRC lifetimes would never reach acceptable values, for the reasons discussed earlier, as long as the first Crowbar was used with its excessive modulation of the Theta coil current waveform.

To reduce the down time, therefore, that would come with setting up the new Crowbar switch immediately on FRX-L, the Crowbar hardware was partially assembled in advance – including mounting it to a new quad set of rail-gap switches – in AFRL’s Building 322 before shipping. A special rail gap assembly table was borrowed from Titan Pulse Sciences Division in order to bond the four Crowbar rail-gap switches together. Also as part of this effort, SAIC personnel prepared the gas fill and exhaust lines for the rail gaps and fabricated and calibrated the four Rogowski coils that were to be placed around the ground-side supports of each of the four rail gaps.

When all of the preparatory tasks that could be performed were completed, the hardware was carefully boxed or otherwise secured for transportation up to LANL. Personnel then transported the hardware up to the FRX-L facility at the beginning of November 04 and returned later that month to work with FRX-L personnel in quickly installing the new switch. Figure 45 shows several photos of the crowbar switch at various stages during the assembly process. Figure 46 provides a view of how the Rogowski coils were positioned around the Crowbar rail gaps and how diagnostic cable connections were then made to them.



Figure 45. FRX-L Crowbar switch installation: (a) view of the Crowbar rail gaps and ground bus work being mounted on the back of the Main bank; (b) the nylon anti-tracking tubes and Lexan side cover have now been placed on the cable header portion of the switch; (c) the Lexan end covers and the hot bus bar of the cable header have now been attached; (d) a view looking down on the FRX-L Crowbar switch after the rail gap covers and gas feeds have been installed and the top bus plate over the switch has been bolted into place.

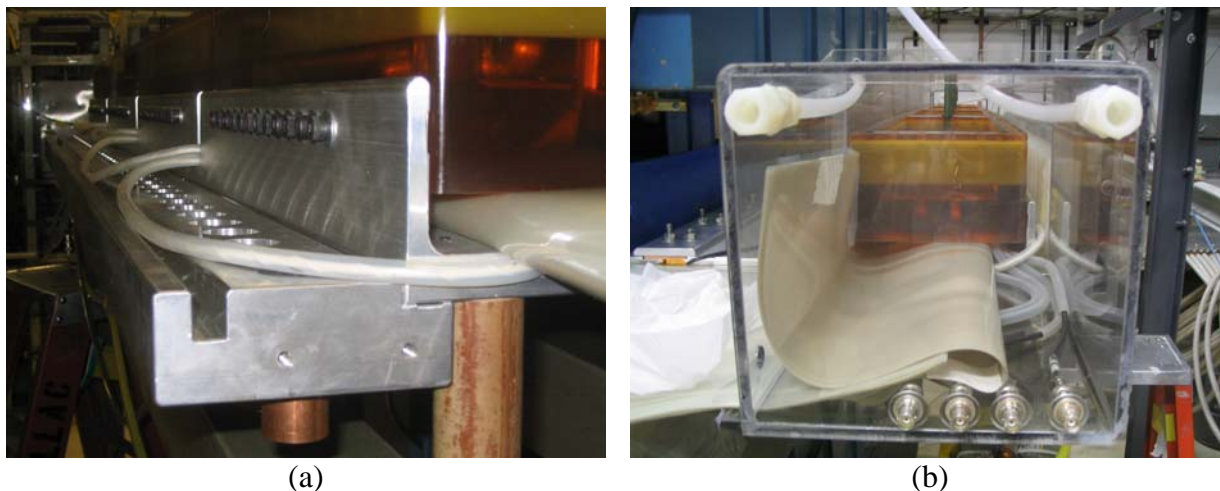


Figure 46. Closer view of the crowbar current diagnostics: (a) four Rogowski coils (pushed up against the L-bracket when the Nylon anti-tracking tubes were installed) monitor the current flow in each rail-gap switch; (b) connections to the Rogowski coils are made at the west Lexan end cover.

The majority of the assembly was actually completed in a day. Only the re-termination of the RG-17/14 cables remained, as well as a couple of minor changes that were needed on the trigger board to enable connections to be made to the new Crowbar switch. FRX-L personnel took care of completing these few remaining tasks during the next couple of days. Once this work had been accomplished, along with a few additional maintenance tasks and some other minor modifications to the FRX-L systems, the experimental effort was ready to begin again.

Shortly after the installation of the new crowbar switch, FRX-L personnel requested a couple of slides noting the improvements in the new switch compared to the previous switch. In response (and with the goal of completeness and of carefully documenting all of the new switch's properties), several additional slides were prepared, as well. This set of slides not only explained how the hardware changes should reduce the modulation in the Theta coil current, but also how the new geometry should be less sensitive to changes in Theta coil inductance and to the time at which the Crowbar switch is triggered. (Floating the Crowbar trigger generator with the Main bank, one of the proposed solutions to the problem limiting the variation in trigger timing for the Crowbar switch, was still recommended, however, in the hope that it would allow the operator to freely vary the time of crowbarring the Theta coil current if needed.) These slides are included in Appendix D for reference.

3.1.5 Evaluation of the Initial Operation of the New FRX-L Crowbar Switch

By July 05 on the order of 100 Main-Bank shots had been performed with the new Crowbar switch. Main bank charge voltages were varied from ± 25 kV to ± 40 kV, and overall the performance of the switch clearly met or even exceeded expectations. As demonstrated by the plot of the axial magnetic field in Fig. 47, the modulation was greatly reduced compared to that observed with the former crowbar switch.

Initially there was some difficulty getting the Crowbar switch to trigger well and have all four rail gaps conduct current (evidence that the original triggering problem still persisted), but after

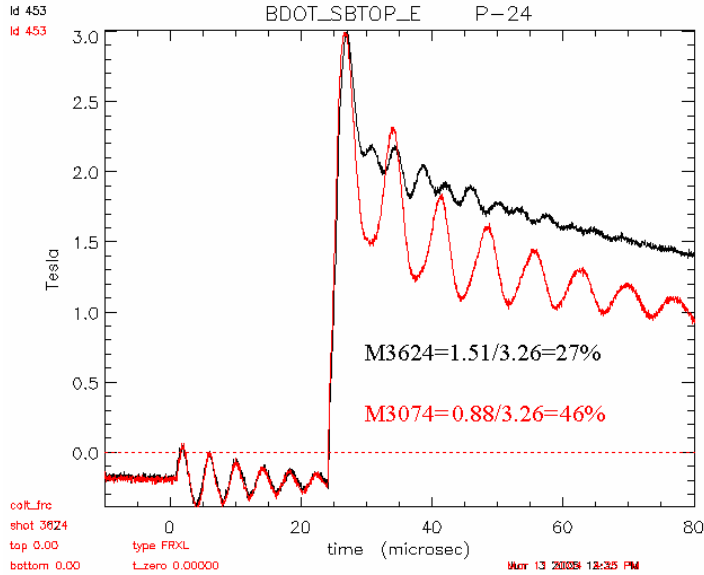


Figure 47. Waveforms from a B-dot probe inserted in the top of Theta coil segment B. The red waveform was recorded during a shot with the old Crowbar switch and black during a shot with the new switch. The drop in flux density following the initial peak is only 27% with the new Crowbar switch, compared to 46% with the old. This drop is somewhat dependent on the extent of the trigger delay following the Theta coil current maximum.

the Main bank-to-Crowbar switch trigger delay was extended by a few hundred nanoseconds, more reliable operation was then obtained. The best operating (triggering) point for the switch is now, in fact, slightly after the Theta coil current maximum has been reached; this is part of the reason for the initial large peak seen on the magnetic field waveform in Fig. 47 before it begins its exponential decay.

Even after adjusting the triggering delay, however, there was still some difficulty with getting both of the two inner rail gaps to conduct during the same shot. Sometimes only gap #2 would conduct, and at other times only gap #3 would conduct. Similar problems had occurred once before with getting gap #4 to conduct on the previous Crowbar switch right after the switches had been cleaned. At that time it is possible that some contaminant, such as oil or another solvent besides alcohol, had inadvertently gotten onto the electrodes of that gap, effectively “poisoning” it after the first shot and preventing it from starting conduction within a reasonable amount of time during subsequent shots. Re-cleaning the gap immediately corrected the problem at that time, however, but in this case it did not seem to help.

Though not consistent, the Rogowski coils monitoring each of the Crowbar rail gaps tended to show higher currents passing through the two outer rail gaps (gaps #1 and 4) and lower currents passing through the two inner ones (gaps #2 and #3) (Fig. 48). This behavior suggested that the voltage drop across the outer two gaps was higher than that across the inner gaps, and it was then hypothesized that the gap spacing on the inner two rail gaps could be reduced to compensate for this difference and thereby increase their triggering reliability.

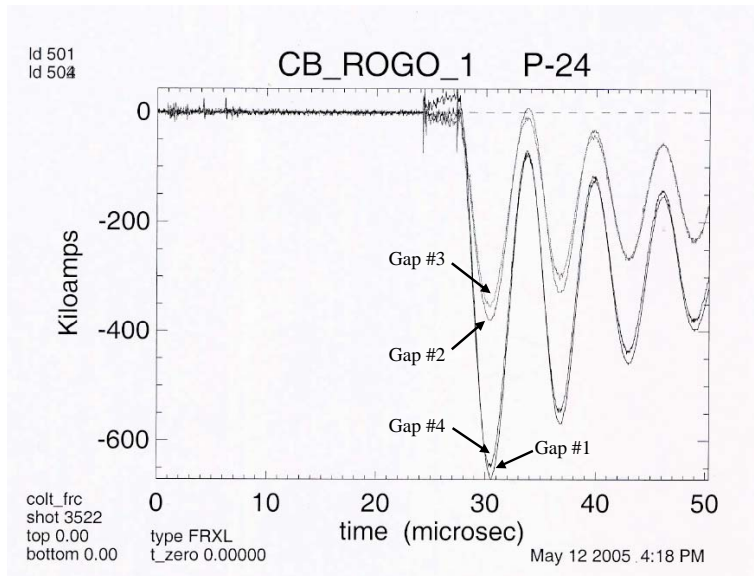


Figure 48. Current waveforms recorded with the Rogowski coils around each of the crowbar switch rail gaps. During typical shots it was observed that the current passing through the outer two rail gaps was higher than that passing through the inner two. Currents were often, but not always, balanced between the gaps in each pair, as shown here.

To determine how much the gap spacing of the inner two rail gaps should be decreased, the electric fields across the electrodes in the inner and outer pairs were considered. Because it was desired to keep the pressure in all four rail gaps the same and to have all four rail gaps close to the same operating point on the electric field vs. pressure curve, it seemed clear that the adjustment simply needed to be sufficient to equal out the electric fields in both pairs of gaps. The electric fields $E_{2,3}$ and $E_{1,4}$ were then estimated in the following manner.

The rail electrodes have approximately a cylindrical geometry, and from Sarjeant and Dollinger (High-Power Electronics, Tab Books, Inc., Blue Ridge Summit, 1989, p. 176) the maximum electric field between two parallel cylinders can be calculated from the expression

$$E_{\max} = \frac{U/2}{2.3 \cdot r \cdot \log \frac{r+a/2}{r}}, \quad (6)$$

where U is the voltage between the cylinders, r is the radius of the cylinders (in cm), and a is the surface-to-surface spacing between the cylinders (also in cm). The radius of the electrodes in the rail-gap switches is $1.5'' = 3.81\text{cm}$, and the typical gap spacing of the Crowbar switch electrodes (for 100 kV max operation) is $0.708'' = 1.80\text{ cm}$. The voltage drop, U , across the inner and outer pairs of gaps was estimated from the rail-gap current waveforms recorded during several “typical” shots. In general

$$U = L \frac{dI}{dt} + RI, \quad (7)$$

but just after the gaps are triggered and before current really begins to flow ($t = 0^+$) this expression simplifies to

$$U = L \frac{dI}{dt}, \quad (8)$$

By then taking the time derivatives of the recorded current waveforms, average values of dI/dt at $t = 0$ were found for the gap pairs: $dI_{1,4}/dt = 3.2 \times 10^{14}$ A/s and $dI_{2,3}/dt = 2.5 \times 10^{14}$.

Substituting Eqn. (8) into Eqn. (6), and plugging in the above values for dI/dt , a , and r into the resulting equation, two expressions for the gap electric fields are obtained:

$$E_{1,4} = \frac{3.2 \times 10^{14} L}{17.526 \log(1.236)} \quad (9)$$

and

$$E_{2,3} = \frac{2.5 \times 10^{14} L}{17.526 \log \frac{3.81 + a_{2,3} / 2}{3.81}} \quad (10)$$

When Eqns. (9) and (10) are set equal to each other, the appropriate electrode spacing for the inner two rail gaps $a_{2,3}$ is found to be 1.373 cm or 0.541". When first attempting to re-gap the inner two rail-gap switches to this new spacing, it was discovered that the bolt slots in the electrodes were not long enough to allow the electrodes to be slid this close together. As a result, an intermediate electrode spacing of 0.637" was chosen.

Following the re-gapping procedure, there did in fact appear to be some improved reliability with making both inner rail gaps conduct current together. Interestingly, however, the current distribution among all four rail gaps had changed in an unexpected way, as is illustrated by the plot of the four rail-gap current waveforms shown in Fig. 49. Though this exact current distribution was again not always consistent, the tendency was that the highest current flowed through gap 1 with the current steadily decreasing towards gap 4. This particular distribution of current does not appear to affect the operation of the experiment in any way (based upon the magnetic field measurements at the Theta coils), and since the triggering of all four Crowbar rail gaps became more consistent, attempts were not made at that time to modify the current flow distribution any further.

3.1.6 Analysis of Triggering Problems With the New Crowbar Switch

The overall performance of the new Crowbar switch continued to be extremely good as experiments continued, but unfortunately the difficulties with getting all four of the rail gaps to conduct during a given shot returned after a few months. The problem was intermittent at first, but by August 05 the problems became much more consistent for some reason. Unlike the previous instance where only gap #2 or gap #3 was not conducting, this time the gap that was not conducting was fairly random from shot to shot.

At this point, FRX-L personnel decided to implement a scheme that had been proposed some time ago to isolate the Crowbar trigger system from the PI and Main bank trigger systems and to

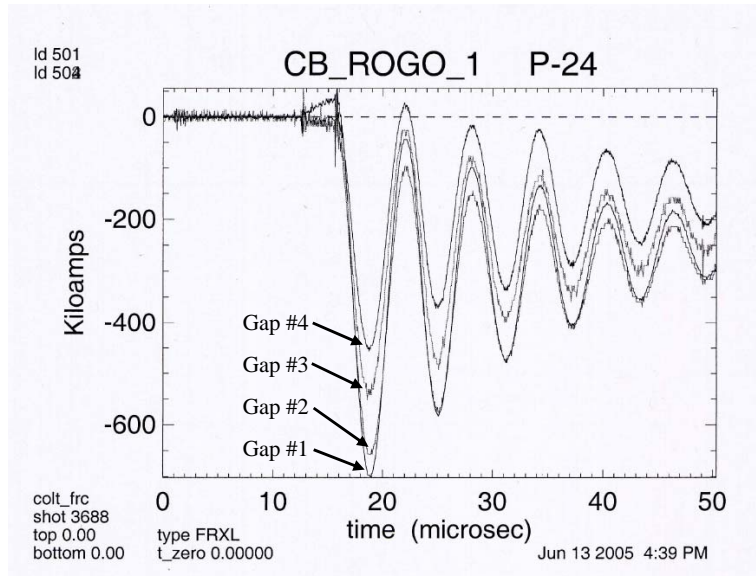


Figure 49. Current waveforms recorded with the Crowbar Rogowski coils following the re-gapping of the inner two rail-gap switches. During typical shots it is now observed that the current is highest in gap 1 and steadily decreases toward gap 4.

let the whole system float with the Main bank during shots. The Maxwell 40168 trigger amplifier and its fiber optic trigger receiver were placed in an RF-shielded equipment rack along with a UPS that would provide power to these units during shot operations. Three Jennings switches (for hot, neutral, and ground) were used to break contact between the UPS and the wall power as soon as high voltage was enabled on the 40168. Both the rack and the master trigger generator were placed on insulating blocks and, together with the RG-218 trigger cables running to the crowbar switch, were kept physically separated from all other components on the experiment.

Despite the fact that having the trigger system isolated and floating during a shot would seem to be a proper pulsed power practice, there was in fact no discernable change in the performance of the Crowbar switch when tests were conducted again. (It was noted, however, that if the Crowbar trigger system was subsequently left grounded during a shot or if the equipment rack door was left open, the Main bank trigger unit could then readily cause the Crowbar trigger unit to fire when the former was triggered. As long as careful attention was given to these details, however, pre-firing of the Crowbar trigger system was not an issue.) Because of the absence of any change in performance, greater attention was then given to the pulsed power data measured at the Main bank and Crowbar switch during each shot. Such data included signals from the trigger monitors located on the western-most Main bank and Crowbar switch trigger cables (the delay between the two is compared with the delay generator setting in the FRX-L screen room), the signal from the Crowbar voltage monitor, and the current waveforms from each of the Crowbar Rogowski coils. A measurement of the total current from the Main bank and Crowbar switch was obtained from the Theta coil Rogowski. Observations from the data were as follows:

- The delay between triggering the Main bank and the Crowbar switch, as determined from the trigger monitors, always agrees quite well with the delay generator setting.

- The four Crowbar rail gaps prefer being triggered 3.0 μs following the Main bank trigger; when attempting to trigger earlier or later only three rail gaps tend to conduct.
- Examination of the actual delay between the start of current from the Main bank (determined from the Theta coil Rogowski signal) and the start of current through the Crowbar rail gaps (determined from each of the Crowbar Rogowski signals) showed an additional *1 ~ 2 μs or more* beyond what the trigger monitors indicated. (The total delay was 4 μs or greater.) This “turn-on” time for the switches is excessive.
- Such an extended delay between triggering and the start of conduction could be from
 1. The gas pressure being too high and/or electrode spacing being too great;
 2. The voltage across the switch being too low;
 3. Improper biasing on trigger electrode;
 4. The trigger pulse not having sufficient amplitude, energy, and/or dV/dt .

Items 1 and 2 are somewhat related through the dependence of the breakdown electric field on pressure, voltage, and electrode spacing. We know from both the Crowbar voltage monitor and the oscillation period of the Theta coil current waveform that the voltage across the Crowbar rail gaps is typically very low when they are triggered. Test shots at decreased switch pressures seemed to produce no discernable effect, so when it was time to clean the rail-gap switches again the gap spacing between the rail electrodes was decreased further to 0.577 in. (essentially to a spacing appropriate for ± 40 kV operation). To make this adjustment, it was necessary to increase the length of the slots for the bolts in the rail electrodes. As a starting point, the same gap spacing was set in all four Crowbar rail gaps.

While the cleaning and re-gapping were being performed, the bias resistors connected to each of the rail gap trigger terminals were also checked again for any abnormalities in their values (Item 3 in the list above). The following resistances were recorded:

- CB#1 upper = 1.64 k Ω , CB#1 lower = 1.54 k Ω
- CB#2 upper = 1.56 k Ω , CB#2 lower = 1.46 k Ω
- CB#3 upper = 1.60 k Ω , CB#3 lower = 1.52 k Ω
- CB#4 upper = 1.80 k Ω , CB#4 lower = 1.48 k Ω

The largest deviation is for rail gap #4, where the actual bias appears to be 55–45 (as opposed to 50–50), but this particular rail gap was actually one of the least problematic ones at the time.

Prior to resuming tests, FRX-L and SAIC personnel met with two other LANL personnel, Mr. William Hinckley and Mr. Robin Gribble, who have considerable experience in working with rail-gap switches. The triggering problems and delayed turn-on times were discussed, and Mr. Hinckley pointed out several of the same issues noted in Items 1 through 4 above as possible causes of this behavior. Mr. Gribble suggested the possibility of using air in the switches. While multi-channeling might be reduced, he had found from his experience that turn-on times for switches could be considerably faster with air. He also noted that the inductance increase from lower multi-channeling was not terribly severe as long as the channels that were present were not concentrated in one location. Mr. Gribble stated that higher pressure combined with decreased

gap spacing for a given voltage would further help to improve turn-on time and reduce jitter. With these ideas in mind, it was decided to perform a few tests with air in the rail-gap switches.

Table 2 summarizes results from the 16 Main bank test shots following the re-gapping of the Crowbar rail-gap switches. The Main-to-CB-#1, -#2, -#3, and -#4 times were determined based upon the apparent starting times of the Main bank and rail-gap current signals recorded with the Theta coil and the individual Crowbar Rogowski coils, respectively. A blank in the table indicates that the particular rail-gap switch did not conduct during the shot. As noted, the first three (shots 3861–3863) were performed with SF₆/Ar in the Crowbar rail gaps, as usual, and the remaining shots (shots 3870–3882) were performed using compressed air, based upon Mr. Gribble’s suggestion.

Table 2. Delay times between Main-bank triggering/current start and crowbar triggering/current start for several shots following the crowbar-switch re-gapping.

Shot Num.	Main Vcharge (+/- kV)	Rail Gap Pressure (psi)	Delay Gen Setting (μs)	Measured Delay from Trig Monitors (μs)	Main to CB #1 (μs)	Main to CB #2 (μs)	Main to CB #3 (μs)	Main to CB #4 (μs)	Comments
3861	25	9	3	3.07	3.92	4.137		3.739	SF ₆ /Ar in rail gaps.
3862	25	9	3	3.044	4.073	3.89		4.073	
3863	25	9	3	3.036	4.093	4.004		4.183	
3870	25	20	3	3.039	4.204			4.705	Comp. air in rail gaps.
3871	25	18	3	3.017	4.711			3.930	
3872	25	16	3	3.052	4.437			4.463	CB trig'd early by Main trigger.
3873	25	12	3	0.532	0.750	0.691	0.573	0.810	
3874	25	12	3	3.035	3.765			4.392	
3875	25	9	3	3.012	4.011	5.643		4.654	
3876	25	9	2.5	2.535	5.635	5.127	9.190	5.105	
3877	25	9	2	2.076	5.020	5.111	6.424	5.038	
3878	30	13	2	2.021	4.917		5.463	5.167	
3879	30	11	2	1.968	5.015	5.087	5.395	4.422	
3880	30	11	1.8	1.847	4.830	4.427		4.533	
3881	30	11	1.8	1.883	5.763		4.789	4.349	
3882	30	11	3	3.074	3.973			4.430	CB voltmeter on CB#1 trig terminal

Right away it was observed that Crowbar rail gap # 3 had trouble conducting with either gas. With air, rail gap #2 did not conduct until switch pressures were decreased to values closer to those typically used with the SF₆/Ar mixture, and even then it failed to conduct at times. Rail gaps #1 and #4 did consistently conduct, however. It was obvious, therefore, that with a return to a uniform gapping for all four of the rail-gap switches the initial problem encountered with the new Crowbar switch – that one of the inner two gaps was resistant to being triggered – had returned, even though all gaps were set at a closer spacing now. The obvious solution was then to try an even smaller gap spacing for the inner two switches, and this change was made approximately a week later.

Other observations from the data in Table 2 are that we did not observe the faster turn-on times that Mr. Gribble suggested we might be able to obtain; rather, we still observed the same excessive delays of 1 ~ 2+ μs between triggering and the start of current conduction. The only fast turn-on time that was observed was for Shot 3873, during which it was suspected that the Main-bank trigger caused the crowbar trigger to fire very early. In addition, the jitter in the triggering of all four of the rail gaps is also quite high, as is evidenced by the rather extreme variation in these delay times for a given rail-gap switch from shot to shot. It is possible that the

gap spacing would need to be decreased significantly further and the pressure increased accordingly to reach the regime of operation that Mr. Gribble described, but this would not be possible without further lengthening of the bolt slots on the rail electrodes.

The overall performance of the Crowbar rail gap switches was also somewhat poorer when pressurized with air. Though not extreme, the Theta coil Rogowski indicated an increase in the modulation of the crowbarred Theta coil current even for shots when all four rail gaps conducted. This performance can be explained by the expected decrease in multi-channeling when pressurizing the switches with air.

For shots 3881 and 3882 the Crowbar voltage monitor was connected to the trigger terminal of Crowbar rail gap #1. The voltage monitor itself is simply a known resistor with a resistance (588 Ω) that is large compared to that of either the Theta coil or the Crowbar switch when the Crowbar is conducting. The monitor's low-voltage connection passes through the bore of a Pearson current transformer (model 110) that in turn provides a measurement of the current through the known resistor. When this monitor resistor was placed in parallel with the 1.54 k Ω resistance of the lower part of the rail gap #1 bias network, an equivalent resistance of 425.5 Ω was obtained. In series with the upper bias resistance of 1.64 k Ω , a voltage division of 0.26 was then obtained. Measurements of the "bias" voltage during shots 3881 and 3882 showed a voltage of approximately one-quarter of the total voltage applied across the Crowbar switch. Though this measurement ended up perturbing the normal bias voltage somewhat, it provided a second verification that (without the monitor attached) the bias voltage should indeed be correct on each rail-gap trigger terminal.

Thus, while this series of tests verified the proper biasing of the Crowbar rail-gap switches and the benefit of having a smaller gap spacing for the inner two switches, it failed to provide any insight into why the delay between the triggering of the Crowbar rail gaps and the time current conduction starts has been so excessive. The inner two Crowbar rail gaps were re-gapped as planned following these tests to 0.517 in. (essentially to a spacing appropriate for ± 35 kV operation), and, again, in the months that followed all four Crowbar rail-gap switches returned, in general, to operating quite well. As a result, investigating the triggering issue was moved down in priority at that time in favor of concentrating on other issues related to the experiment, which will be discussed shortly.

Most recently, however the triggering problem has returned again. A rather involved solution has been proposed by FRX-L personnel for addressing it this time, and SAIC personnel have been in the process of designing the necessary hardware required for implementing this solution and then having that hardware fabricated. This potential solution attempts to inductively isolate the adjacent rail-gap switches from each other, and it will be described in greater detail in both the next sub-section and in the first part of a memo included in Appendix E. (This memo was prepared a couple of months ago before hardware fabrication began in order to brief FRX-L, AFRL, and other SAIC personnel of the idea.) At the time of the writing of this report, fabrication of the hardware has been completed and delivered to the FRX-L facility, and it is scheduled to be installed within the next several days. Experimental data showing the level of effectiveness of this modification to the switch should be available in as little as a week.

In concluding this discussion of the FRX-L Crowbar switch triggering problems, several additional observations should be noted. First, Item #4 in the list of possible reasons for the excessive trigger-to-conduction delay (insufficient amplitude, energy, and/or dV/dt in the trigger pulse) still has not been carefully examined. A scheme for attempting to correct the triggering problem from this angle is also briefly described in the memo included in Appendix E.

Furthermore, since the Crowbar switch is now being triggered on the falling slope of the Theta coil current waveform, the voltage across the Crowbar switch is shifting to a negative polarity when it is being triggered. This situation is different from that of the first crowbar switch, where triggering took place just before the current maximum, at a time when the voltage across the switch was still positive. Because of this earlier triggering time, the crowbar trigger system had been configured to provide a negative trigger pulse at that time, and this has not been changed. Thus, changing the trigger pulse polarity is another task that should be kept under consideration.

Also, SAIC's Mark Babineau has recently pointed out two additional observations related to the FRXL setup: 1) spark gap switches having a positive applied voltage typically do have more jitter and must be operated at lower pressures than switches with a negative applied voltage of the same amplitude, and 2) a UV light source could be introduced above each of the rail gaps to help reduce this jitter by stimulating electron emission. Though switch pressure has, in fact, been reduced during some of the tests, the pressure may not have been reduced by a sufficient amount or for a sufficient number of tests to allow any improvement in triggering to be observed. The UV light source, like the method of increasing the trigger pulse amplitude described in Appendix E, offers significant promise and would actually be easier to implement. It is likely, therefore, that development of a UV source will be pursued first if the inductive isolation scheme does not prove to be totally effective.

If the positive polarity of the Main bank is truly the issue, as a worst-case attempt to solve this problem, the polarities of all of the banks could be changed. In such a case, the Main bank would then drive a negative current through the Theta coil, and there would be a negative applied voltage across the Crowbar switch when the bank is first discharged. With this configuration the FRX-L experimental setup would then finally match the original Crowbar switch test setup at AFRL in all respects.

Finally, it should be noted that once FRC translation studies begin, the performance of the Crowbar switch and its trigger system may no longer be of particular concern, as the FRC will be leaving the Theta coil region very quickly after formation is completed, which is around the time of the Main bank current peak. Acceleration of the FRC should even start while formation is still in the process of occurring. Thus, if one Crowbar rail gap fails to start conducting, the FRC will likely not "notice" the resulting increase in modulation in the magnetic field, as it will have left the Theta coil region and moved into the essentially constant magnetic field of the translation region. Only if the modulation for some reason causes the Theta coil field to drop below the field in the translation region before the FRC has fully entered it will this be a problem, as the FRC would then get pushed back in to the Theta coil region.

3.1.7 Slotted Bus Plate Design For Rail Gap Inductive Isolation

As was just mentioned above, the Crowbar switch has again in recent months started exhibiting the triggering problem that has plagued it since its installation on FRX-L, whereby one or more of the rail-gap switches are not conducting current when the Crowbar is triggered. A new idea to

address this problem has been put forth by FRX-L personnel and is now in the process of being implemented. This idea involves putting slots in the Crowbar switch bus work on the hot side of the switch with the intension of inductively isolating the individual rail-gap switches from each other. Part of the difficulty with getting the rail gaps to start conducting lies with the low voltages that are across the Crowbar switch when it is triggered. If for some reason one rail gap takes a little longer to begin conducting, the start of conduction in the gap(s) adjacent to it will then cause what little voltage that was present to collapse, thereby preventing the slow rail gap from ever breaking down and conducting. By putting slots in the bus work and introducing a measure of inductive isolation between the rail gaps, there should be more time available for each gap to begin conducting. A Solid Works® rendering of the Crowbar switch assembly illustrating this proposed slotted-bus-plate concept is shown in Fig. 50.

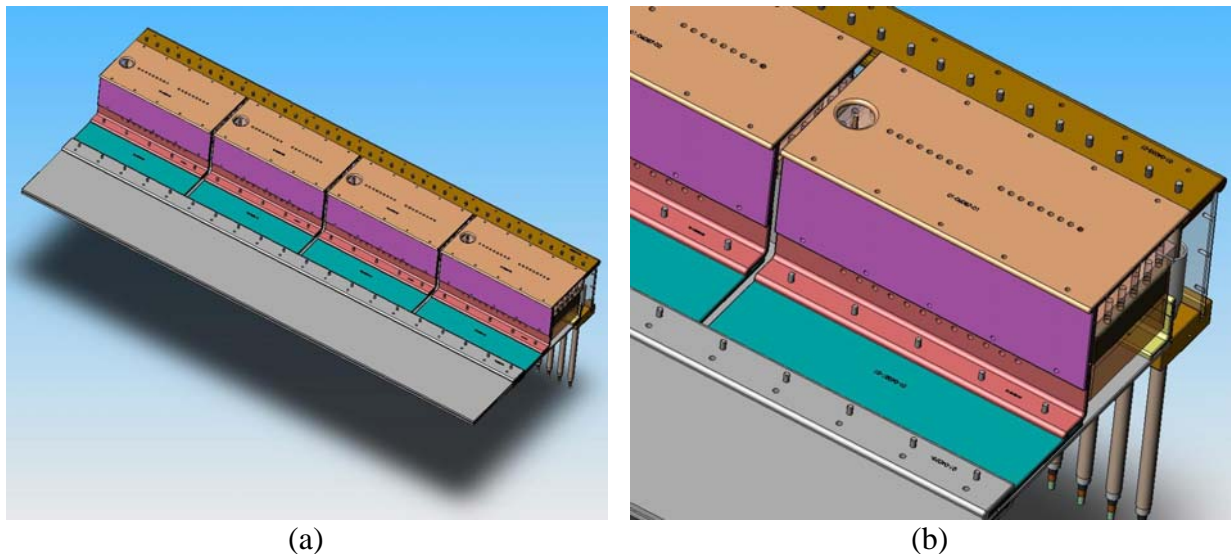


Figure 50. (a) Solid Works® rendering of the Crowbar switch assembly with 1.27-cm-wide slots cut in the hot bus plates between the rail-gap switches. (b) Close-up view near one of the rail-gap switches to show the slot more clearly.

SAIC personnel have performed an analysis of the effects of slotting the bus work and from this analysis have estimated an appropriate length of slot to insert both upstream and downstream of the Crowbar rail gaps. This analysis was outlined in a memo sent to FRX-L, AFRL, and other SAIC personnel for their review, and as was mentioned in the previous sub-section it is also included in Appendix E of this report. After reviewing the memo, FRX-L personnel decided to proceed with implementing this concept. To reduce down time on the experiment they decided, however, that a separate set of slotted bus plates should be fabricated rather than attempt to have the existing set modified. In this case, the down time on the experiment would be only that which is required to change out the bus plates.

SAIC mechanical engineers then began preparing detailed design drawings of the new bus plates and angle bracket supports that were required for the Crowbar switch, and an internal design review was held among SAIC personnel before presenting the final drawings to FRX-L personnel. In this design review, the question was raised of how much mutual coupling there would be between the plates and whether or not a greater spacing (i.e., slot width) than 0.5 in. (1.27 cm) would be needed between the bus plate segments to reduce this coupling and ensure

that the level of isolation required between rail gaps will indeed be obtained. A couple of Quick Field analyses were performed to answer this question. The analyses looked at both the parallel plate transmission line region leading up to the Crowbar switch and the bus bars on each side of the Crowbar rail gaps. In both cases, there did not appear to be any significant coupling on the time scales that are relevant for the FRX-L experiment (a sinusoidal signal with a 3- μ s quarter-cycle rise time, approximately the same as the Main bank quarter-cycle rise time, was used in the analysis). The results of these analyses were described in second memo that was again sent to FRX-L, AFRL, and other SAIC personnel for their review, and this memo is included in Appendix F of this report.

Following a review of the memo and the detailed hardware drawings that had been prepared, FRX-L personnel then arranged for the fabrication of the segmented bus plate parts at a local machine shop. As has already been mentioned, the fabrication work was recently completed and the hardware delivered to AFRL's Building 322. Following an inspection and test fitting of the new hardware (Fig. 51), SAIC personnel carefully packed up the bus plate pieces and transported them to the FRX-L facility, where they will be installed on the FRX-L Crowbar switch assembly very soon.



Figure 51. Photos of (a) the bank side and (b) the Theta coil side of the new Crowbar switch slotted bus work during its test fitting. As is shown in (b), two single rail-gap switches were set out and spaced appropriately to allow the bolt-hole spacing and the sizes of parts to be checked.

3.2 IMPLEMENTATION OF PASSIVE MIRROR CONCEPT

It was concluded from tests on FRX-L during the fall of 2005 that the FRCs being formed in the experiment were accelerating out of the Theta coil region rather quickly after formation. (These events were determined through the use of a six-channel spectrometer that received light signals from six optical fibers placed at various positions along the length of the quartz vacuum vessel.) Thus, the short FRC “lifetimes” that have been observed up to this point were not necessarily a result of their rapid decay but may have been due simply to their leaving the formation region where they were being diagnosed.

As a result, a plan was developed by FRX-L personnel, with the aid of a magnetic field analysis code developed by a graduate student at the University of Nevada-Reno, to set up a “passive” mirror on each end of the Theta coil to increase the magnetic field strength at these locations and thereby trap the FRC inside the Theta coil so that it could be diagnosed for its full lifetime. Each passive mirror consisted simply of two halves of a ring, approximately 6 cm in axial length, which bolted onto the sides of the outer Theta coil segments. The passive mirror, therefore, derives its current from the three banks already driving the Theta coil, and a slightly smaller (by 3 mm) inner radius for the rings provides the necessary increase in field strength over that in the adjacent Theta coil. Figure 52 shows a 3-D rendering and a cross-sectional view created by SAIC personnel using Solid Works® that illustrate how the mirror rings were to be attached to the Theta coil. Figure 53 is a close-up view highlighting the details of the passive mirror ring bore.

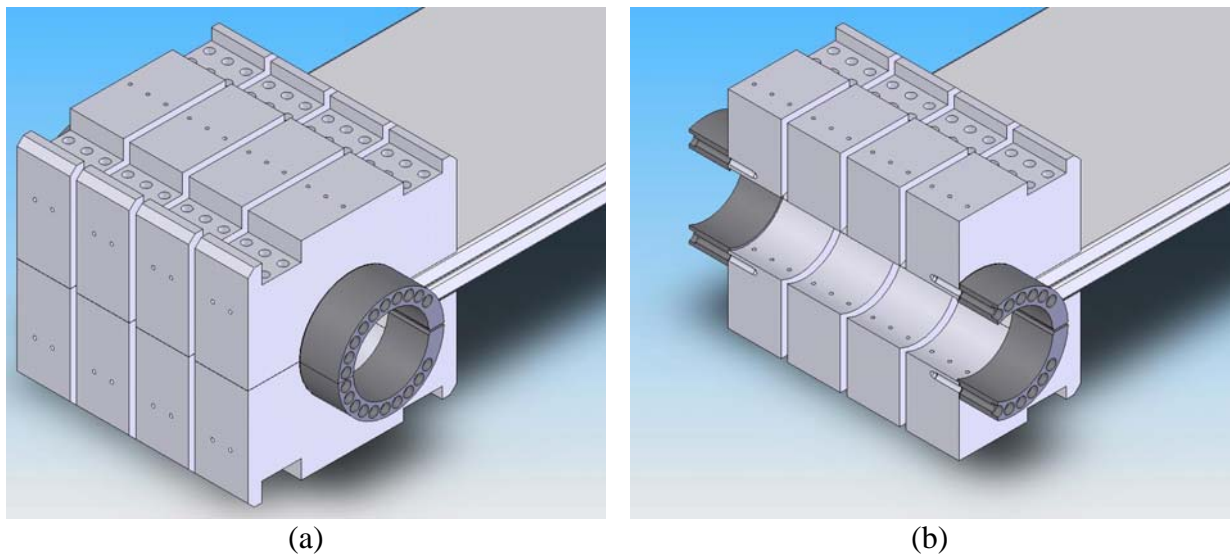


Figure 52. (a) Four-segment Theta coil with passive mirror rings attached on the outside segments. (b) Cutaway view showing the outside segments of both sides of the Theta coil with their mirror rings.

In addition to preparing the illustrations in Figs. 52 and 53, SAIC personnel assisted the FRX-L team in this effort by preparing the outer Theta coil segments so that the mirror rings could be attached (i.e., the necessary bolt holes were bored and tapped in the two pairs of Theta coil segments), by ordering the copper-shim stock needed for current-joint gaskets between the mirror rings and the Theta-coil segments, and then by helping with the assembly of the passive mirror setup once FRX-L personnel had completed the fabrication of the mirror rings.

Unfortunately, the passive mirrors did not have the beneficial effects that were desired. While computer modeling had showed that the smaller radius on the mirror pieces would provide an appropriate increase in magnetic field at the ends of the Theta coil to help confine the FRC, it is suspected from the poor results that were obtained (i.e., the lack of any notable FRCs being formed) that either the mirror fields may not have been azimuthally uniform after all because the width of the feed from the transmission line was not extended to match the width of the mirror pieces (and thereby feed the mirror pieces directly) or by moving the flux excluder plate and Cusp coils further from the Theta coil to make room for the mirror pieces a more detrimental

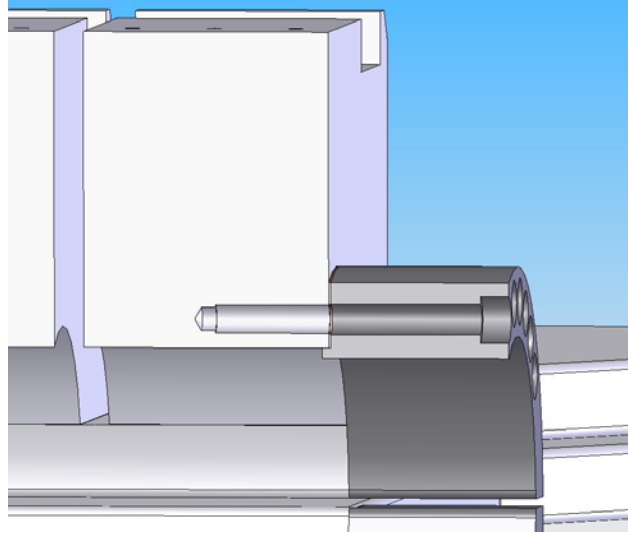


Figure 53. Close-up view of one end of the Theta coil showing the step down in the inside radius of the mirror ring. The ring also has a lip that extends inside the bore of the Theta coil segment to aid with centering the ring.

magnetic field configuration was established. In the case of the former, the current was left to spread out into the mirror pieces only after it had first entered the main Theta coil segments, and this possibly created a low-field region in the mirror field near the transmission line feed that prevented the FRC from forming properly. In the case of the latter, with the flux excluder plates and Cusp coils further from the Theta coil, the initial magnetic null between the Bias and Cusp fields may have been too far from the Theta coil, and the Bias and Main field lines could not then connect during the Main field compression, again preventing the FRC from forming properly.

Following this series of experiments, FRX-L personnel removed the mirror pieces and repositioned the Cusp coils in a configuration more closely resembling one in the past that had led to good FRC formation. The 0.64-cm thick stainless steel flux excluder plates were also replaced at that time with 0.025 cm copper sheets to not only limit the penetration of the Main field into the Cusp coils but to also limit the Cusp field penetration into the Theta coil region. With the Cusp field reduced in this manner, the starting Bias field in the Theta coil region is then higher, leading to hopefully a higher trapped flux in the FRC, and the null is kept close to the desired location. Results to date have indeed indicated that FRCs are being formed again and, at least in a few cases, with increased lifetimes over those observed in previous shots. Problems with the Crowbar switch triggering have made it difficult to perform repeatable shots, though, from which the data can be compared and trends observed.

3.3 DESIGN SUPPORT FOR FRC TRANSLATION EFFORTS

During the periods of time when the FRX-L Crowbar switch has been performing well, the efforts of the FRX-L team have concentrated on determining the various parameters and conditions required to repeatedly form FRCs with the appropriate MTF target characteristics (density, temperature, trapped flux, etc.). Work has also begun on the design and development of the additional hardware needed to begin FRC translation experiments on FRX-L. SAIC personnel have been able to provide support to FRX-L personnel in these areas by performing a

few analyses on some of the capacitor bank designs that have been proposed for the FRC translation setup.

The first bank design proposed is actually a replacement for the existing Bias bank that would allow a higher Bias field to be generated with a shorter pulse duration. The simulations and analyses performed on this design concept are summarized in a memo that was sent to FRX-L personnel, which is also included in Appendix G of this report. The second bank design concept would be used for driving the Guide and Mirror field coils, and this analysis was similarly summarized in a memo sent to FRX-L personnel and is included in Appendix H of this report.

In brief, both design concepts center upon using a PFN architecture for the banks. In the Bias bank concept the Theta coil would be the load for the PFN, and other than needing to make appropriate voltage stand-off provisions to prevent the Main bank voltage from flashing over the Bias bank bus work the design appears quite feasible. The second design concept initially called for using the Guide and Mirror coils as the stage inductances in the PFN. Subsequent analyses revealed an inherent problem with this concept in that the currents are not uniform in all of the inductors in a PFN; thus the Guide magnetic field would not be uniform along the FRC translation region unless other special provisions were made. As was mentioned in Section 2.6, FRX-L project manager Dr. Tom Intrator has commissioned two other LANL personnel, Mr. Robin Gribble and Mr. William Reass, to explore other possible pulsed power driver design variations for the Guide and Mirror field coils, and we will likely make use of their design efforts when building up the FTX Guide and Mirror banks.

4.0 PUBLICATIONS AND PRESENTATIONS

During the period of performance on Task Order 36, SAIC personnel have had the opportunity to give a couple of presentations and prepare one conference paper describing the work related to the MTF-FRC project. The first presentation was given at the 15th IEEE International Pulsed Power Conference, which was held in Monterey, CA June 14-17, 2005. The presentation given there was a poster describing the proposed design, progress, and goals for the AFRL FTX/F-LINCX experiment. There seemed to be a fair level of interest in this project at the conference, not only because of the pulsed power systems that were described in the presentation, but also because of the plasma physics areas (FRCs and fusion energy) in which we are working. The conference paper was submitted at this time, as well, and will appear in the published proceedings from the conference.

The second presentation was again a poster presentation and was given more recently at the 2006 Innovative Confinement Concepts Workshop held in Austin, Texas February 13-15. The presentation given at this meeting was somewhat similar to that prepared for the Pulsed Power Conference in that its primary focus was the design of the AFRL FTX experiment and its proposed integration with the Shiva bank for FRC compression-heating (F-LINCX) experiments. The slides, however, had been updated to reflect the present status of both the design efforts and the hardware assembly, and several photos showing the new hardware in the Building 322 bay were added.

5.0 SUMMARY OF PRESENT WORK AND FUTURE PLANS

In closing, the efforts of SAIC and its sub-contractors, NumerEx and FabTek, Inc., under Task Order 36 have covered a wide range of areas related to the MTF-FRC research programs at both LANL's FRX-L facility and at AFRL's Building 322. A significant portion of the FTX experimental hardware has been designed now, and a smaller yet still significant portion has been fabricated and/or assembled in the Building 322 high bay. Two Z-pinch deformable contact liner-on-vacuum validation experiments were performed, both of which yielded extremely promising results. Such a liner configuration was found to implode very uniformly and should be able to adequately compress an FRC in our proposed compression-heating experiments. Design, fabrication, and assembly of an improved FRX-L Main bank Crowbar switch was also accomplished, and tests with the switch have shown that it performs extremely well with a dramatically reduced amplitude modulation being induced on the crowbarred Theta coil current waveform.

There is still much work to be done, however, and this will be the focus of the work performed on the new MTF-FRC Task Order under the DETAR contract. This work includes starting the initial FTX pulsed power tests within the next several weeks at AFRL, as soon as diagnostic and fiber optic trigger lines can be set in place. Design work on the support framework for the vacuum stand, as well as procurement of components for the vacuum system itself, will begin very soon, along with assembly of the control system. As work in these areas progresses, efforts to complete the assembly of the Bias and PI banks will then be accelerated so that FRC formation experiments can begin as soon as the vacuum system comes on line. The design and layout of the magnetic field coils needed for FRC translation are already being considered by FRX-L personnel (with AFRL and SAIC personnel assisting), and similar coils and the necessary banks to drive them must eventually be fielded on FTX, as well. Ultimately, we hope to perform several FRC compression-heating experiments with the Shiva Star bank by the end of the period of performance for this next Task Order, demonstrating that we can achieve MTF-relevant plasma densities ($n \sim 10^{19} \text{ cm}^{-3}$) and temperatures ($T \sim \text{several keV}$) in such experiments.

With regard to the FRX-L Crowbar switch, while the switch itself has been observed to perform well, unfortunately the triggering problems experienced by the first Crowbar switch still remain, and in some respects these problems are affecting the performance of the new switch more severely. As has been noted, the triggering problem must be resolved so that the "stationary" FRC characterization studies at FRX-L do not continue to be hindered. The addition of the slotted bus work on the Crowbar switch should help to mitigate this problem, but if it is not sufficient or if problems persist despite the new bus work, the ideas suggested at the end of Section 4.1.6 can be explored, and imminent tests with the FTX Main bank and Crowbar switch can also be used to help address this problem. In addition, efforts can be shifted toward beginning FRC translation studies more quickly, at which point the performance of the Crowbar switch and its trigger system may no longer be a concern because the FRC will be promptly leaving the Theta coil region after its formation. SAIC personnel will continue to help with the design work on FRX-L translation setup, as needed, and will also continue to support the FRX-L work in the areas of operations, diagnostic setup, maintenance, and system troubleshooting.

APPENDIX A. INVENTORY OF HARDWARE AVAILABLE FOR THE AFRL FRC FORMATION AND TRANSLATION EXPERIMENT

System	Los Alamos has on FRX-L	We have in-house	We will need to borrow/buy/fabricate
<i>Bias Bank</i>	Four 500- μ F, 10-kV capacitors Bus hardware, w/ cable header Two Class-D (?) ignitrons One NorthStar Ignitron trigger unit -10kV Spellman power supply Jennings switch for soft dump Jennings switch for charging Four pneumatic switches for hard short Several μ H inductor for bank isolation RG-214 (?) cables, bank to inductor ~Twelve RG-17/14 cables, inductor to theta coil header	Two modules of fifteen 170 μ F, 10-kV capacitors Some bus hardware RG-214 cable RG-17/14 cable	Cable header Ignitrons Ignitron trigger unit(s) 10-kV power supply Jennings switches Pneumatic switches (or Ross relays) Several μ H inductor for bank isolation More RG-214 cable
<i>Cusp Bank</i>	From two to sixteen 500- μ F, 10-kV capacitors Bus hardware, w/ cable header From one to eight Class-D (?) ignitrons One LANL-developed Ignitron trigger unit 10-kV Peter-Dahl power supply Jennings switch for soft dump Jennings switch for charging ___ pneumatic switches for hard short RG-214 (?) cables, bank to Cusp coils (two cables for each pair of capacitors)	One module of fifteen 170 μ F, 10-kV capacitors Some bus hardware RG-214 cable	Cable header Ignitrons Ignitron trigger unit(s) 10-kV power supply Jennings switches Pneumatic switches (or Ross relays) More RG-214 cable
<i>Guide Coil Bank</i>	(Not assembled yet)	One module of fifteen 170 μ F, 10-kV capacitors Some bus hardware RG-214 cable	Cable header Ignitrons Ignitron trigger unit(s) 10-kV power supply Jennings switches Pneumatic switches (or Ross relays) More RG-214 cable
<i>Translation-End Mirror Bank</i>	(Not assembled yet)	Thirty+ 170 μ F, 10-kV capacitors in storage RG-214 cable	Bus hardware and cable header Ignitrons Ignitron trigger unit(s) 10-kV power supply Jennings switches Pneumatic switches (or Ross relays) More RG-214 cable
<i>PI Bank</i>	Two 1.35- μ F, 100-kV capacitors Bus hardware, w/ cable header One Atlas-style rail-gap switch Trigger board and components for rail gap One 40' RG-218 trigger cable Maxwell 40151-B 100-kV trigger generator Maxwell 40168 50-kV trigger generator Length of RG-214 from 40168 to 40151 Length of 6-conductor cable from 40168 to 40151 +70kV Spellman power supply Jennings switch for soft dump Jennings switch for charging One (or two) pneumatic switches for hard short ~Twelve RG-17/14 cables, bank to theta coil header	A number of 1.35- μ F and 2.1- μ F, 100-kV capacitors One Atlas-style rail-gap switch w/ vertical flashguard Trigger board components RG-218 cable One Shiva-style trigger unit and one 100-kV UV power supply available (supply condition unknown) Brand new 40168 available RG-214 cable RG-17/14 cable	Bus hardware, w/ cable header Trigger board (acrylic) Controller for UV power supply More RG-214 cable 60-80 kV power supply Jennings switches Pneumatic switches (or Ross relays)

APPENDIX B. PRELIMINARY LIST OF CONTROL AND STATUS SIGNAL LINES REQUIRED BY THE FTX CONTROL SYSTEM

AFRL MTF Control System Details

Digital Outputs from Control System

Channel Number	Signal Name	Signal Type
1	Main bank ground lift	air signal line
2	Main bank hard short	air signal line
3	Main bank dump switch	air signal line
4	Main bank +/- charge switch	air signal line
5	Main bank contactor (start charge)	air signal line
6	Main bank charge cable ground lift	air signal line
7	Main bank trigger HV	air signal line
8	Main bank rail gap flush enable	air signal line
9	Crowbar trigger HV	air signal line
10	Crowbar rail gap flush enable	air signal line
11	PI bank ground lift	air signal line
12	PI bank hard short	air signal line
13	PI bank dump switch	air signal line
14	PI Spellman S3 (Control power on)	air signal line
15	PI Spellman S1 (HV enable) and charge switch	air signal line
16	PI Spellman HV on (S2)	air signal line
17	PI bank charge cable ground lift	air signal line
18	PI bank trigger HV	air signal line
19	PI bank rail gap flush enable	air signal line
20	Rail gap flush command	air signal line
21	Bias bank ground lift	air signal line
22	Bias bank hard short	air signal line
23	Bias bank dump switch	air signal line
24	Bias CCDS remot control power on (DB25-8)	air signal line
25	Bias CCDS HV enable (DB25-7) and charge switch	air signal line
26	Bias CCDS HV on (DB25-4)	air signal line
27	Bias bank charge cable ground lift	air signal line
28	Bias bank trigger HV	air signal line
29	Cusp bank ground lift	air signal line
30	Cusp bank hard short	air signal line
31	Cusp bank dump switch	air signal line
32	Cusp bank charge switch	air signal line
33	Cusp bank charge cable ground lift	air signal line
34	Cusp bank trigger HV	air signal line

Digital Outputs from Control System (Cont.)

Channel Number	Signal Name	Signal Type
35	Guide bank ground lift	air signal line
36	Guide bank hard short	air signal line
37	Guide bank dump switch	air signal line
38	Guide bank charge switch	air signal line
39	Guide bank charge cable ground lift	air signal line
40	Guide bank trigger HV	air signal line
41	Mirror bank ground lift	air signal line
42	Mirror bank hard short	air signal line
43	Mirror bank dump switch	air signal line
44	Mirror bank charge switch	air signal line
45	Mirror bank charge cable ground lift	air signal line
46	Mirror bank trigger HV	air signal line
47	Peter-Dahl contractor (charge Cusp, Guide, and/or Mirror)	air signal line
48	Command trigger	air signal line
49	Close gate valve	air signal line

Digital Inputs to Control System

Channel Number	Signal Name	Signal Type
1	North personnel door	copper line
2	East bay double doors	copper line
3	South sliding door	copper line
4	South personnel double doors	copper line
5	West sliding door	copper line
6	Shiva scram-shorting stick interlock chain	copper line

Analog Inputs to Control System

Channel Number	Signal Name	Signal Type
1	Main bank positive charge voltage	fiber optic V-to-F
2	Main bank negative charge voltage	fiber optic V-to-F
3	PI bank charge voltage	fiber optic V-to-F
4	Bias bank charge voltage	fiber optic V-to-F
5	Cusp bank charge voltage	fiber optic V-to-F
6	Guide bank charge voltage	fiber optic V-to-F
7	Mirror bank charge voltage	fiber optic V-to-F

APPENDIX C. PULSED POWER DIAGNOSTICS AND TRIGGERS REQUIRED FOR FTX

Table C.1. Pulsed Power Diagnostics for the FTX banks and Theta coil.

<u>Bank/Component</u>	<u>Diagnostic List</u>	<u>Scope Channels</u>
Main Bank	<ul style="list-style-type: none"> Rogowski coil to measure total bank current Trigger Monitor (small Rogowski) on at least one trigger cable 	3
Crowbar Switch	<ul style="list-style-type: none"> Planar triode Sync Out Rogowski coil for each crowbar rail gap (4 total) Trigger Monitor (small Rogowski) on at least one trigger cable Voltage monitor across crowbar (CVR and Pearson) Fiber optic array to view gap channeling 40168 Sync Out 	7
Theta Coil Assembly	<ul style="list-style-type: none"> 2 Rogowski coils, CW and CCW, to measure current into coils Faraday rotation diagnostic (2 channels) Voltage monitor, capacitive or resistive 	5
Pre-Ionization (PI) Bank	<ul style="list-style-type: none"> Rogowski coil to measure bank current Trigger Monitor (small Rogowski) on trigger cable Voltage monitor at cable header (?) 40168 Sync Out 	4
Bias Bank	<ul style="list-style-type: none"> Pearson or Rogowski coil to measure bank current Voltage monitor between bank and isolation inductor (?) 	2
Cusp Bank	<ul style="list-style-type: none"> Pearson or Rogowski coil to measure bank current 	1
Guide Bank	<ul style="list-style-type: none"> Pearson or Rogowski coil to measure bank current 	1
Mirror Bank	<ul style="list-style-type: none"> Pearson or Rogowski coil to measure bank current 	1

Up to 24 data channels are estimated for the FRC formation and translation experiment (FTX). For initial tests with the Main bank, Crowbar switch, and Theta coils, 15 data channels will be recorded (shown in red).

Table C.2. FTX triggers and possible delay generator channels.

Main bank	Possible diagnostics:
Crowbar switch	
Pre-Ionization (PI) bank	OMA(s)
Bias bank	Spectrometer(s)
Cusp bank	Framing camera(s)
Guide bank	Others?
Mirror bank	Screen room scopes

Triggers for initial tests are shown in red.

APPENDIX D. SLIDE SUMMARY DESCRIBING THE CHANGES MADE IN THE NEW FRX-L CROWBAR SWITCH DESIGN

Summary of Changes to FRX-L Crowbar Switch

10 Jan 2005 1

Original Crowbar Switch Tested With 40 nH Load

- Anticipated Theta Coil L was 36 nH
- Modulation Observed During Testing was +/- ~21%

Module Voltage = 80 kV; Crowbar Delay 1.8 μ s;
Load Inductance ~ 40 nH

Current (A) Millions

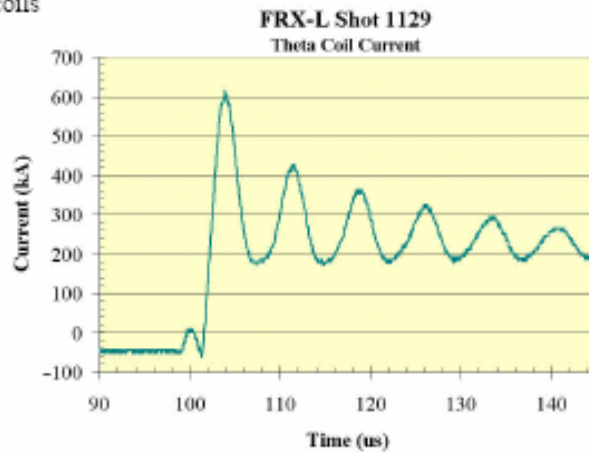
Time (μ s)

Legend: Main Bank Current, Crowbar Current, Theta Coil Current

10 Jan 2005 2

Modulation Observed on FRX-L Was Much Greater

- Actual Theta Coil Inductance was closer to 24 nH
- This increased, but only to ~31 nH, as flux excluder plates were moved away from coils



10 Jan 2005

3

Inductance in Crowbar switch comes from two sources:

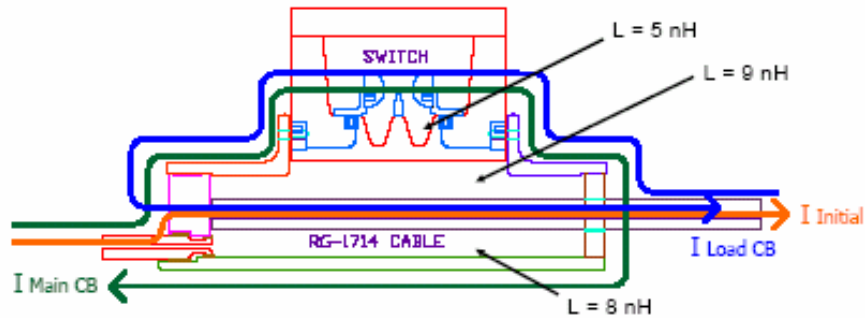
- Volume enclosed by current path
- "Quality" of multi-channeling in rail-gap switches

10 Jan 2005

4

Current Paths in Original Crowbar Switch

Inductances due to volume are:

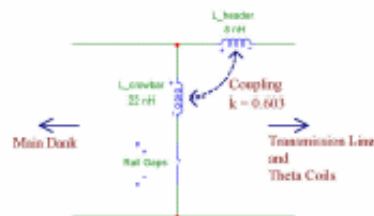


Total of 22 nH in crowbarred Main bank loop; 14 nH in Theta coil loop. The Theta coil loop inductance is shared by the Main bank loop → the two loops are coupled.

10 Jan 2005

5

Equivalent Circuit:



- Current in Main Bank loop induces voltage across crowbar switch ($V = L \, dI/dt$)
- Crowbar inductance comparable to transmission line and theta coil inductance
- Induced voltage from Main bank is able to significantly modulate theta coil current

10 Jan 2005

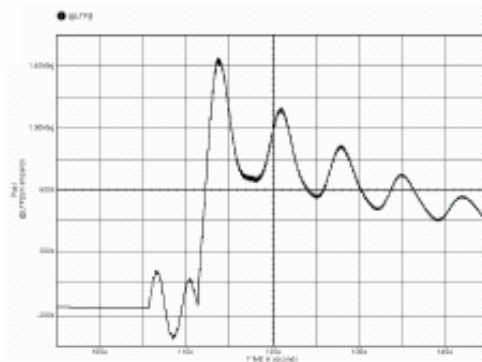
Calculated Theta Coil Current:

Main bank +/- 35 kV, trig @ 116.45 μ s

Bias bank - 7 kV, trig @ 0

PI bank + 53 kV, trig @ 110.8 μ s

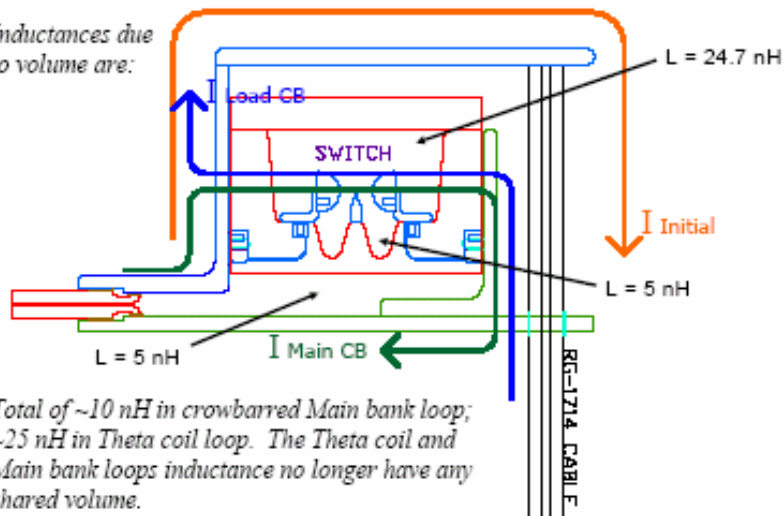
Crowbar, trig @ 119.2 μ s



6

Current Paths in New Crowbar Switch

Inductances due to volume are:

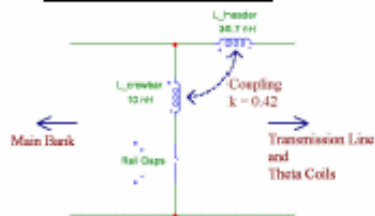


Total of ~10 nH in crowbarred Main bank loop; ~25 nH in Theta coil loop. The Theta coil and Main bank loops inductance no longer have any shared volume.

10 Jan 2005

7

Equivalent Circuit:



- Current in Main Bank loop still induces voltage across crowbar switch ($V = L \, dI/dt$)
- Crowbar inductance now significantly less than transmission line and theta coil inductance
- Induced voltage from Main bank has minimal effect on theta coil current waveshape

10 Jan 2005

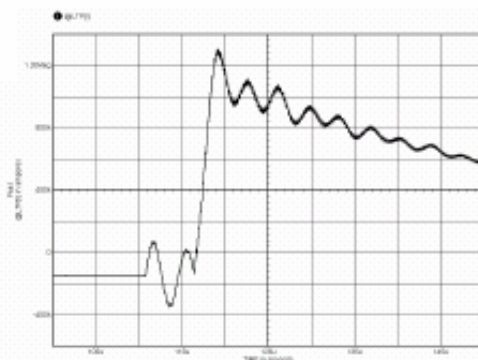
Calculated Theta Coil Current:

Main bank +/- 35 kV, trig @ 116.45 μ s

Bias bank - 7 kV, trig @ 0

PI bank + 53 kV, trig @ 110.8 μ s

Crowbar, trig @ 119.2 μ s



8

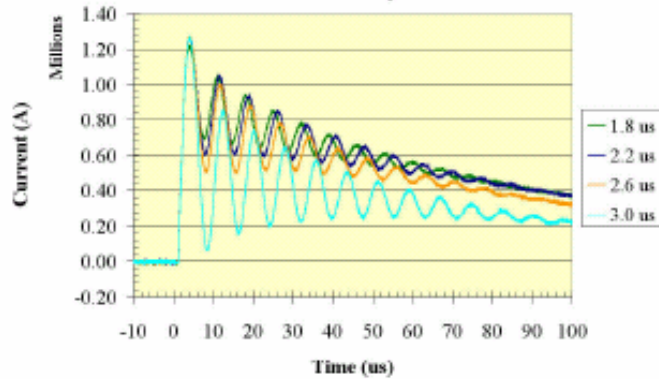
* Note that even though there are no shared volumes between the Main bank and Theta coil loops, the current path through the rail gaps is not a uniform sheet. Thus, there will still be some coupling. J. Parker, who has performed these circuit simulations, has tried to include the effects of this coupling in the simulations (the $k = 0.42$).

10 Jan 2005

9

“Quality” of Multi-Channeling in Crowbar Rail Gaps Also Affects Switch Inductance

Load Current Waveforms For Different Main-to-Crowbar Delays



10 Jan 2005

10

In the tests above, the crowbar was triggered at varying times before current peak (at $\sim 2.9 \mu\text{s}$) \Rightarrow

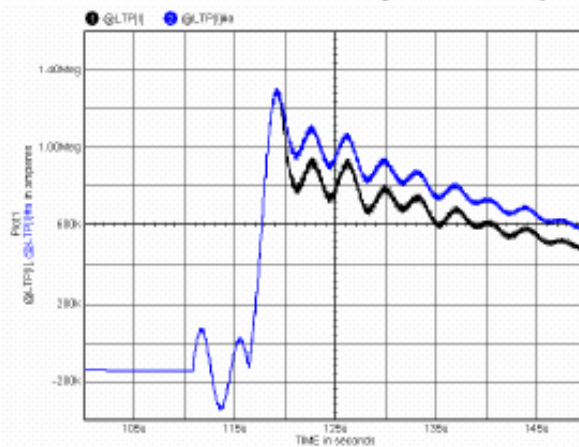
- Modulation increased as trigger time approached current maximum
- Voltage across rail gaps also decreased, of course, closer to current maximum
- Multi-channeling was likely poorer with trigger at lower voltages

10 Jan 2005

11

Modeling of FRX-L With New Crowbar Switch

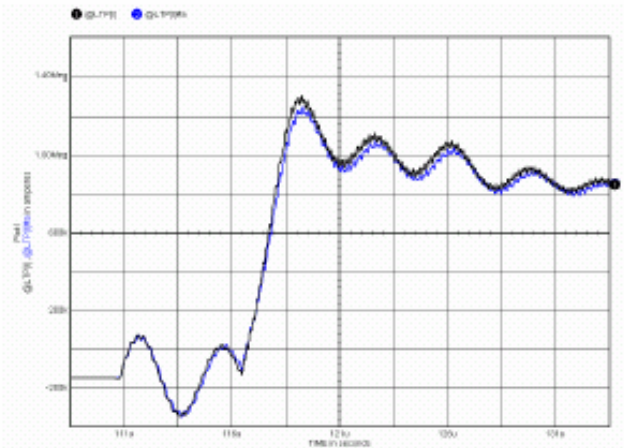
- Crowbar triggered at t_{cb} (black) versus $t_{cb} + 1 \mu\text{s}$ (blue)
- \Rightarrow Mean current decreases but modulation amplitude relatively unchanged



10 Jan 2005

12

- Theta coil inductance 24 nH (black) versus 31 nH (blue)
- ⇒ Modulation amplitude relatively unchanged



10 Jan 2005

13

The circuit simulation plots above suggest that because of

- the increase in the inductance downstream from the crowbar switch and
- the elimination of all shared volumes (coupled inductances) between the Main bank and Theta coil current loops,

the new crowbar switch is more insensitive to changes in Theta coil inductance and the effects of the quality of the multi-channeling in the rail gaps.

10 Jan 2005

14

APPENDIX E. ANALYSIS FOR ESTABLISHING BETTER ISOLATION AND/OR BETTER TRIGGERING BETWEEN THE FRX-L CROWBAR RAIL GAPS

E.1 DESCRIPTION OF THE PROBLEM

Though the performance of the new Crowbar switch has been exceptional in terms of the improved current waveform in the Theta coil load, it still suffers from the triggering problems that the old Crowbar switch had, as well as an increased level of difficulty in initiating current conduction in all four rail-gap switches; that is, quite often only three of the four rail-gap switches will conduct during a given FRX-L shot. The rail gap that fails to conduct varies with each cleaning cycle and often with each shot. If a particular switch is persistently not conducting during shots re-cleaning the rail gaps will help it to begin conducting again, but often another rail-gap switch will then fail to conduct. Prior to decreasing the gap spacing of the inner two switches in the quad assembly, it would typically be gap #2 or #3 (the inner two rail gaps in the assembly) that would fail to conduct current; now any of the four seems to have an equal likelihood of not conducting.

We know that the voltage across the Crowbar switch is low when it is triggered. The triggering problem that affected to old Crowbar switch also appears to be present with this new switch, and prevents it from being reliably triggered at earlier times when the voltage would be higher. We also know from trigger monitors and Crowbar Rogowski coils that there is a significant delay (100's nanoseconds to microseconds) between when the Crowbar is triggered and when the rail gaps actually begin conducting current.

It has been suggested that the reason a given rail gap may fail to conduct is because its neighbors start conducting slightly earlier, causing the voltage to collapse completely across the non-conducting rail gap and thereby preventing it from ever starting conduction. This memo looks at slotting the hot bus plates of the Crowbar switch to provide a margin of inductive isolation between the individual rail gaps. A possible scheme for increasing the amplitude of the trigger pulse to initiate the breakdown in each rail-gap switch more quickly (and therefore more reliably) is also discussed. Having a higher trigger voltage may help to compensate for the low voltages at which the Crowbar switch is operating.

E.2 SLOTTING OF BUS PLATES

Main Bank Closing Switch Geometry – There have rarely been any difficulties with getting the rail gaps in the Main bank closing switch to conduct. Of course, there is the full Main bank voltage across them when they are triggered, but the upper and lower hot bus plates also have separate tabs which extend toward the switch to make contact with the rail gaps (Fig. E1). It is likely that the plate is contoured the way it is to gradually direct current from the upper and lower modules into the switch, however the resulting cutouts between the rail gaps may also serve to inductively isolate the individual rail gaps. The inductive isolation then slows the time it takes for the voltage collapse across one rail-gap switch to be “noticed” by its neighbors.

To attempt to quantify the level of isolation, a calculation was made of how quickly a wave (that of the collapsing voltage across one of the rail gaps) would propagate to an adjacent rail gap. The shortest path between the rail gaps is along the edge of the cutout, as shown in Fig. E1.

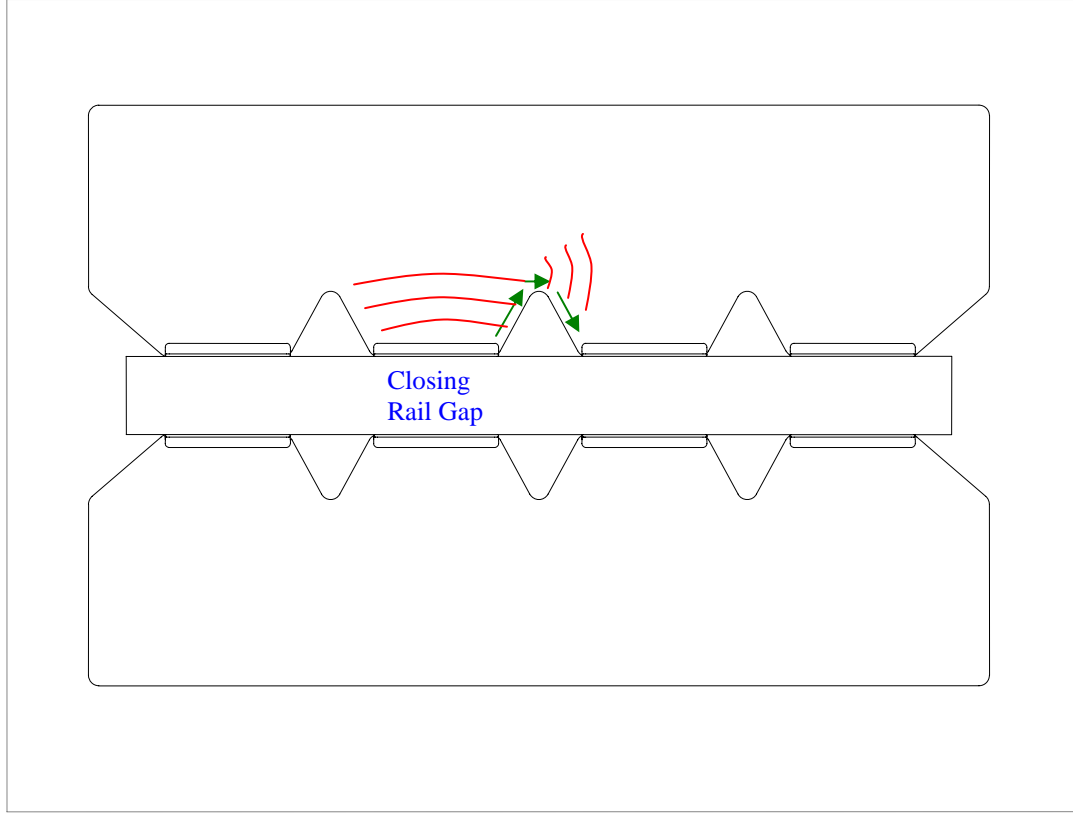


Figure E1. Propagation of the voltage wave from a rail-gap switch after it closes.

Considering the hot and ground bus plates as a parallel plate transmission line, we have

$$L^* = \frac{\mu_o t}{w} \text{ [H/m]}, \quad (\text{E1})$$

$$C^* = \frac{\epsilon_o \epsilon_r w}{t} \text{ [F/m]}, \quad (\text{E2})$$

and

$$v = \frac{1}{\sqrt{L^* C^*}} \text{ [m/s]}, \quad (\text{E3})$$

where L^* is the inductance per unit length of the current channel along the edge of the cut-out, C^* is the capacitance per unit length of the channel, v is the velocity of the voltage wave propagation along the channel that forms, and w and t are the width and thickness of the channel. (Note that these equations may not be entirely accurate here because we are considering a narrow current channel and boundary conditions may thus play a more important role than they are being given.) Plugging Eqns. (E1) and (E2) into Eqn. (E3) we obtain

$$v = \frac{1}{\sqrt{\mu_o \epsilon_o \epsilon_r}}. \quad (\text{E4})$$

The dielectric constant ϵ_r of the Mylar between the plates is ~ 3.0 . Inserting this value and those for μ_o and ϵ_o into the equation, we find a propagation velocity of 1.731×10^8 m/s. The path length around the cutout is 16.15 in. or 0.41 m, so the propagation time is then 2.37 ns.

Present Crowbar Switch Geometry – A similar attempt is now made to look at the wave propagation between the crowbar rail gaps. Figure E2 shows a drawing of a side view of the crowbar switch, looking from the Main bank toward the crowbar (high voltage side) and load.

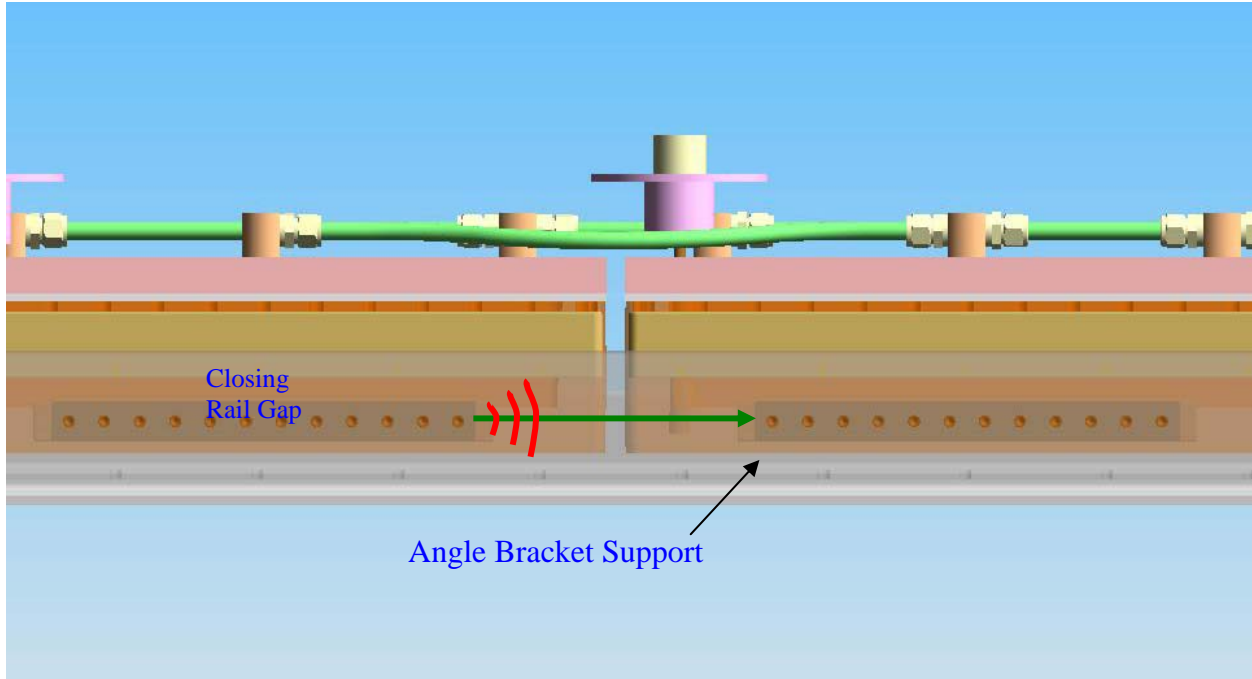


Figure E2. Propagation of the collapsing voltage wave between crowbar rail gaps. The view is from the Main bank looking toward the switch, and the angle bracket support has been made transparent so that the contacts on the rail gaps can be seen.

When one rail gap closes, the collapsing voltage wave has a straight line of propagation to the adjacent rail gaps. This distance is 7.875 in. or 0.20 m. The assumption is made that the width of the current channel is the same as the width of the rail gap contacts on their sides (1.125 in. or 0.029 m) and the thickness of the channel is the skin depth in aluminum. The quarter-cycle rise time of the current in the crowbar rail gaps, as observed from the crowbar Rogowski waveforms, is $\sim 2.69 \mu\text{s}$; the skin depth in aluminum should therefore be 0.010 in. or 2.62×10^{-4} m. Because of the complicated geometry, the parallel plate formula for inductance (Eqn. [E1]) is not used; rather we consider the inductance to be the sum of current channel inductance in the hot bus plate, the mirror current inductance in the ground bus work, and the mutual inductance between the two. The inductance of the current channel is calculated using the formula for a rectangular bar:

$$L = 0.00508 \ell \left(2.303 \text{Log}_{10} \left(\frac{2\ell}{w+t} \right) + 0.5 + 0.2235 \frac{w+t}{\ell} \right) [\mu\text{H}], \quad (\text{E5})$$

where w and t are the width and thickness of the current channel, respectively, and l is the length of the channel. This inductance turns out to be 126.5 nH or 632.5 nH/m. The mirror path on the ground side of the crowbar switch hardware is assumed to span the entire width of the ground hardware. Because of this width, it is also assumed then that the inductance will be much less than that of the channel on the hot side. Furthermore, because of the distance between the two, it is assumed that the coupling between the hot side and ground side channels is very low. With these assumptions in mind, the total inductance of the channel reduces to the 632.5 nH/m just calculated.

To calculate the capacitance associated with this current channel, the 2-D finite element analysis program Quick Field was used. A cross-sectional diagram of the crowbar switch is shown in Fig. E3; this drawing was imported into Quick Field, and the ground and high voltage regions were then defined as shown. Analogous to considering only the current in the channel between the rail gap contacts for the inductance calculation above, only the current channel region was defined to be at high voltage here. After building the mesh and running the electrostatic analysis routine, the program was then used to numerically calculate the capacitance (per unit length) associated with the channel. The value that was obtained from this calculation was 25 pF/m.

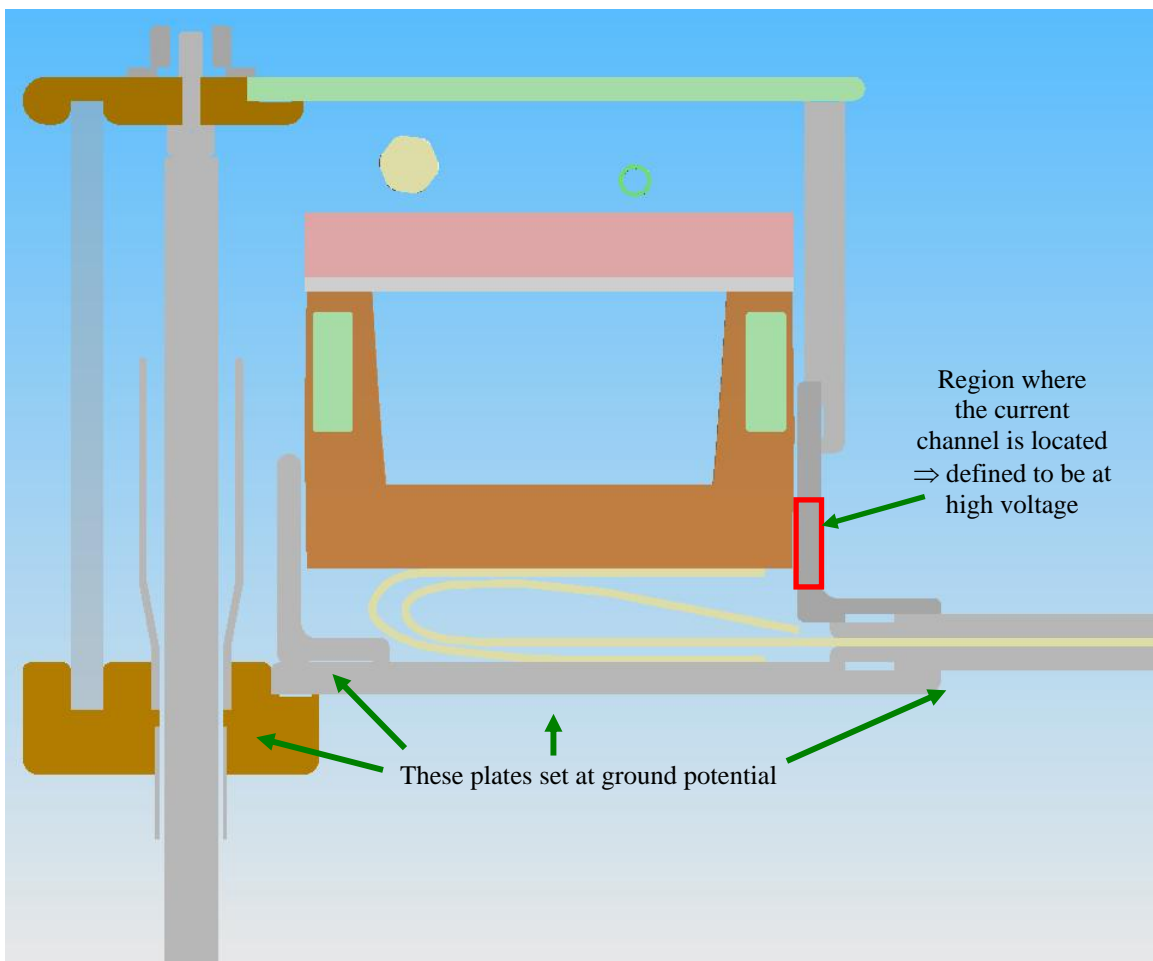


Figure E3. Cross-sectional view of crowbar geometry. Regions set at ground and at high voltage in the Quick Field electrostatic simulation are noted, as well.

Plugging the values for L^* and C^* calculated above into Eqn. (E3) a wave velocity of 2.515×10^8 m/s is obtained. By then dividing the spacing between the rail gaps (7.875 in or 0.2 m) by this velocity, a propagation time of only 0.795 ns is obtained, which is a factor of 3 shorter than the propagation time between the closing switch rail gaps.

Old Crowbar Switch Geometry – Interestingly, after a similar analysis was performed for the old crowbar switch geometry, a propagation velocity and time between adjacent rail gaps of 2.721×10^8 m/s and 0.735 ns, respectively, were obtained. These values are very close to those just calculated for our present switch geometry, yet we note that near the zero crossing of the Main bank voltage (where the crowbar switch is triggered) each of the crowbar rail gaps tended to operate very reliably. (It was only when the trigger delay time was moved away from the zero crossing that problems tended to occur.) It is possible that the higher inductance associated with the current flow through the old crowbar geometry helped to “slow” the closing of each of the rail gap switches, thereby ensuring that all four could in fact initiate sustainable arc channels and begin conducting before the voltage across them collapsed.

Slot Dimensions – To increase the degree of isolation of the crowbar rail gaps from each other, slots could possibly be machined into the hot bus plates. This will require the collapsing voltage wave to propagate a further distance in order to reach the contacts of an adjacent rail-gap switch (Fig. E4). In contrast to the bus plate cut-outs around the closing switch rail gaps, the slots here

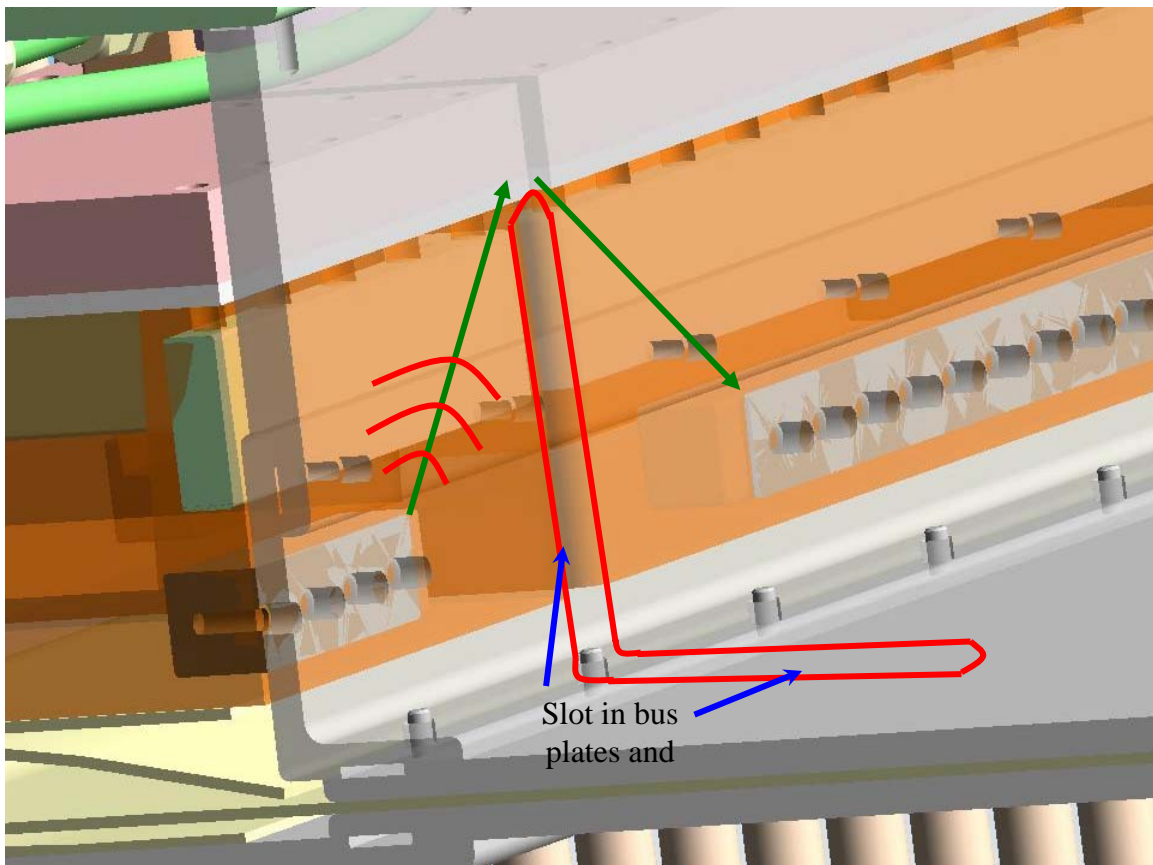


Figure E4. Illustration of how the collapsing voltage wave would have to propagate further to an adjacent rail gap if a slot were inserted into the bus plates and angle bracket.

should probably be fairly long and narrow to prevent perturbing the current flow from the Main bank as it travels past the crowbar switch and down to the load.

To estimate how long the slots should be we can take the propagation velocity for a wave propagating from a crowbar rail gap (2.515×10^8 m/s) and multiply it by a more lengthy transit time, say, the transit time estimated for the closing switch rail gaps (2.37 ns). This value would appear to be reasonable since, again, the closing switch has shown no signs of problems with triggering all four rail gaps. Performing this calculation, a path length of 0.596 m (23.47 in.) is then obtained. From geometry the slot then needs to extend up the bus plate and past the rail gap contacts by 11.05 in. (0.28 m). The slot also needs to extend down the angle bracket support and up the short transmission line towards the Main bank. Since the propagation velocity is the same in the transmission line as in the bus plates on the front of the bank (1.731×10^8 m/s), which is slower than in the crowbar switch region, the total slot length need not be quite as long upstream of the crowbar switch as it should be downstream of it. Nevertheless, it would appear that in both directions rather lengthy slots are required.

E.3 INCREASING TRIGGER PULSE AMPLITUDE

In addition to isolating the individual crowbar rail gaps in an attempt to provide more time for the trigger pulse in each to initiate sufficient arc channels to start conduction, we might also consider how to improve the production of the arc channels. Improved triggering combined with the slotted bus plates might lessen the constraints on the slots; that is, we could possibly get away with implementing a set of shorter slots. Shorter slots would hopefully reduce the machining work and therefore the down time for the experiment.

One obvious way to do improve the breakdown conditions in the rail gaps would be to increase the voltage of the trigger pulse delivered to the rail gaps. Fitch and Howell (R.A. Fitch and V.T.S. Howell, "Novel principle of transient high-voltage generation", Proceedings IEE, vol. 111, no.4, 1964, pp. 849-855.) describe a relatively simple method for obtaining high voltage pulses by "stacking" charged cables. Since we already use a charged-cable arrangement for triggering the crowbar rail gaps, implementing a scheme such as the one they describe in their Fig. 7 to, say, double the trigger pulse amplitude would only require adding a second charged cable to each rail gap plus any additional trigger board components needed to accommodate the higher pulsed voltage. The basic circuit diagram for the setup is shown in Fig. E5.

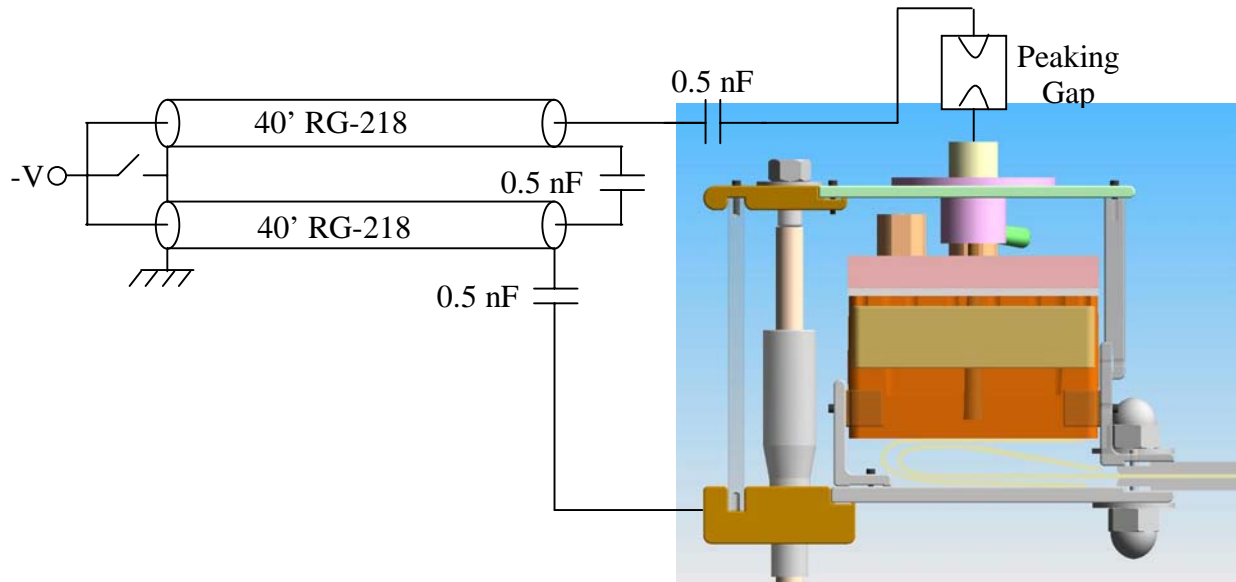


Figure E5. Sketch of trigger circuit with second trigger cable added to double the trigger pulse amplitude.

E.4 SUMMARY

Though there were a number of assumptions made in these analyses, they would seem to support the utility of inserting slots in the bus plates between the individual crowbar rail gaps to inductively isolate them. A longitudinal slot no more than, say, 0.5 in. (1.3 cm) in width that extends 11 in. (0.28 m) downstream and possibly shorter upstream of the rail gaps should in principle provide an equivalent isolation to that which is present for the Main bank closing switch. The slots could perhaps be made shorter if we can also apply a higher voltage trigger pulse to improve the arc initiation in the rail gaps. The triggering scheme, as shown in Fig. E5, is simple enough that we could implement it fairly quickly to verify its usefulness before beginning any work on cutting slots in the bus work.

APPENDIX F. ESTIMATES OF MUTUAL COUPLING BETWEEN SECTIONS OF THE SLOTTED CROWBAR SWITCH BUS WORK

F.1 PARALLEL PLATE TRANSMISSION LINE TO THE CROWBAR SWITCH

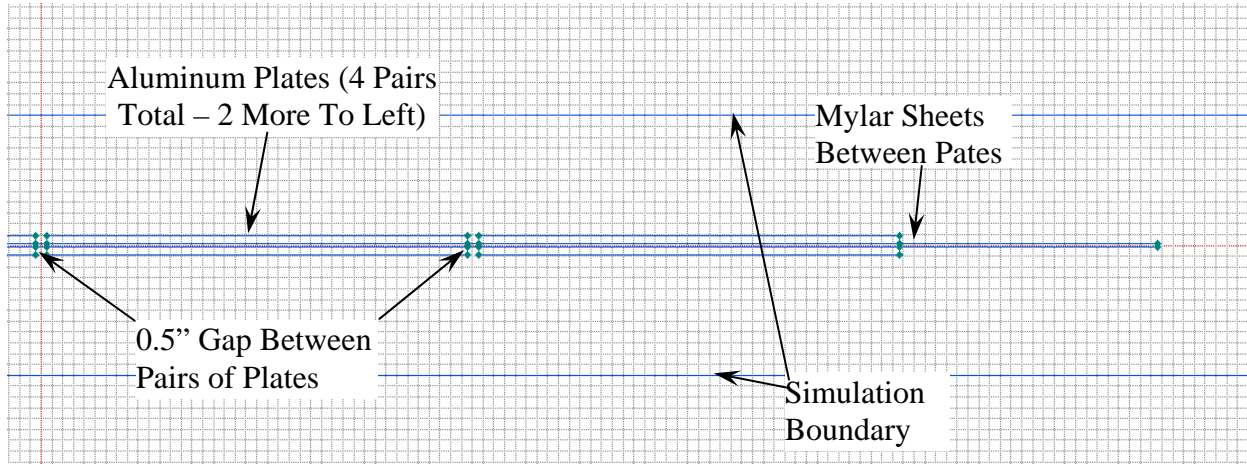
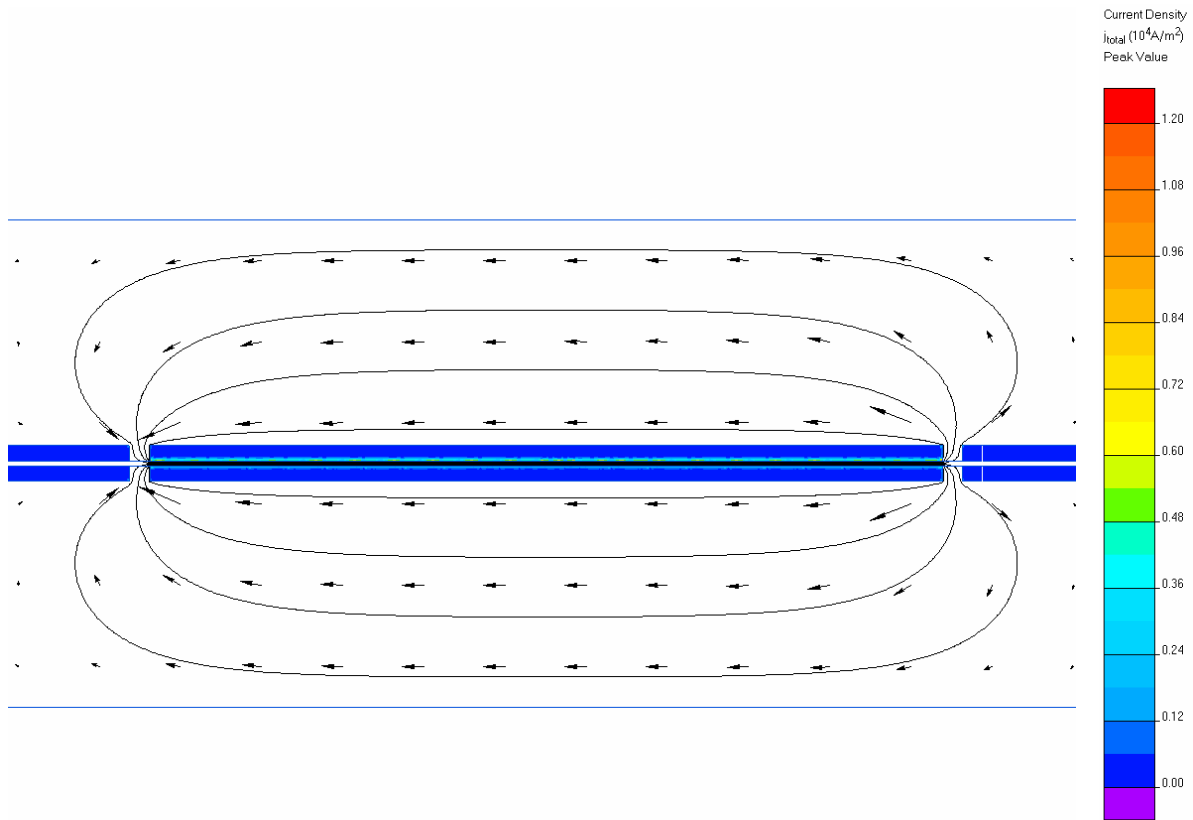


Figure F1. Layout of the Quick Field simulation for the transmission line feed on back of Main bank going to the Crowbar switch and cable header. 0.12'' of Mylar separate the upper plates from the lower plates. Between each upper-lower plate pair, there is the proposed 0.5''-wide slot in the bus plates.

Quick Field Time-Harmonic Magnetics Simulation:



- Amplitude of AC current in top aluminum plate is 1 A, -1 A in bottom plate. Frequency of AC current is 94.3 kHz (quarter rise time of 2.65 μ s, same as for FRX-L Main bank).
- Field lines at 0° phase, scale = 1e-9 V.
- Vector plot at 0° phase of flux density B, scale = 10,000,000.
- Peak current density shown in contours, scale as indicated to the right.

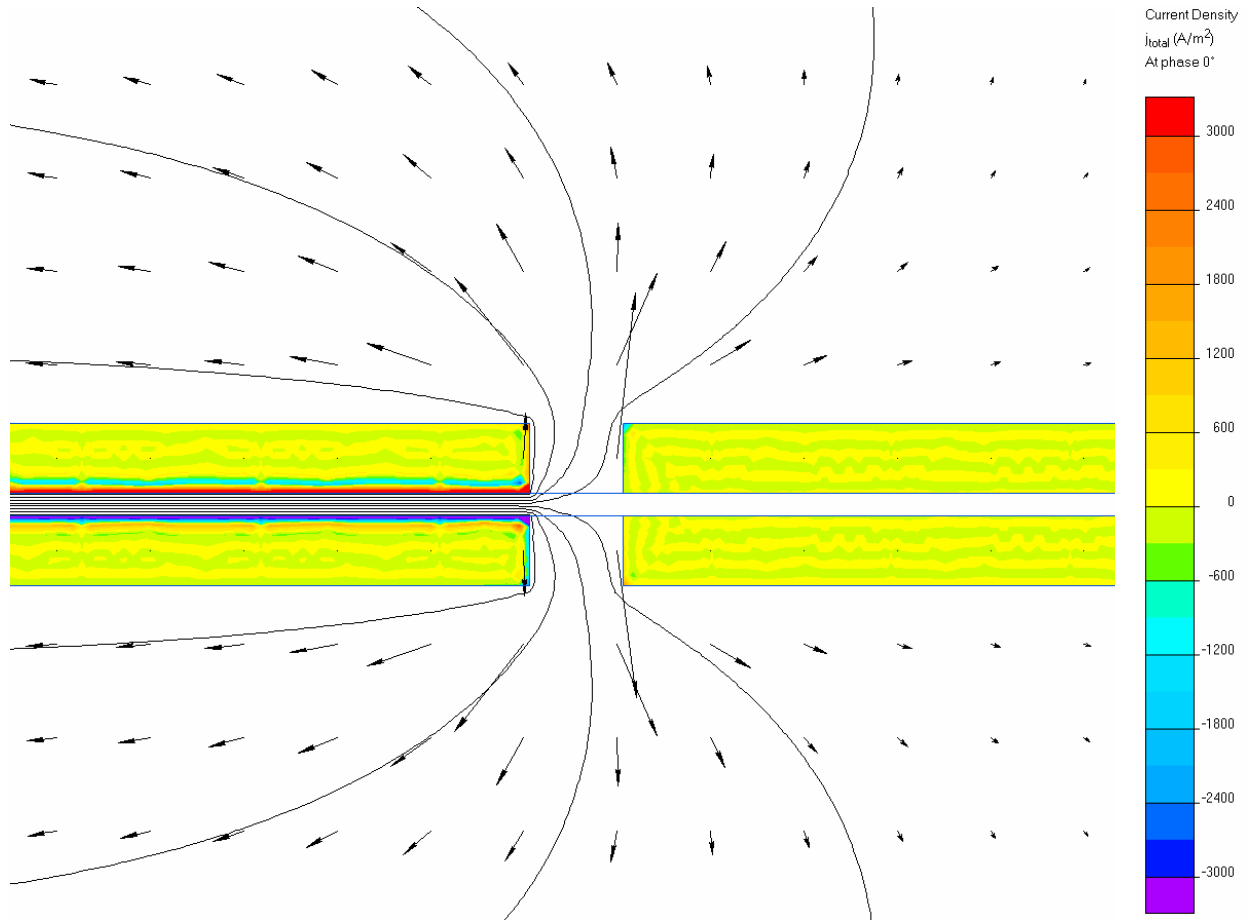


Figure F2. Close-up of right side of the two conducting plates – current density contours are now shown for 0° phase with the scaling as indicated to the right. Field line plot and vector plot scales are the same as above.

—→ Vector plots above, as well as the plots of the field lines, show that the magnetic field does not appear to couple to the adjacent pair plates on either side, so 0.5”-wide slot is sufficient to provide inductive isolation between the rail-gap switches.

F.2 VERTICAL BUS WORK CONNECTED TO THE CROWBAR RAIL GAPS

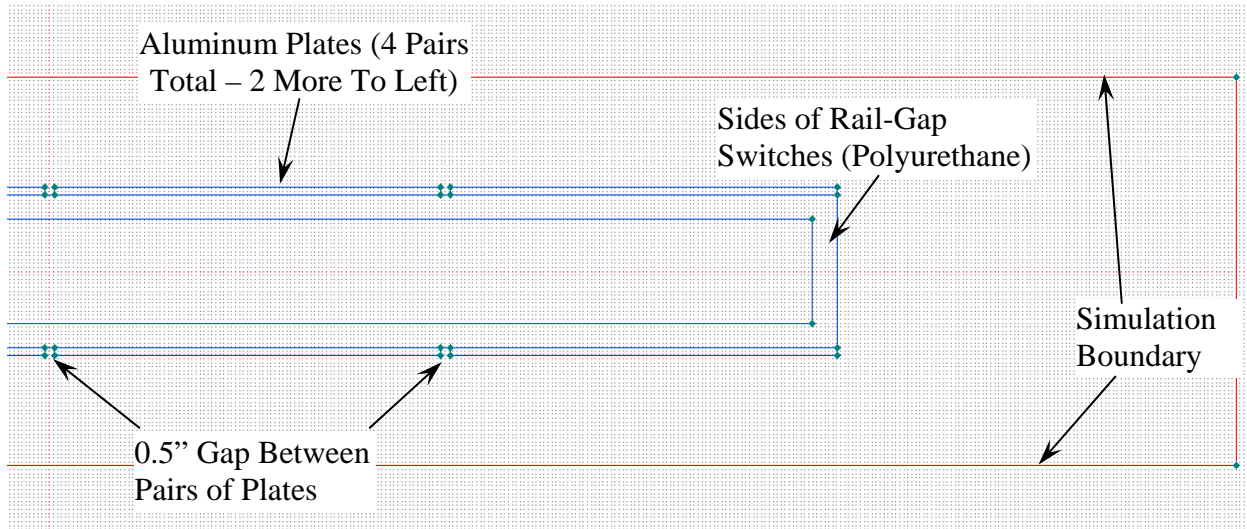
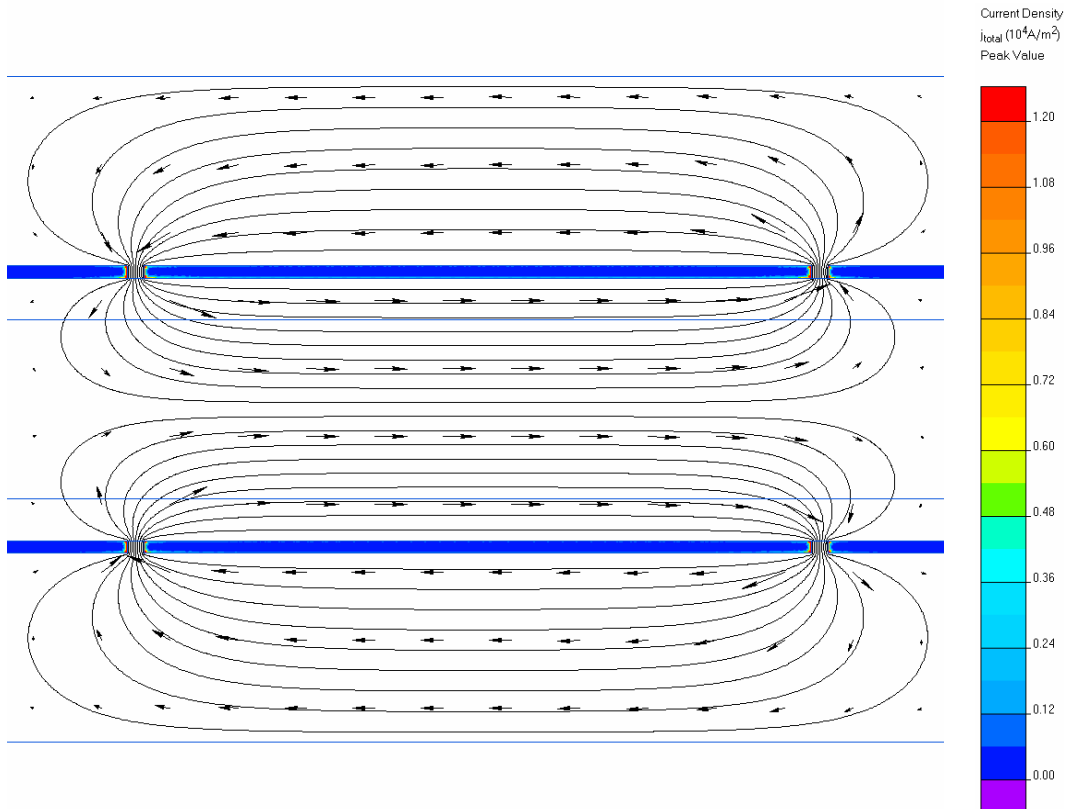


Figure F3. Layout of the Quick Field simulation for the bus plate and angle bracket that are bolted to each side of the Crowbar switch. 7.725" (the width of the rail-gap switches) separate the top angle bracket segments in the sketch from the bottom plate segments. Between each bracket-plate pair, there is the proposed 0.5"-wide slot. (A 0.5" wide slot is actually already present in the angle bracket because of the Rogowski coils.)

Quick Field Time-Harmonic Magnetics Simulation:



- As with the first simulation, the amplitudes of the AC currents in the top and bottom aluminum plates are 1 A and -1 A, respectively. Frequency of the AC current is 94.3 kHz (i.e., it has a quarter rise time of 2.65 μ s, same as for FRX-L Main bank).
- Field lines are at 0° phase, scale = 1e-8 V.
- Vector plot is at 0° phase of flux density B, scale = 500,000.
- Peak current density shown in contours, scale as indicated to the right.

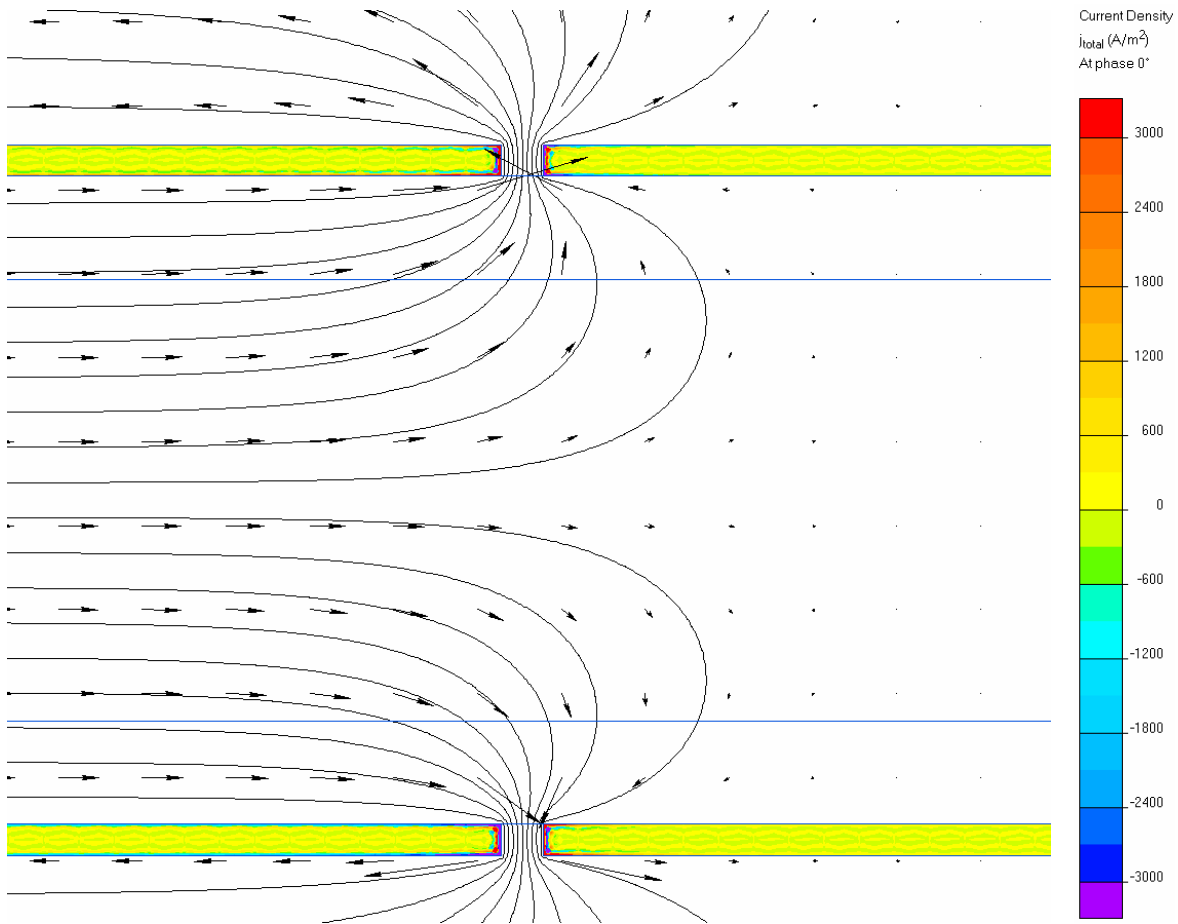


Figure F4. Close-up of right side of the two conducting plates – current density contours are now shown for 0° phase with the scaling as indicated to the right. Field line plot and vector plot scales are the same as above.

—→ As with the first simulation for the parallel plate transmission line leading to the Crowbar switch, the field does not appear to couple to adjacent pairs of plates here either, so 0.5”-wide slot is again sufficient to provide inductive isolation between the rail-gap switches.

APPENDIX G. TWO-STAGE PFN CONCEPT TO INCREASE BIAS CURRENT AND DECREASE BIAS PULSE DURATION

This memo describes several follow-up simulations of the FRX-L Bias bank concept discussed in a memo sent out by Dr. Tom Intrator on 15 May 2006. The simulations focus in particular on the voltages that might be induced on the Bias bank when the Main bank is triggered. A comparison between the new Bias bank concept, the present FRX-L Bias bank, and the AFRL Bias bank, which is similar in design to the present FRX-L Bias bank, is made at the end.

A generic MicroCap circuit model for the present FRX-L Main, PI, and Bias banks is shown below in Fig. G1. The crowbar switch parameters in the model also reflect those of the present switch configuration, while the switch closing times were taken from the FRX-L shot series in which the Main bank was triggered after the PI bank rang for one and a half cycles. Note that the net resistances of each bank circuit are incorporated into the switch element (third parameter following the “T”).

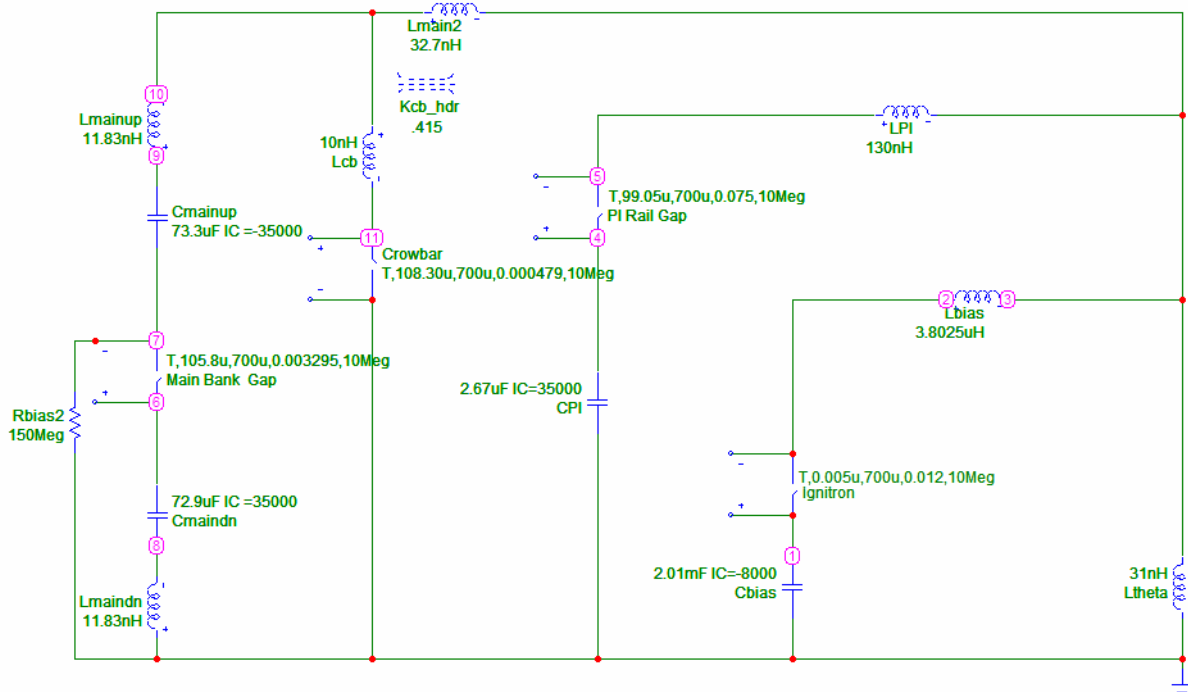


Figure G1. Lumped-element circuit model of the FRX-L experiment that has been entered into MicroCap.

Shown in Fig. G2 are several waveforms obtained after the circuit simulation was run. Currents (in MA) are shown in the top plot and voltages (in kV) in the bottom. We mainly want to note that when the Main bank is triggered only a slight change in Bias bank current, $I(C_{Bias})$ is observed in the top plot, and in the bottom plot little if any change in voltage is observed at the Bias bank ($V(C_{Bias})$), or at the node between the ignitron and the bias inductor ($V(2)$); the voltage is “dropped” primarily across the Bias inductor ($V(L_{Bias})$).

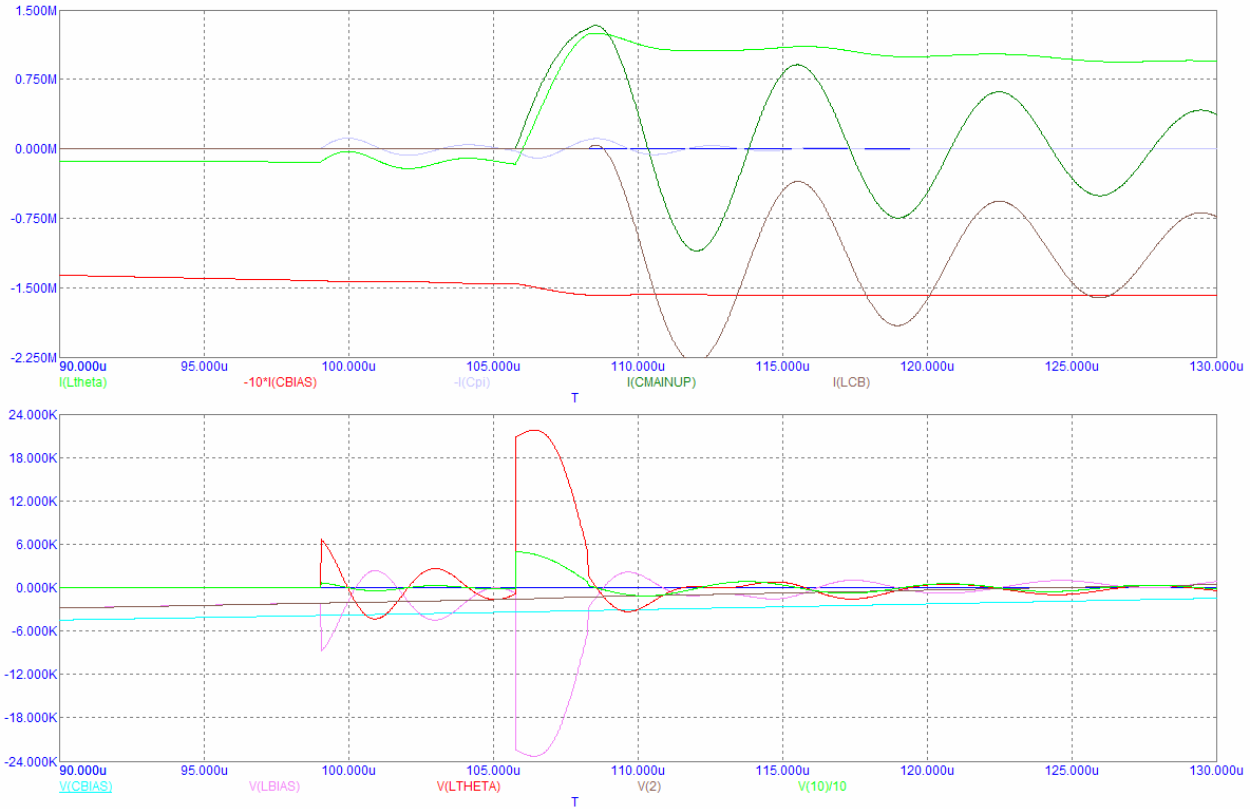


Figure G2. Current and voltage waveforms calculated by MicroCap using the FRX-L circuit model shown in Fig. G1.

Figure G3 shows the same waveforms for the condition when the Bias bank is not triggered. It can be seen that the node between the ignitron and the bias inductor, V(2), jumps up to 20+ kV when the Main bank is triggered, and in the experiment this usually results in an arc between the hot and ground bus plates on the bias bank.

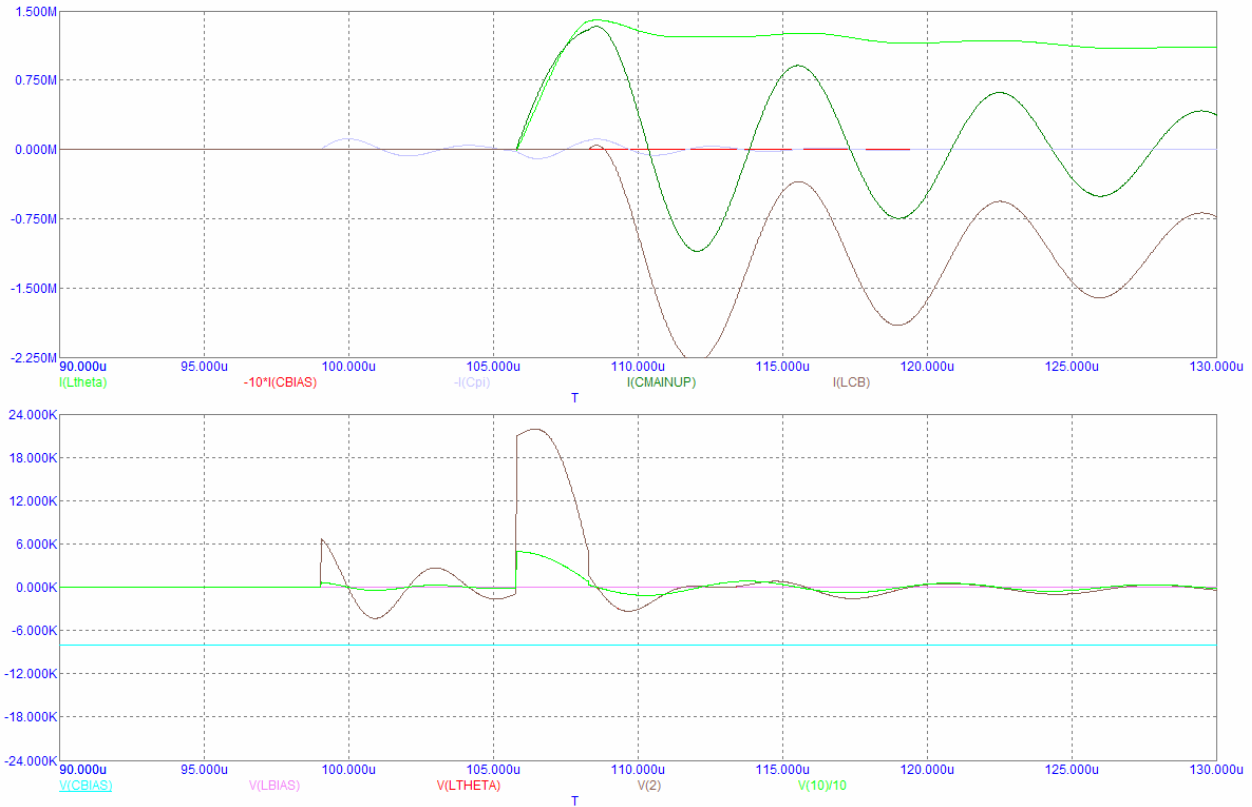


Figure G3. Current and voltage waveforms calculated by MicroCap for case when the Bias bank is not triggered.

Dr. Intrator’s Bias bank/PFN circuit model was entered into MicroCap next (Fig. G4) to verify that MicroCap was giving the same results that Dr. Intrator observed. The waveforms shown in Fig. G5 verify that the same results are indeed obtained.

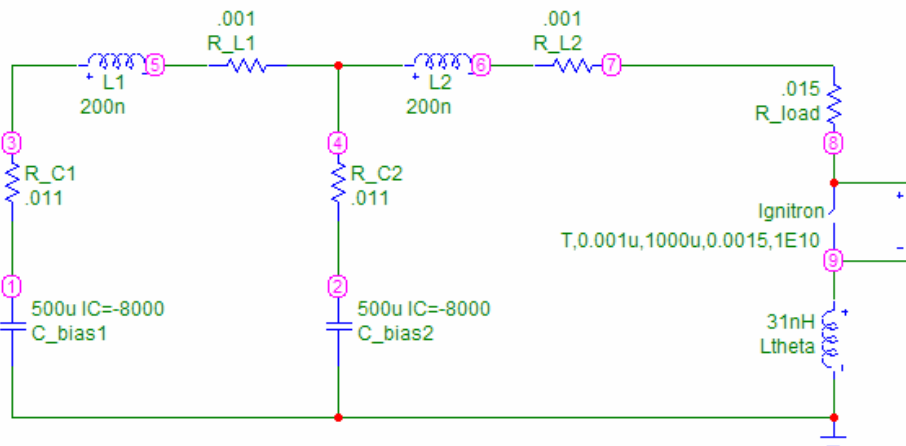


Figure G4. MicroCap circuit model of Dr. Intrator’s Bias bank/PFN concept.

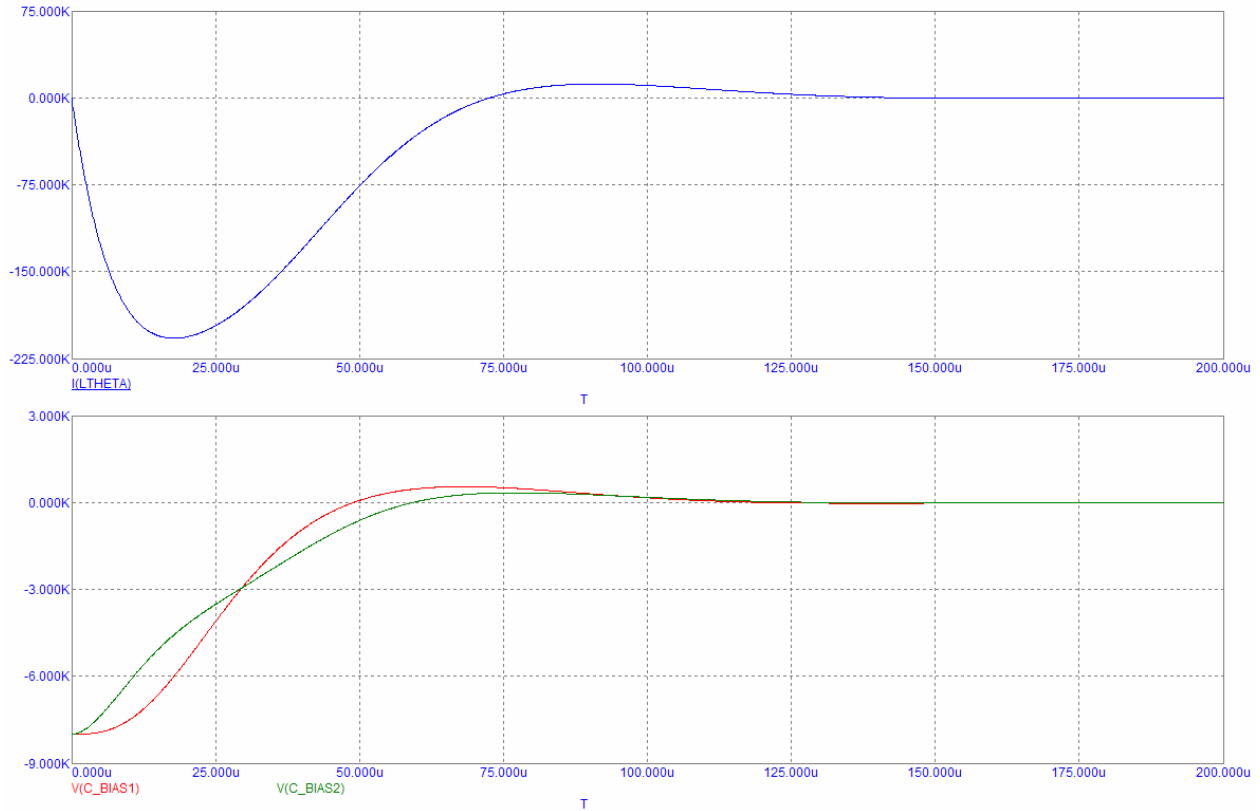


Figure G5. Current and voltage waveforms calculated by MicroCap using the circuit model shown in Fig. G4.

Next, the Bias bank/PFN circuit model was then incorporated into the FRX-L circuit shown in Fig. G1 in place of the Bias bank model that was currently there. The new model is shown in Fig. G6, and Fig. G7 shows a similar set waveforms, as were obtained from the previous FRX-L model (Fig. G2). The plot in Fig. G7, however, shows the voltages for each stage of the PFN, $V(C_Bias1)$ and $V(C_Bias2)$, and the total bank current is represented by $I(L2)$, which is the current through the inductor L2. We note that there is a greater change in the Bias bank current now when the Main bank is triggered (comparing with Fig. G2, the Bias bank current is scaled in that plot by a factor of 10 to make the changes more apparent).

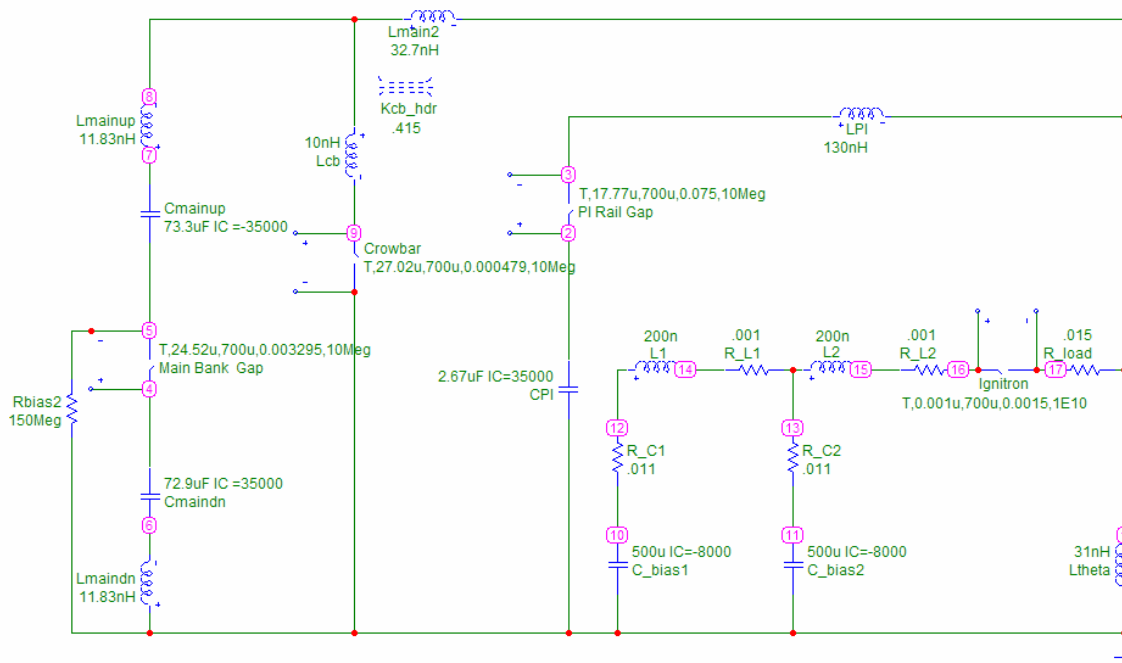


Figure G6. The lumped-element FRX-L circuit model is shown again but with the Bias PFN circuit in place of the original Bias circuit.

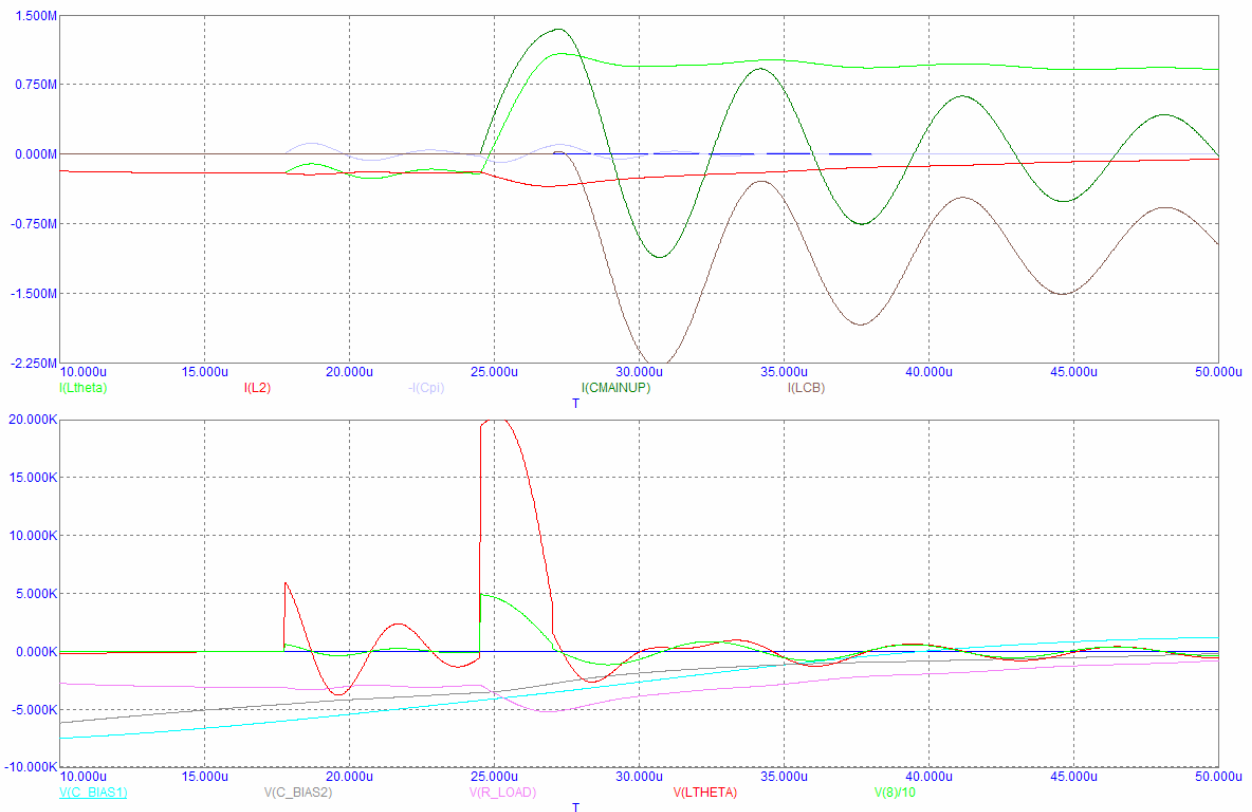


Figure G7. Current and voltage waveforms calculated by MicroCap using the circuit model shown above in Fig. G6.

Figure G8 shows a plot of the voltages at nodes 17, 13, and 12 indicated in the diagram in Fig. G6, which correspond to the voltage at the node between the load resistor and the ignitron and the nodes at the hot terminals of the stage 2 and stage 1 Bias bank capacitors, respectively. Comparing V(2) in Fig. G2 with V(17) in Fig. G8, we see that the Main bank is going to induce a significantly higher voltage across the bus plates of the Bias bank to which the ignitron is connected. The Main bank will also try to pulse charge and reverse polarity on the second stage Bias capacitors (V(13) waveform at $\sim 24 \mu\text{s}$), however because of the additional inductor L1 the first stage capacitors look like they will be relatively unaffected. In the case of Fig. G8, where the Bias bank was charged to -8 kV , the pulse charge only has the affect of zeroing out the charge on the second stage. If the Bank is charged to lower voltages, -1 kV for example, the voltage on the second stage will reverse (Fig. G9), however the voltage reversal is not severe. The only serious concern to address will be the higher voltages induced on the Bias bank bus work, since the Main bank voltage pulse is not dropped as much across the load resistor R_Load as it was across the Bias inductor LBias.

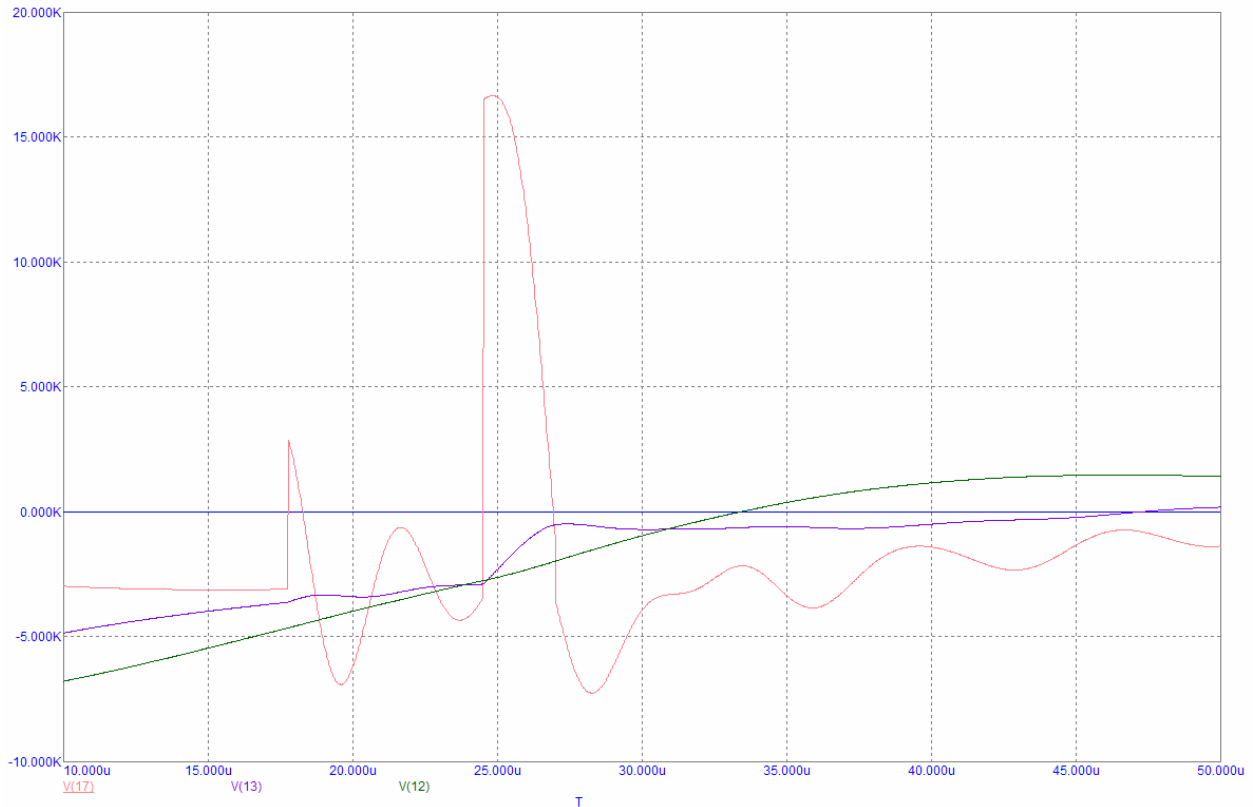


Figure G8. Plot of the voltage at the node between the load resistor and the ignitron and the voltages at the hot terminals of the stage 2 and stage 1 Bias bank capacitors. The initial charge voltage on the Bias bank capacitors was -8 kV .



Figure G9. A similar plot to that shown in Fig. G8, except that the initial charge voltage on the Bias bank capacitors was only -1 kV.

Before moving on from the discussion of the circuit in Fig. G6, a final simulation was run in which the Bias bank ignitron was not triggered. As in the case of the present Bias circuit illustrated by the waveforms in Fig. G3, Fig. G10 shows that with no current flowing through the load resistor, R_Load, the full Main bank voltage that reaches the Theta coils will also be applied across the Bias bank bus work. Since the bus work will have to be improved to hold off the higher voltages shown in Fig. G8 and G9 for normal operation, anyway, any concerns regarding the reliability of the triggering of the ignitron – and problems that might arise if the ignitron is not successfully triggered – should be automatically addressed when these other improvements are implemented.

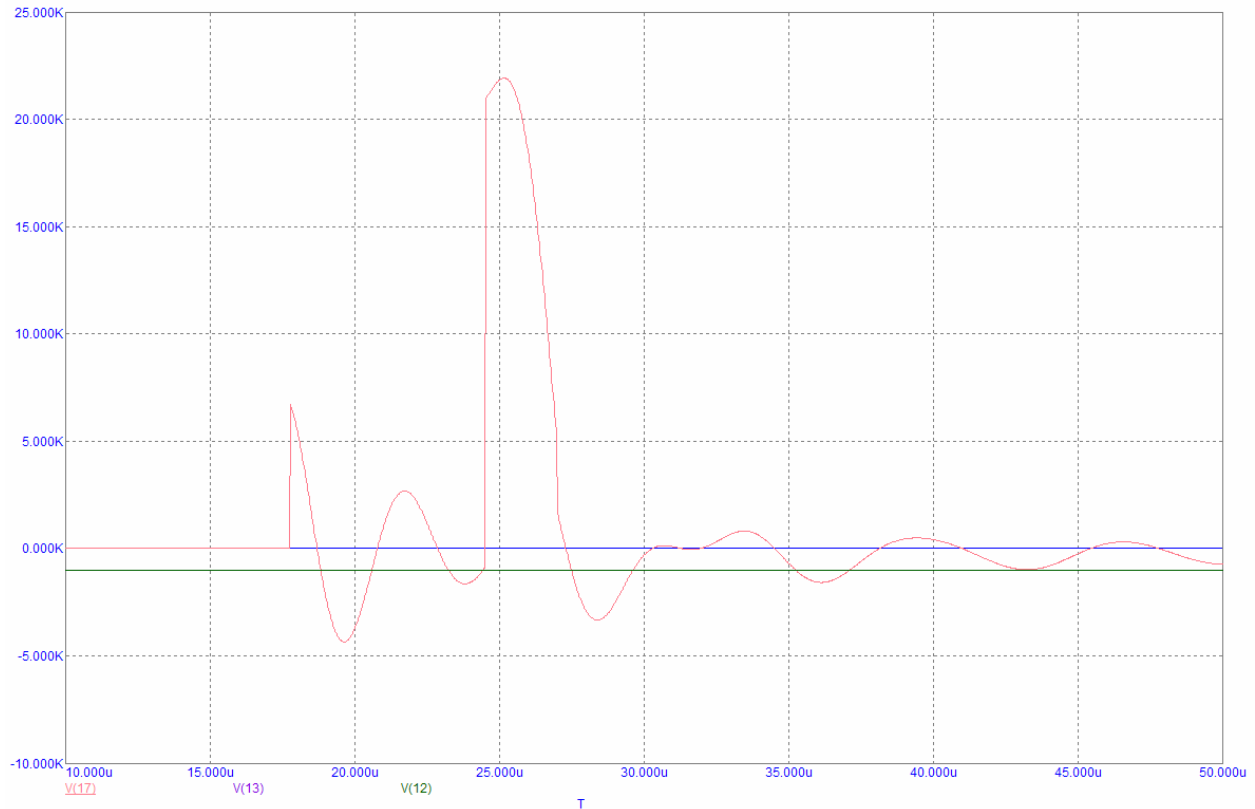


Figure G10. A plot of the same node voltages shown in Figs. G8 and G9 for the case when the Bias bank ignitron is not triggered.

The final set of plots below, obtained by means of these same circuit simulations with MicroCap but plotted in Excel, provides a comparison between the present FRX-L Bias bank and the new Bias bank/PFN that Dr. Intrator has proposed. Current waveforms provided by both banks are shown in Fig. G11 on a long time scale to show the amplitude swing of the present bank and in Fig. G12 on a shorter time scale to show the features of the currents from each PFN stage, as well as from the total PFN/bank. The structure that appears on the PFN current waveforms is, again, primarily due to the discharge of the Main bank, though some structure is caused by the discharge of the PI bank. (Figure G7 also shows this behavior in the current waveform, though because of the scale it is not as visible.) The only concern here might be the current rating of the capacitors, that they could sustain the short but high-current discharge approaching 350 kA.

Figure G13 shows the corresponding waveforms for the voltages across the capacitors for the present bank and the proposed PFN design. As can be seen, the initial charge voltage was -8 kV, and the voltage reversal on the capacitors is considerably less for the PFN design than for the present bank design. For a -1 kV charge (Fig. G14), even though the Main bank drives the voltage reversal on the Bias capacitors here, the total reversal is still only on the order of 1 kV.

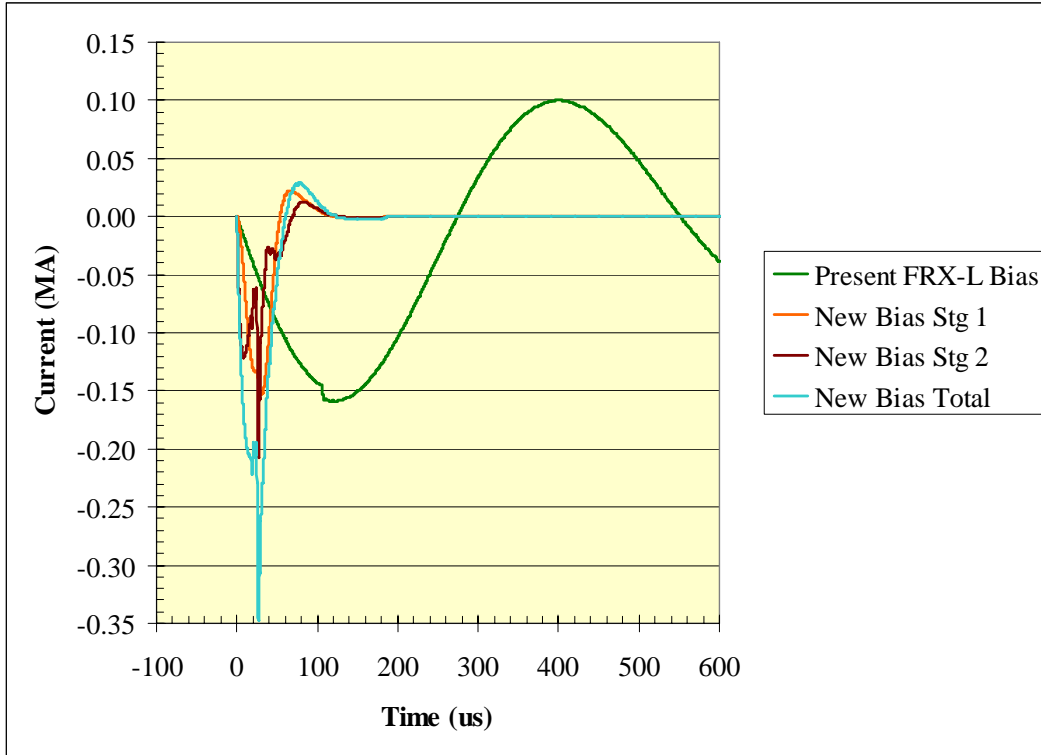


Figure G11. Overlay of the current waveforms calculated by MicroCap using the circuit diagrams shown in Figs. G1 and G6.

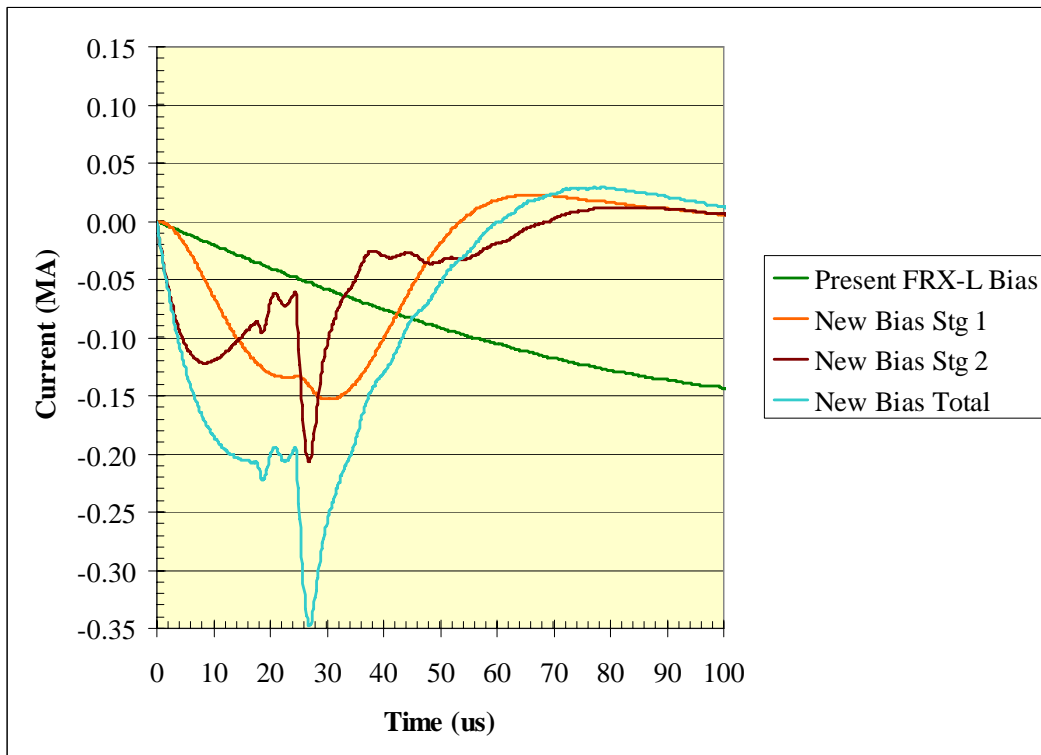


Figure G12. Expanded view of the time period between 0 and 100 μ s from Fig. G11.

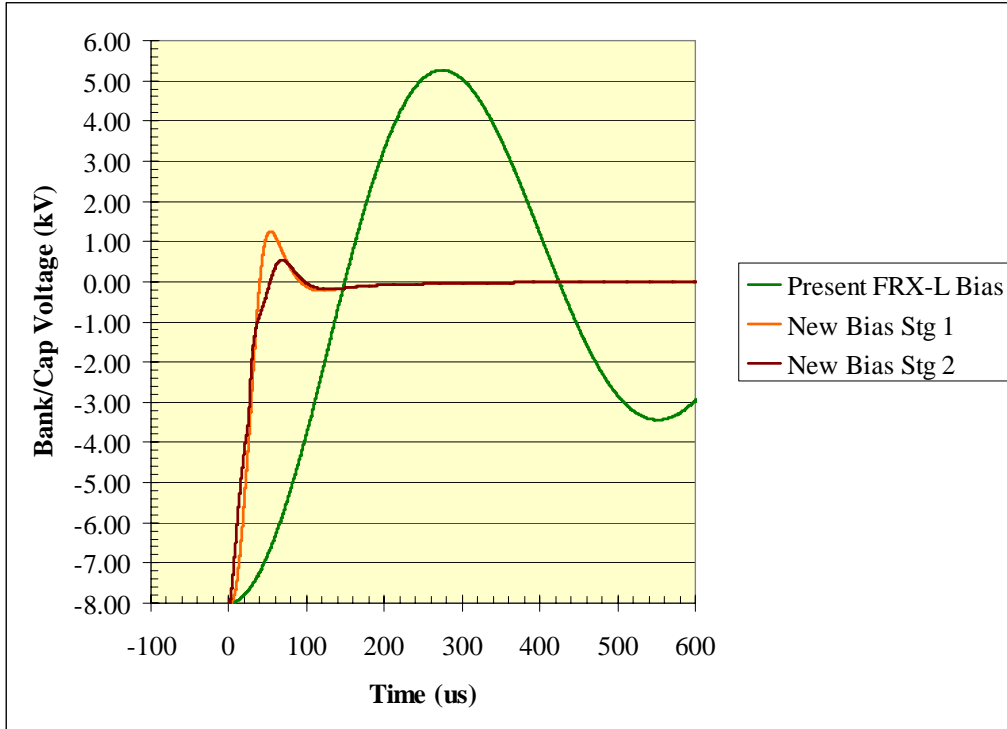


Figure G13. Overlay of the voltage waveforms calculated by MicroCap using the circuit diagrams shown in Figs. G1 and G6. The initial charge voltage on the Bias bank capacitors was -8 kV.

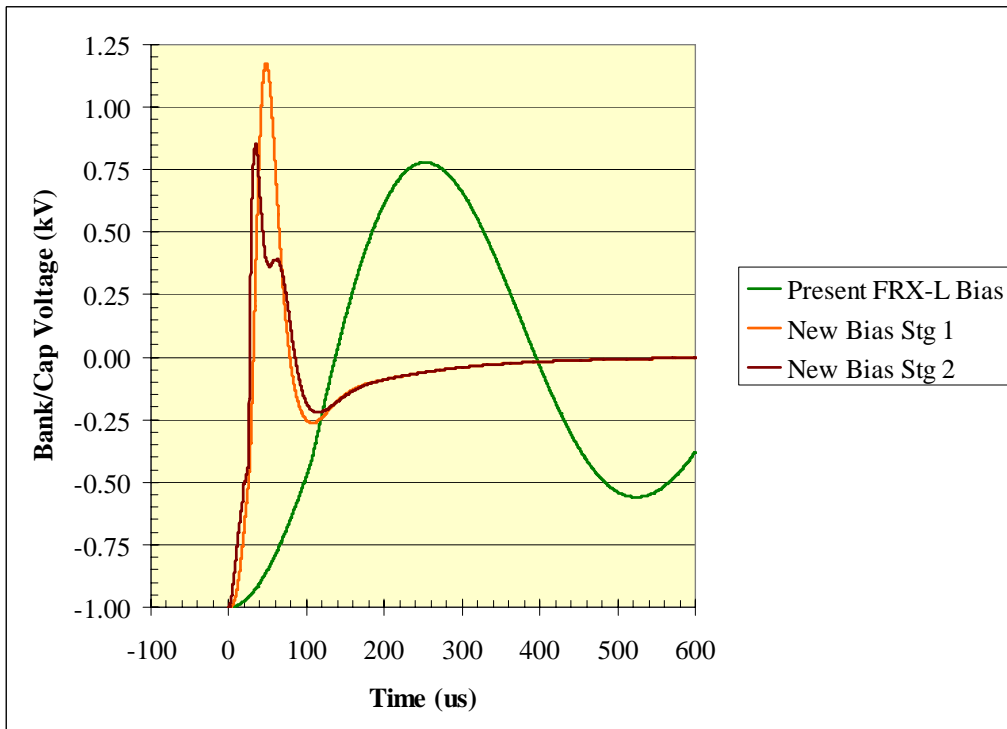


Figure G14. A second overlay of Bias bank voltage waveforms for the case when the initial charge voltage on the Bias bank capacitors was -1 kV.

A final current plot is shown in Fig. G15 for comparison purposes. The Theta coil current is shown here for the two FRX-L Bias banks and the planned AFRL Bias bank. (The PI and Main banks were not included in these simulations.) The AFRL Bias bank plan differs from the present FRX-L Bias bank in that a load/damping resistor has been incorporated to limit the Coulomb transfer through the ignitron switch. The capacitance is also 25% higher (2.55 mF), thus the waveform has a slightly longer period, a similar amplitude, and a lower voltage reversal. For initial pulsed power tests we will be using this bank design, since hardware fabrication is almost complete. When FRC formation tests begin, the bank can be converted to the PFN design concept at that time, should it prove to be necessary.

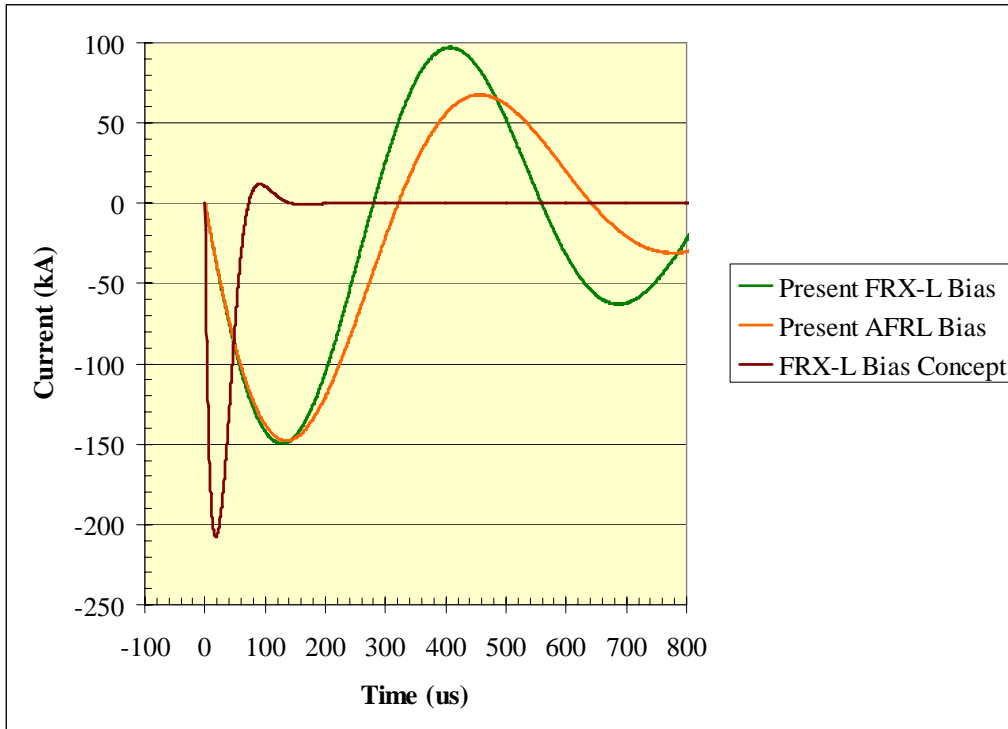


Figure G15. Overlay of the current waveforms calculated by MicroCap for the two FRX-L Bias bank configurations and the FTX (AFRL) Bias bank.

SUMMARY

The additional analyses presented here show no obviously significant problems with implementing the Bias PFN concept. Careful attention must be paid to the bus hardware on the new bank, as the voltage impressed upon it will be somewhat higher than for the present bank. Though these voltages exceed 10 kV, the voltage rating of the Bias capacitors, due to their larger capacity the actual voltage that the capacitors end up being charged to (the voltage reversal on the Bias capacitors) does not appear to exceed 1.5 kV (less for higher initial negative charge voltages on the Bias bank). The current rating of the capacitors should also be checked, as it appears that a high surge current, at least in the second stage of the PFN, is generated when the Main bank is discharged. Key hardware components that would be needed, in addition to a more robust set of bank bus work, are the inductors. L2, in particular, would have to handle the full bank current, as well as hold off some fairly significant voltages.

APPENDIX H. INITIAL ANALYSIS OF PFN CONCEPT FOR DRIVING THE FRC GUIDE/MIRROR FIELD COILS

This memo describes a set of follow-up simulations of the PFN circuit discussed in Dr. Tom Intrator's memo (sent on 15 May 2006) as a possible scheme for driving the translation magnets. The circuit diagram shown in the memo is reproduced in Fig. H1, except that six PFN stages, as was discussed in the text of the memo, are shown instead of four. With the field coils set up to be the stage inductances and with each coil having an inductance of $50 \mu\text{H}$, this circuit is essentially set up to drive 12 coils. A load resistance of 0.316Ω is shown at the "end" of the circuit to provide a matched load, and the ignitron resistance of 0.015Ω is incorporated into the switch model.

For an initial charge voltage of 10 kV on each of the capacitors, MicroCap calculates the voltage and current waveforms shown in Fig. H2 for the load and each of the field coils. Immediately we note that the shape of the current waveform is different for each coil. The pulse width becomes shorter for coils positioned further from the load in the circuit, suggesting that the magnetic field in these coils will not be able to fully penetrate the liner and fill the liner region. Furthermore, the current in coil 1 falls short of the peak value ($15 \sim 17 \text{ kA}$) obtained in the other coils.

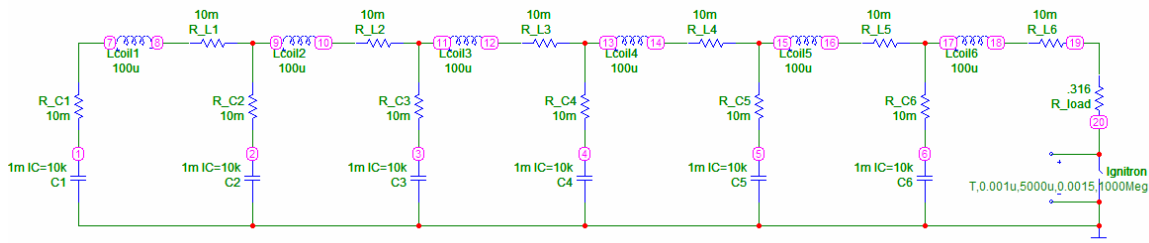


Figure H1. Circuit model of a PFN configured to drive the FRX-L translation (Guide and Mirror) magnets.

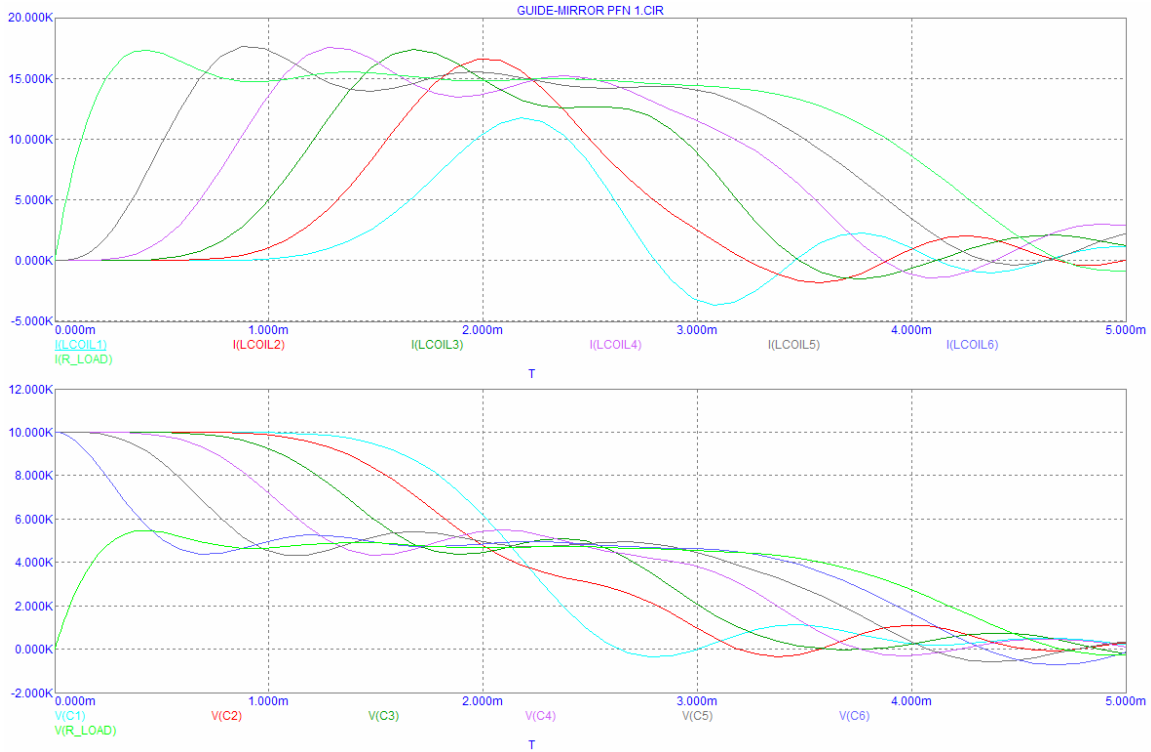


Figure H2. Current and voltage waveforms calculated by MicroCap for the circuit shown in Fig. H1.

Figure H3 shows another PFN circuit very similar to that in Fig. H1, however the field coils are now placed “outside” of the PFN, adjacent to the load resistor. This circuit now mirrors one discussed in an earlier memo (provided in Appendix G of this report) that is being considered for generating a higher-amplitude and faster Bias field. With all 12 coils in parallel, the I(LMAGNETS) curve in Fig. G4 shows that each coil receives the same current over the same time period, so that the diffusion into and filling of the liner region should be uniform everywhere. However, with all of the coils in parallel, each coil now receives only 1/12th of the PFN current (=1.25 kA).

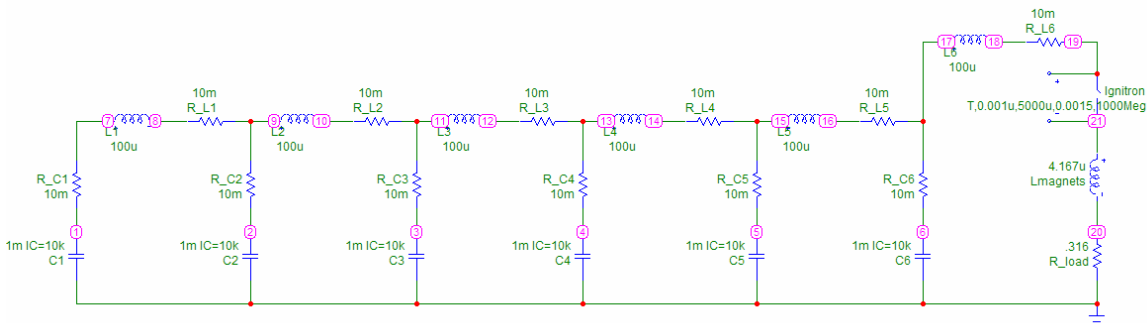


Figure H3. An alternative PFN circuit concept in which the translation (Guide and Mirror) magnets are now placed in parallel close to the load.

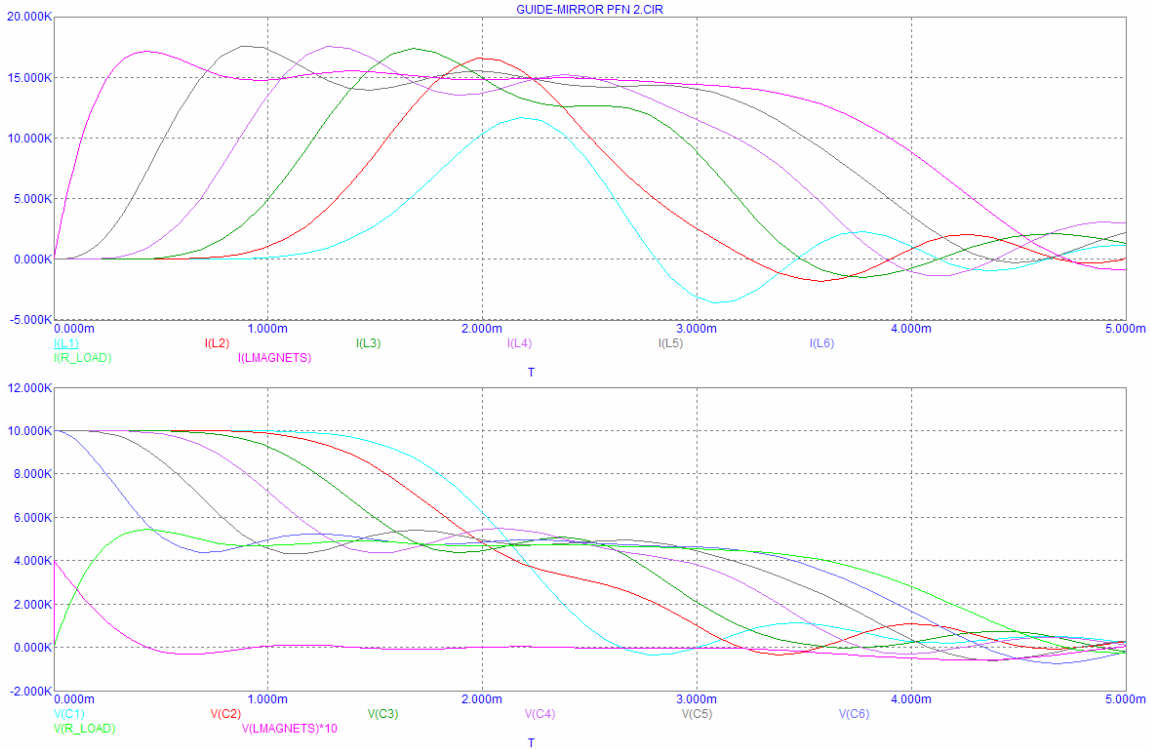


Figure H4. Current and voltage waveforms calculated by MicroCap for the circuit shown in Fig. H3.

The current can be increased by reducing the stage inductance and by adding additional stages (Figs. H5 and H7), however the current pulse width tends to decrease dramatically (Fig. H6 and H8) when this is done. Implementing different parallel and series combinations of coils may still allow us to arrive at an acceptable solution, but changing the arrangement of the coils changes the net coil inductance (PFN load impedance), which in turn further changes the response of the PFN. (We note that if the total field coil inductance is allowed to become too large compared to the stage inductances, the PFN begins to act like a “regular” capacitor bank again.)

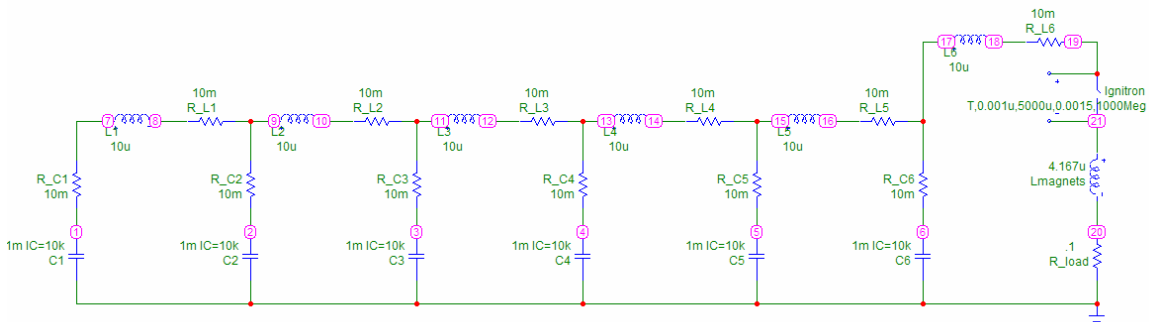


Figure H5. A PFN circuit similar to that in Fig. H3 but with a decreased stage inductance.

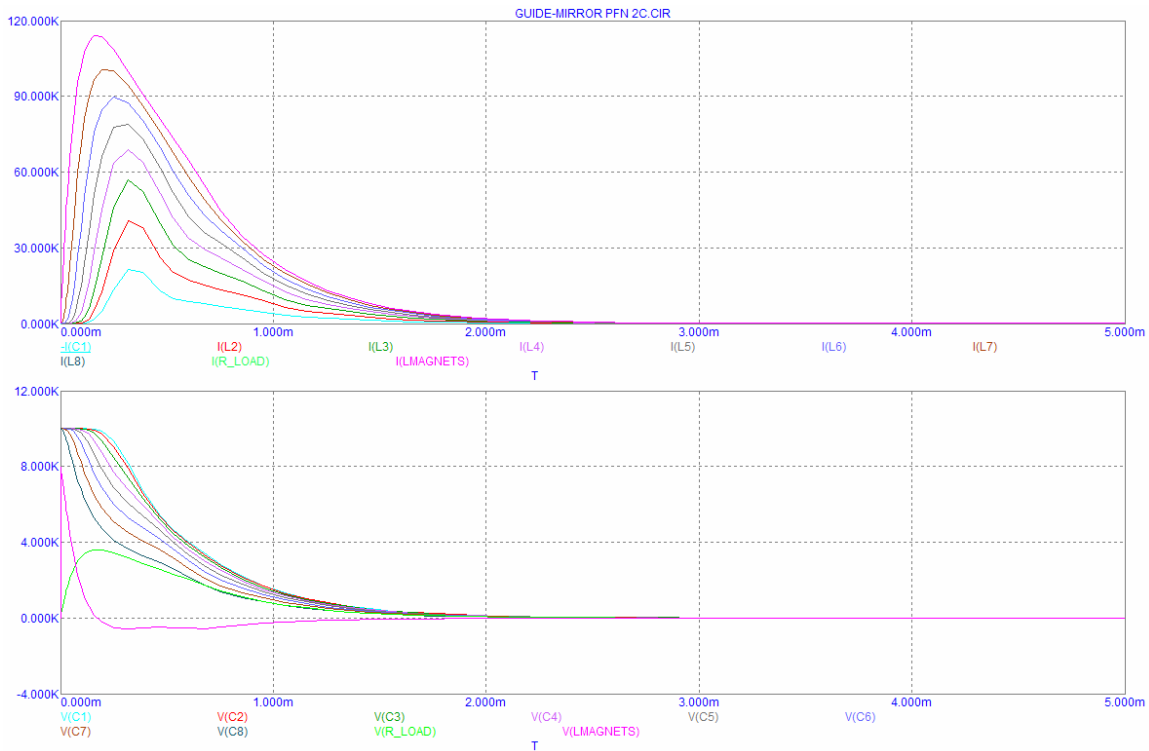


Figure H8. Current and voltage waveforms calculated by MicroCap for the circuit shown in Fig. H7.

At this point, before pursuing a possible PFN design further, it seems prudent to narrow down the parameters for the field coil design. The field coils proposed earlier by Lenny Dorf of LANL (Fig. H9) have a larger bore than that of the present Cusp coils, which we were assumed to be using in the circuit models above. If we plan on keeping the acrylic vacuum vessel around the liner, so that the return conductor can be slotted, field coils having an even larger bore will be required. The coils shown around the liner in Fig. H9 have a bore diameter of 9.5 inches, a total of 8 layers of windings with 4 turns per layer, and a conductor with a square cross section (0.5in. by 0.5 in.). Using the figures and equations for the inductance of multi-layer coils found on pages 60 and 61 in Terman's *Radio Engineers Handbook*, an inductance of 346 μH is calculated for this coil. An even larger (wider) coil is shown for the mirror at the end of the liner, though possibly two of these coils, spaced closely together, could be used for the mirror. Nevertheless, given the large inductances of these coils, a PFN concept may not work for driving them (based upon the comment made earlier that when the field coil inductance is allowed to become very large compared to the PFN stage inductances, the PFN begins to act like a "regular" capacitor bank again).

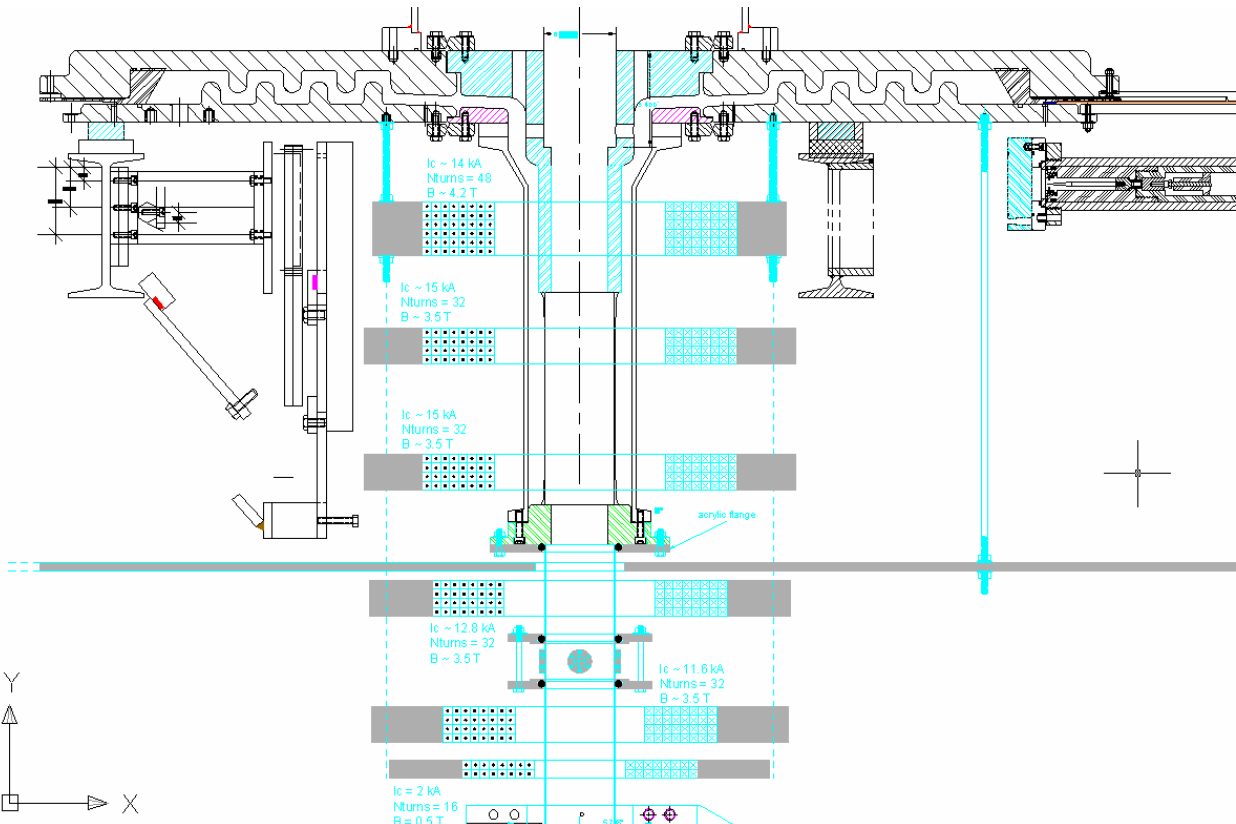


Figure H9. Conceptual field coil designs and arrangement along the translation region and solid liner that will allow enable FRC translation from the Theta coil region into the liner.

SUMMARY

Because of the long magnetic field diffusion and filling time required in the liner region, a PFN may not work as well for generating the Guide/Mirror field as for generating the Bias field in the Theta coil region. Furthermore, because the current pulse shape and amplitude varies for each stage inductor in the PFN, there does not appear to be a straightforward way of simply letting the Guide and Mirror field coils act as the stage inductances. Before further analysis continues with the PFN concept, it seems prudent to finalize the design parameters required for the field coils so that it is possible to better determine the viability of using a PFN to drive these coils.

DISTRIBUTION LIST

DTIC/OCP 8725 John J. Kingman Rd, Suite 0944 Ft Belvoir, VA 22060-6218	1 cy
AFRL/VSIL Kirtland AFB, NM 87117-5776	2 cys
AFRL/VSIH Kirtland AFB, NM 87117-5776	1 cy
Official Record Copy AFRL/DEHP Attn : Dr. James Degnan 3550 Aberdeen Ave SE B322 Kirtland AFB, NM 87117-5776	1 cy
SAIC Attn : Colleen Garcia 2109 Air Park Road SE Albuquerque, NM 87106	2 cys

This page intentionally left blank.